POLITECNICO DI TORINO

Corso di Laurea Magistrale in Ingegneria Aerospaziale

TESI DI LAUREA MAGISTRALE

Geometrically Nonlinear Analysis of Axial Rotors

Relatori
Prof. Erasmo Carrera
Prof. Matteo Filippi

Candidato:
Alessandro Maturi

Luglio 2021

“La montagna più alta rimane sempre dentro di noi”

Walter Bonatti

Ringraziamenti

Voglio dedicare questo spazio iniziale a tutti coloro che, con il loro supporto, mi hanno aiutato in questo lungo e meraviglioso percorso di crescita personale e di approfondimento delle conoscenze acquisite durante i miei anni universitari.

Un enorme ringraziamento va innanzitutto ai miei genitori, fonte di sostegno e di coraggio, per avermi trasmesso la passione per lo studio e la forza di volontà necessaria per raggiungere questo traguardo. Grazie per tutti i consigli e in particolar modo per le esperienze ed i viaggi che mi avete permesso di vivere insieme a voi fin da bambino: anche se è impossibile ricordare tutti quei momenti, sono assolutamente certo che essi siano stati fondamentali per la determinazione del mio carattere e del mio modo di pensare. Dal picco del Preikestolen in Norvegia, passando attraverso i viaggi in camper in Europa fino ai grattacieli di New York, avete dato a me e a mia sorella una diversa prospettiva sul mondo e gli strumenti per approfondire, forse anche troppo, ogni situazione. Senza tale spinta propulsiva non sarei qui oggi a dedicarvi la gioia di questo momento.

Un sentito grazie anche a mia sorella Laura, per i nostri dibattiti e scambi di idee portati avanti in questo anno di Covid, durante il quale, dopo molto tempo, siamo tornati a vivere nella stessa casa: continua con la tua determinazione verso il tuo prossimo, vicino obiettivo.

Un ringraziamento a tutti gli amici di spirito e compagni di avventure di Fiavè, di Burro, del Bleggio e di Torino: i momenti di svago e di montagna passati con voi durante i weekend e in estate sono stati fondamentali per ricaricarsi tra le sessioni di esami.

Per ultimi, ma non meno importanti, voglio qui ringraziare i professori Carrera e Filippi, relatori di questo lavoro di tesi. Il loro supporto e disponibilità nel fornire consigli sono stati cruciali per la stesura dell'elaborato finale.

Acknowledgements

I'd like to dedicate this initial space to all those who, with their support, have helped me in this long and wonderful journey of personal growth and deepening of the knowledge acquired during my university years.

First of all, a huge thanks goes to my parents, a source of support and courage, for giving me the passion for studying and the willpower necessary to reach this goal. Thanks for all the advice and especially for the experiences and travels that you have allowed me to live with you since I was a child: even if it is impossible to remember all those moments, I am absolutely sure that they were fundamental for the determination of my character and my way of thinking. From the peak of Preikestolen in Norway, passing through motorhome trips in Europe to the skyscrapers of New York, you have given my sister and me a different perspective on the world and the tools to explore, perhaps too much, every situation. Without this driving force I would not be here today to dedicate the joy of this moment to you.

A heartfelt thanks also to my sister Laura, for our debates and exchanges of ideas carried out in this year of Covid, during which, after a long time, we have returned to live in the same house: continue with your determination towards your next, near goal.

Thanks to all the friends and adventure mates of Fiavè, Burro, Bleggio and Turin: the moments of leisure spent with you and in the mountains during the weekends and in the summer were fundamental to recharge between the exam sessions.

Last but not least, I want here to thank professors Carrera and Filippi, supervisors of this thesis work. Their support and availability in providing advice were crucial for the drafting of the final thesis paper.

Sommario

Questo lavoro di tesi è focalizzato sull'analisi di sistemi rotanti complessi, soggetti a condizioni operative plausibili nella realtà pratica delle applicazioni aeronautiche. Vengono valutati gli effetti rotordinamici introdotti dalla forza centrifuga; in particolare, l'analisi verrà portata avanti considerando dischi con spessore costante e variabile, che vengono assunti incastrati all'hub o supportati da un albero deformabile e quindi flessibile, non rigido.

I contributi del pre-stress sono stati ottenuti attraverso l'integrazione di uno stato di tensione tridimensionale, che viene generato prevalentemente dai carichi centrifughi, moltiplicati dai termini non lineari del campo di deformazione. La forma debole delle equazioni di governo è stata risolta usando il metodo degli elementi finiti.

Una serie di elementi 1D ad alta fedeltà sono stati sviluppati in accordo con la teoria CUF, che permette di oltrepassare le assunzioni cinematiche delle teorie classiche delle travi. Seguendo l'approccio component-wise (CW), sono stati adottate espansioni polinomiali alla Lagrange per sviluppare delle teorie agli spostamenti più raffinate.

Gli elementi LE permettono di modellare ogni elemento strutturale del rotore con un grado arbitrario di accuratezza usando differenti teorie per gli spostamenti o delle mesh con raffinazione locale.

Per fare ciò, durante questo lavoro di tesi è stato utilizzato il codice MUL2, sviluppato dall'omonimo gruppo di ricerca all'interno del dipartimento e basato sulla Formulazione Unificata proposta dal professor Carrera (CUF). Tale software presenta infatti la potenzialità di eseguire analisi linearizzate e geometricamente non lineari, che verranno qui applicate a numerosi modelli di strutture di comune applicazione aeronautica.

Abstract

This master thesis work is focused on the analysis of complex rotating systems, subjected to plausible operating conditions in the practical reality of aeronautical applications. The rotordynamic effects introduced by the centrifugal force are here evaluated; in particular, the analysis will be carried out considering discs with constant and variable thickness, which are assumed to be keyed to the hub or supported by a flexible, deformable shaft.

The contributions of the pre-stress are obtained through the integration of a three-dimensional state of tension, which is mainly generated by the centrifugal loads, multiplied by the non-linear terms of the deformation field. The weak form of the governing equations is solved using the finite element method.

A series of high fidelity 1D elements have been developed in accordance with the CUF theory, which allows to go beyond the kinematic assumptions of classical beam theories. Following the component-wise (CW) approach, Lagrange-like polynomial expansions have been adopted to develop more refined displacement theories.

Lagrange-expansions LE elements allow the user to model each structural element of the rotor with an arbitrary degree of accuracy using different displacement theories or meshes with local refinement. This allows to obtain very reliable results, with a much lower computational cost than traditional FEM codes.

In order to do this, during this thesis work the MUL2 code has been used, developed by the homonymous research group within the department and based on the Carrera Unified Formulation (CUF). In fact, this software has the potential to perform linearized and geometrically non-linear analyzes, which will be applied here to numerous models of structures of common aeronautical application.

Contents

List of Figures

List of Tables

Part I

INTRODUCTION

Chapter I

Reference framework

Air traffic has experienced a truly sudden development in recent decades. Indeed, the International Air Transport Association (IATA) noted that between the 1970s and the late 1990s air traffic doubled in numbers approximately every 15 years, and it was expected that this market would continue to grow annually at rates of 4% - 5% for next twenty years. These forecasts inevitably had to collide with the heavy price of the COVID-19 pandemic, both in terms of health and human lives, as well as in terms of the possibility of travel and movement of the population.

The limitations on international connections, the more or less generalized "lockdowns" at a global level (**Fig. 1.1**), the absence of tourism for almost the entire year of 2020 and a good part of 2021, pending herd immunity acquired through vaccinations, resulted in a very violent contraction of GDP in all nations and caused, among other things, serious financial problems for the airlines. It is well known that this economic activity is one of the most difficult, as it organizes and mobilizes some of the most complex systems that man has ever developed: first of all it is based on aerospace engineering technology, which for regulations requires very high standards of reliability and safety ($1 \cdot 10^{-9}$); secondly, air traffic interfaces for the most part with different nations and is therefore very susceptible to possible diplomatic incidents and/or problems. Last but not least, air traffic is an activity that is highly dependent on the market trend of some fixed expenses, among all the cost of fuel, which is by far the most decisive.

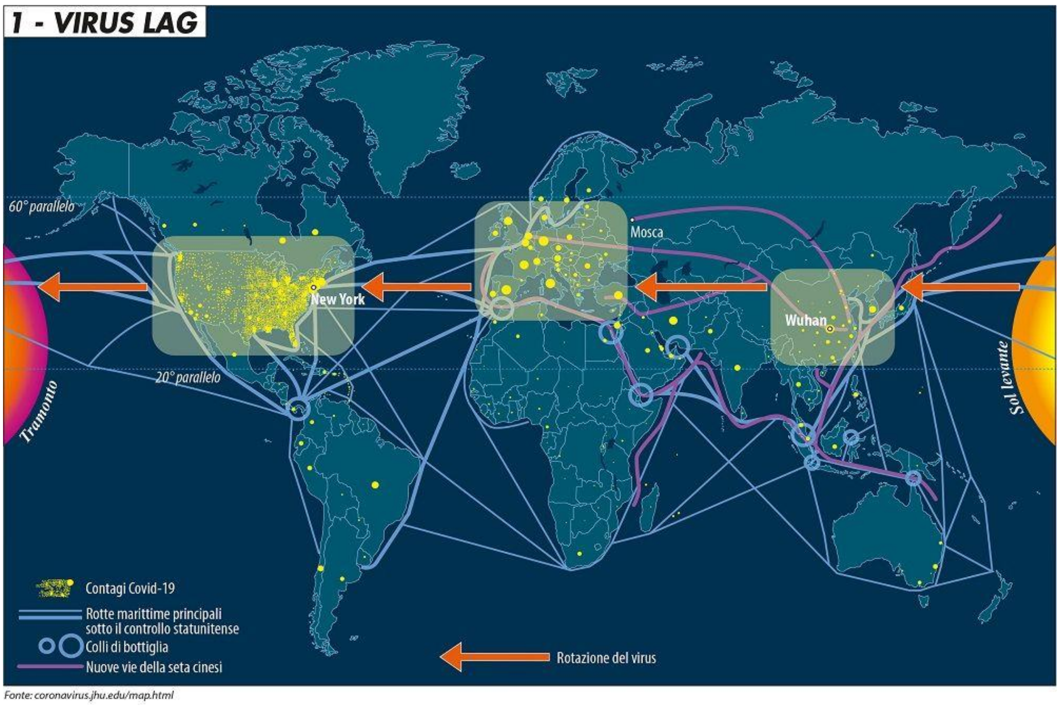

Figure 1.1 : Virus Lag, courtesy of LIMES – Rivista Italiana di Geopolitica [1]

If in a normal year the cash-flow margin of a standard airline is around 3% -5% of its revenue (**Fig. 1.2**), it is easy to understand how during these pandemic months many airlines suffered enormous financial losses or even bankruptcy, requiring and almost always obtaining state aid by virtue of the national interest.

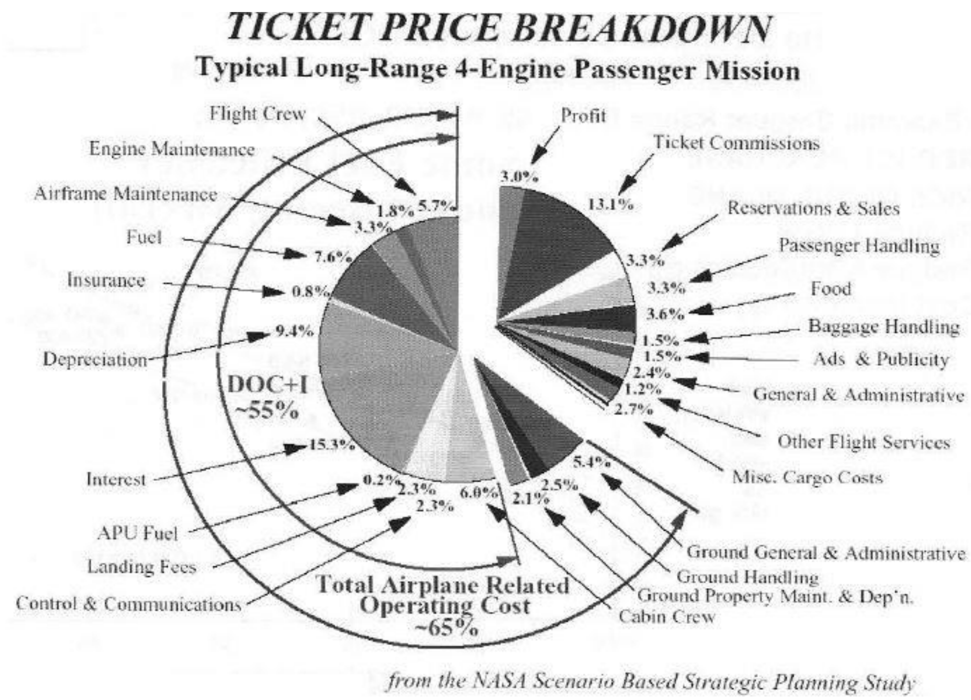

Figure 1.2 : Ticket Price Breakdown

The ability to move people and goods, to connect different parts of the planet, but above all the ability of the aeronautical and aerospace sector to invest in technological research and innovation has always been recognized by nations with ambition for power, because it still represents one of the most advanced sectors of human activity. Despite this, the aeronautical field is always developing and is nowadays facing new challenges, among which the most relevant are certainly the attempt at an energy transition or at least the fight against global warming and the reduction of pollutant emissions and greenhouse gases.

The needs of the final consumer (passenger) and these new environmental protection requirements for next generation aircraft translate into the study of new components of improved reliability and efficiency. Bearings and rotor systems are certainly two of the components that most significantly determine the reliability and effective mechanical performance of aerospace applications such as propulsion systems (turbine jet engines) and transmission systems (gearbox).
These systems must withstand very severe and demanding operating conditions: the main shaft bearings of a modern aircraft engine experience very high levels of temperature and rotational speeds, while they must meet the highest safety and reliability standards trying to minimize weight. Such operating conditions and requirements represent an ongoing challenge to find improvements in all fields of rotor technology.

The so-called "Bearing speed index", that is the product of the bearing diameter and the rotation speed, $D \times N$ represents a very useful parameter in providing information about the centrifugal forces, the speed of the system and in general the operating conditions of the rotor. Since there has always been the need to increase the specific thrust ("thrust-weigth-ratio") and at the same time to reduce fuel consumption as much as possible, the rotation speed of the shafts and the temperatures of the gases have constantly increased since when jet engines were first introduced. Today, for example, the main shaft bearing operates at a speed index of up to $DN = 3.5 \cdot 10^6 \frac{mm}{min}$.

To get an idea of the development of these components, it is possible to refer to this image (**Fig. 1.3**) taken from reference **[2]**, which presents the "speed index" trend of some significant aircraft engines over the years.

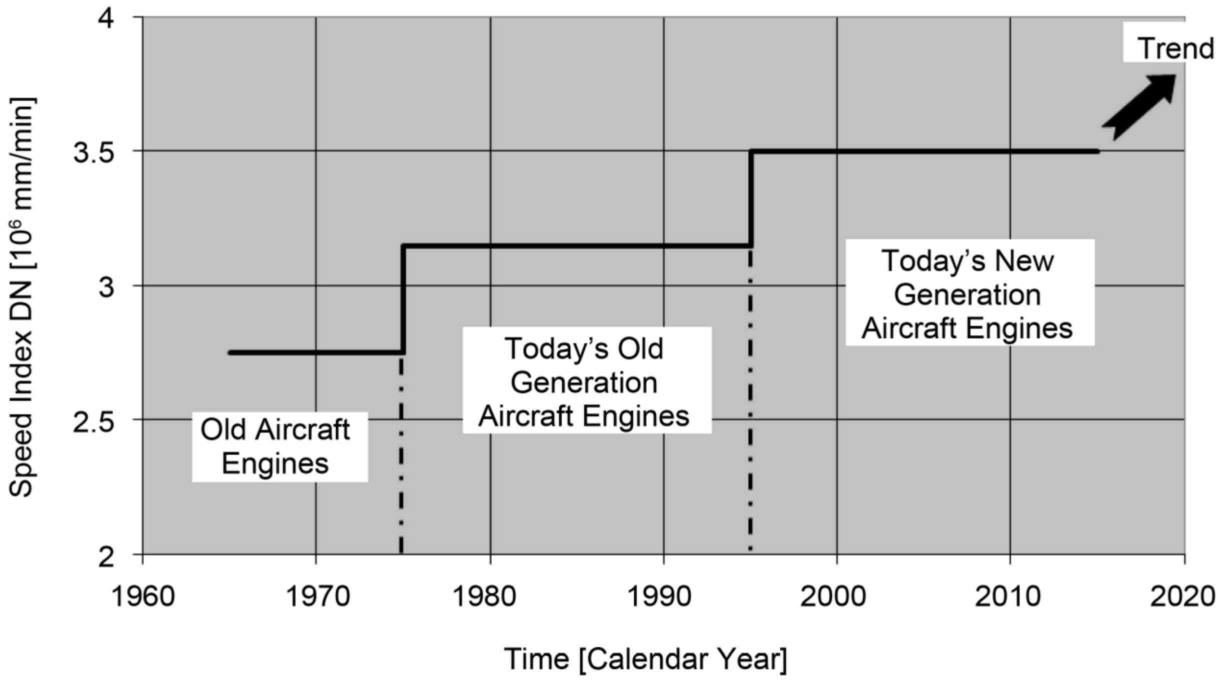

Figure 1.3 : Speed index for main shaft aircraft engine bearings. [2]

However, the more the speed index rises, the more problems related to rotor-dynamics begin to arise: the higher rotational speeds produce greater centrifugal forces and the weight limitation of the mechanical components and rotors lowers their stiffness, causing vibrations which, if not checked, could lead to resonance and destruction of the machine.

Resonance describes the phenomenon of increased amplitude that occurs when the frequency of a periodically applied force is equal or close to a natural frequency of the system on which it acts. When an oscillating force is applied at a resonant frequency of a dynamic system, this system will oscillate at a higher amplitude than when the same force is applied at other, non-resonant frequencies, potentially reaching a critical level, beyond which the structure could break.

This was the case with the Tacoma Narrows bridge, a suspension bridge built in 1940 in the state of Washington on the Pacific coast. Problems related to vibrations immediately emerged

and became more visible especially during the particularly windy days, so much so that the population began to nickname him "Galloping Gertie (**Fig 1.4**).
Unfortunately around ten o'clock on the morning of November 7, 1940, just over four months after its inauguration, the bridge began to sway and twist fearfully due to strong gusts of wind: about two hours later, following the showy twists of the central span which reached 70° of inclination, some tie rods broke, the structure reached the breaking point and the central span collapsed, falling into the water. This was the first evidence of that would be later called aero-elastic flatter, which is also related to resonance.

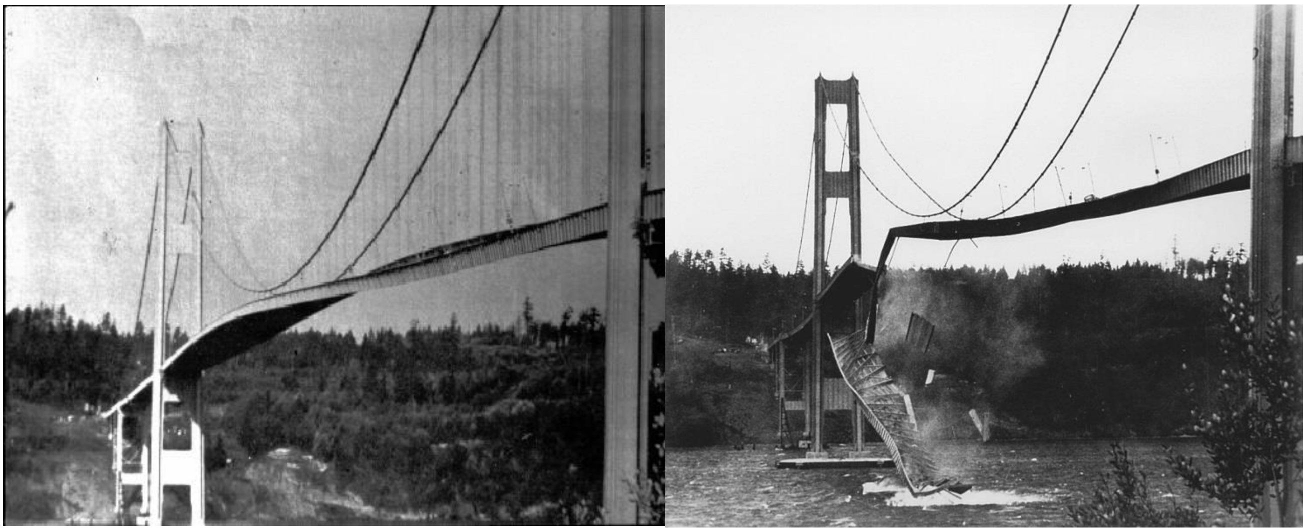

Figure 1.4 : Tacoma Narrows Bridge – 1940 – Washington State - USA

The simplest system we can think of dynamically is the undamped 1 degree of freedom (1 DOF) system, which is shown in the next image (**Fig 1.5**). In this simple case, every physics book states that the resonant frequency (or natural frequency) is given by the following formula, where m represents the oscillating mass, while k represents the stiffness of the spring. Remember that we are considering an undamped system, so $c = 0$.

$$\omega_n = \sqrt{\frac{k}{m}}$$

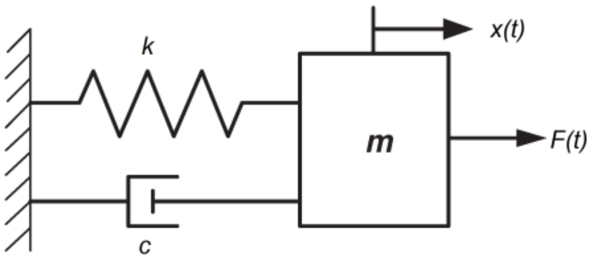

Figure 1.5 : Single degree of freedom vibrational model (1 DOF)

It is therefore easy to understand how the reduction in stiffness can lower the resonance frequency to values that can be reached in today's rotating machines: Rotordynamics must be considered.

Chapter II

History of Rotordynamics

"Human history may be built on the development of technology" *J.S. Rao* **[3]**

Although the invention of the wheel dates back to prehistoric times and the use of rotating systems has accompanied humanity since the dawn of time, it was only during the 19th century, thanks to the industrial revolution, that the first accurate studies on rotors were conducted (**Fig 2.1**).
Only then, in fact, thanks to the invention of the steam engine and then the internal combustion engine, it was possible to reach speeds that caused breakdowns to the rotating machines, to the point of pushing scientists and engineers of that time to study the causes in depth. As stated by J. Vance in his book **[4]** , "most rotordynamic investigations have been motivated by machine problems or failures".

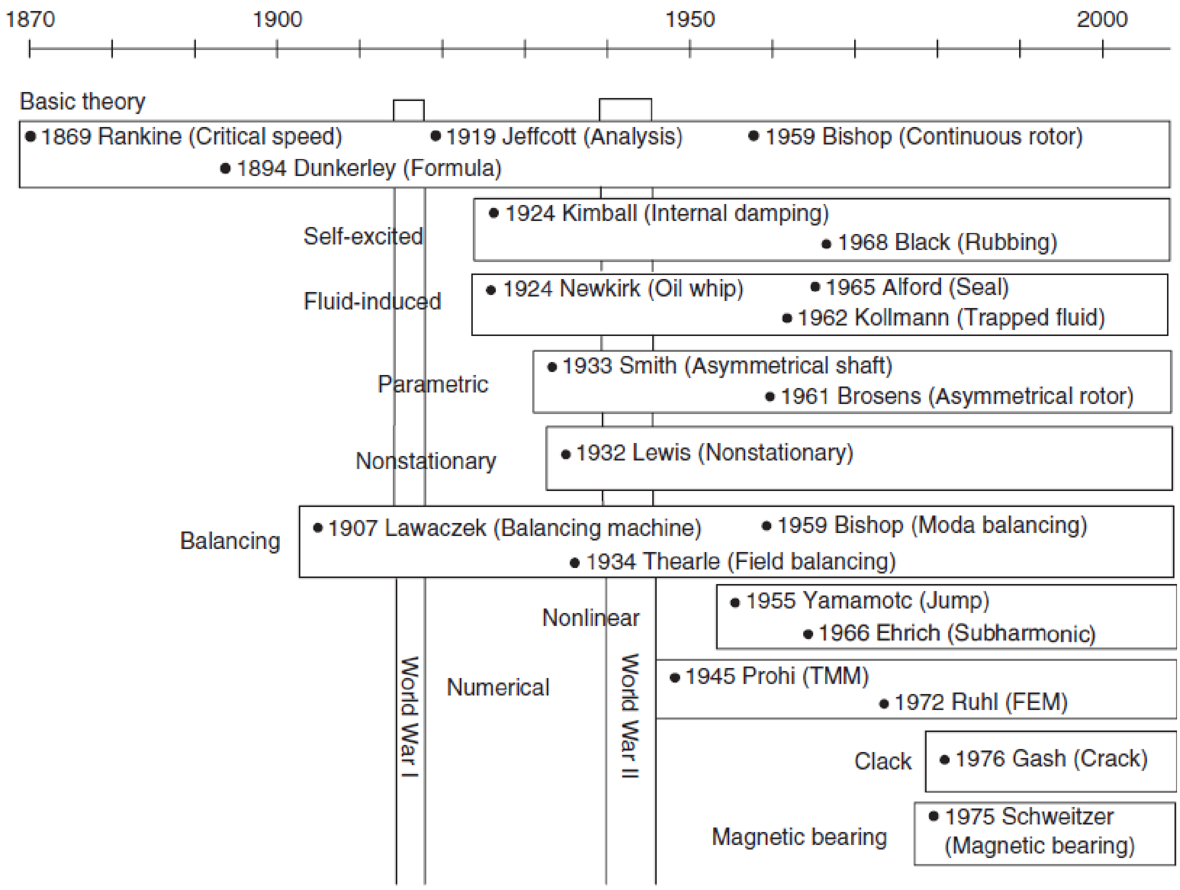

Figura 2.1 : History of Rotordynamics [5]

The development of vibration theory, as a subdivision of mechanics, came as a natural result of the development of the basic sciences it draws from, mathematics and mechanics. The vibration phenomenon was identified already at Aeschylos times, and indeed Pythagoras of Samos (ca. 570-497 BC) conducted several vibration experiments with hammers, pipes and strings, of which he analyzed the harmonics. He was even able to prove with his experiments that natural frequencies are system properties and do not depend at all on the magnitude of the excitation. This proves that in the ancient world there was some kind of progress about vibration theory and a basic understanding of the principles of natural frequency, vibration isolation and their measurements. However, this original body of knowledge had very limited use in engineering and innovation, due to the low level of production technology and machinery speeds, as well as a substantial lack in all the other subjects involved.

For example, calculus and mechanics, which are the basis for the analytical treatment of the problem, began to be developed only during the 1600s and 1700s, with the discoveries of Galileo, Newton and Leibniz. The early stages of mechanization and the first industrial revolution, together with the utilization of chemical energy with the associated high-power machinery (**Fig 2.2**), introduced numerous vibration problems, and the rapid development of calculus and continuous mechanics led to rapid development of the vibration theories by the mid-19th century.

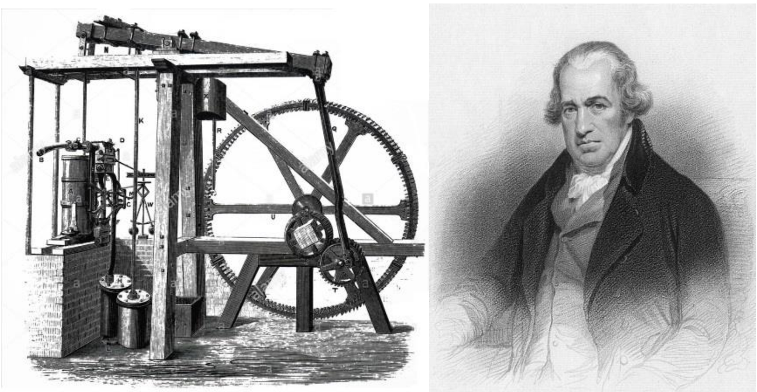

Figura 2.2 : James Watt and its Steam Engine

The wave equation was first introduced by D'Alambert in a memoir to the Berlin Academy in 1750 and the solution of the string equation is due to Daniel Bernoulli. The first mathematical solution to the problem of the vibrating string was obtained by Lagrange in 1759, considering it as sequence of small masses: an approach still used today. Euler and James Bernoulli tried to solve the vibrating plate and shell problem analytically, obtaining the differential equations considering them as consisting of two system of beams perpendicular to each other. Further major improvement was made by Poisson and Kirchhoff, but it was eventually Navier who gave a rigorous theory describing the bending vibrations of plates.

This was meant to be just a fast recap of some of the major development in the sciences that are at the base of rotordynamics. There are countless other scientists and scholars worthy of having made great developments in this field, but to list them all would have been impossible in these few pages.

Rotating machines began to be manufactured in what we can call mass production concurrently with the development of waterwheels for hydraulic power in the early 1800s and steam turbines in the late 1800s. One of the first dynamic problems which was encountered was the critical speed: in this situation, a vibration caused by the rotor imbalance is amplified by the resonance with the natural frequency of the system, causing the rotor axis to deflect.

Research on rotordynamics spans at least a 140-year period, starting with Rankine's paper about the whirling motions of a rotor, which dated back to 1869. The famous Scottish engineer and physicist discussed the relationship between centrifugal forces and restoring forces, concluding that any kind of operations above a certain rotational speed would be impossible to achieve.

Much progress in this area was achieved by the end of the nineteenth century, mainly thanks to the contribution of De Laval and Stodola. The first was a Swedish engineer who invented a one-stage steam turbine and succeeded in its operation, first with a rigid and then with a flexible rotor. His greatest achievement was to show that it was possible to operate in supercritical field by operating at a rotational speed which was about seven times larger than the critical speed, as can be gleaned from Stodola's 1924 publication **[6].** He was the first to notice that he could accelerate through the critical speed, and that the operation at supercritical speeds, way above the critical one, was very smooth.

In 1916 Stodola introduced for the first time the concept of bearing damping in rotordynamics, proving that the presence of damping limits the amplitude due to the unbalance at the critical speed. He also observed the decrease of the critical speed due to damping and was able to compute the phase angle with bearing damping.

As we can imagine, in the early days the major concerns for researchers and designers was to try to predict the value of the critical speed, because their major concern in designing rotating machinery was to avoid resonance.

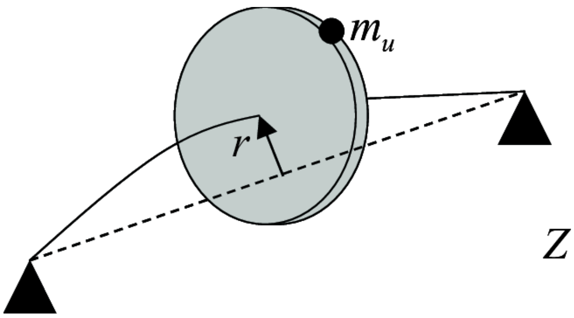

Figure 2.3 : Jeffcott Rotor

The first recorder fundamental theory of rotordynamics can be found in a scientific paper published by Jeffcott in 1919: because of his study and theory, we now call Jeffcott Rotor the system consisting of a shaft with a disk positioned at its midspan (**Fig 2.3**).

He obtained a correct analysis of the critical speed inversion with damping included, and, as a consequence, the predominant design philosophy changed and accepted the practice of turbomachinery supercritical operations. During the same years, also the dynamics of elastic shafts with disks, the dynamics of continuous rotors and the balancing of rigid rotors were analyzed, alongside with the approximate determination of critical speeds of rotors with variable cross sections.

Thereafter, the center of research and scientific world shifted from Europe, that was emerging from the tragedy of the First World War, to the United States , and the scope of rotordynamics expanded to consider many other phenomena. Wilfred Campbell investigated the vibrations in steam turbines in detail, while working at General Electric in the 1920s: he came up with the idea of plotting a diagram, representing critical speed in relation to the cross points of natural frequency curves and the straight lines proportional to the rotational speed. This concept is now widely used and we call it Campbell diagram, after the name of his developer (**Fig 2.4**).

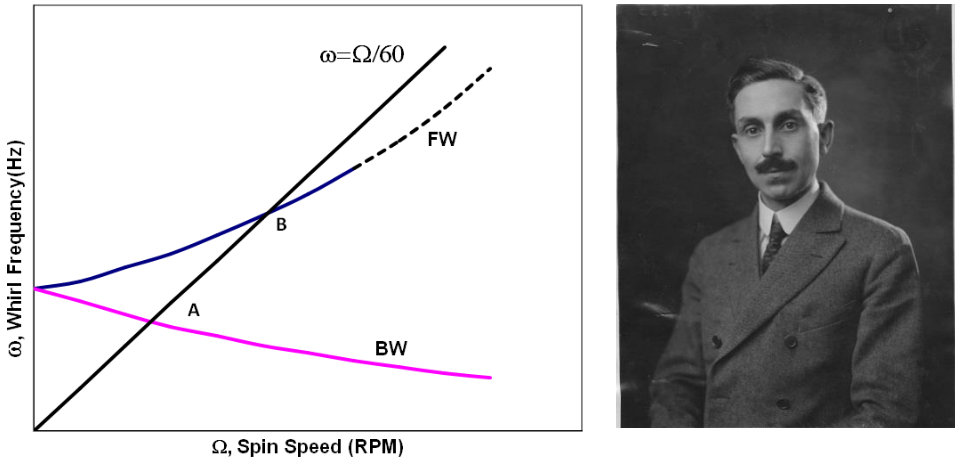

Figure 2.4 : Wilfred Campbell and an example of his diagram

As the rotational speed increases above the first critical speed, the occurrence of self-excited vibration became a serious problem. Newkirk and Kimball recognized the phenomenon according to which the internal friction of shaft materials could cause an unstable whirling motion: they investigated a whirl instability called *oil whip*, caused by the oil film in the small clearance of journal bearings (**Fig 2.5**) which occurs at about two times the critical speed **[7]**.

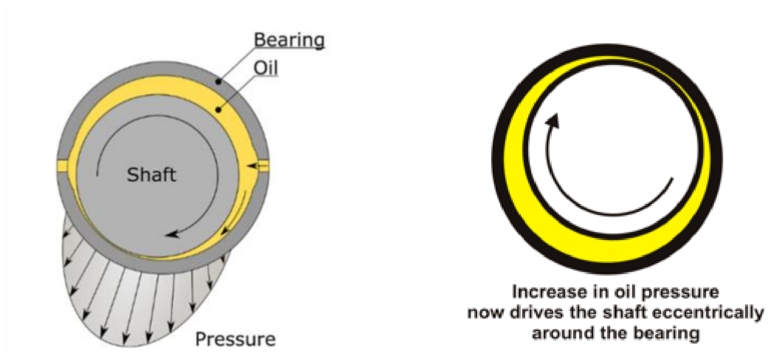

Figure 2.5 : Oil-whip phenomenon

Rotor instability due to thermal strains caused by rubbing was observed by Newkirk in 1926: he spotted a forward whirl induced by a hot spot on the rotor surface, generated in the same point where contact between the rotor and the surroundings happens. This hot-spot instability is therefore called *Newkirk effect*.

During and after the 2nd World War there was a rapid progress in increasing the size and the power density of turbomachinery, in search of technological supremacy and for issues related to the more developed arms race, especially in military aviation.
The theory that explains most fundamental rotordynamics problems had been already published by this time, but the new sophisticated applications brought new and complex challenges in using these theorems to produce practical design analysis.

As an example, the arrival of high-speed rotating machines made it necessary to develop a balancing technique for flexible rotors. In 1945 Prohl published a new method for calculating critical speeds of flexible rotors with many “stations”, consisting of wheels or lumped masses along the rotor shaft. His method is now known as *Transfer Matrix method*. Moreover, up until the fourth decade of the 20th century, most analytical models of critical speeds and whirling eigenvalues had neglected gyroscopic effects of the spinning wheels. With the low-speed machines of the past, the errors in results were generally small and negligible, but now the continuous growth of turbomachinery operating speed requested that the gyroscopic effects to be taken into account. This breakthrough was accomplished by Greene in 1948.

After Frank Whittle and Hans von Ohain developed the jet engine independently of each other, the study of rotordynamics gained even greater momentum, in the search for the development of an engine capable of pushing an aircraft beyond the sound barrier. Success was finally achieved in 1947, when Chuck Yeager pushed his Bell X-1 past Mach 1 over the desert areas of California (**Fig 2.6**).

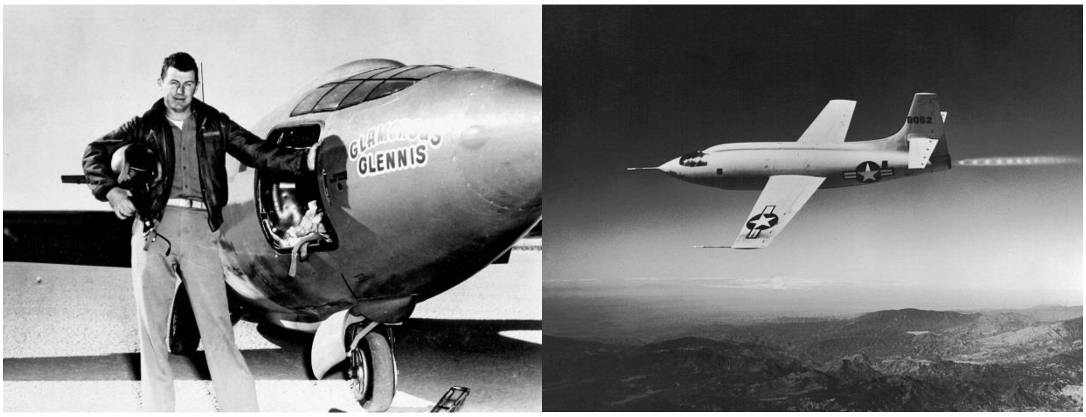

Figure 2.6 : Chuck Yeager and the Bell X-1

In the 1950s it was found that sub-synchronous whirling in steam turbines was somehow related to the steam force on the turbine wheels: a thorough investigation performed by Thomas in Germany showed that a variation of tip clearance around the blades could create a resultant follower force on the whirl orbit, which can unbalance the rotor. This particular kind of instability in steam turbines became known as *steam whirl*.

The design requirements for speed and specific power of turbomachinery equipment have been rapidly increasing since the 1960s, coinciding with the space rush and the race to the moon.

A striking example is the rocket engine turbopumps: the Space Shuttle Main Engine High Pressure Fuel Turbo-Pump (SSME HPFTP) reached speeds of over 35.000 rpm **[8]**, driven by 70.000-hp turbines about the size of a frisbee (**Fig 2.7**).

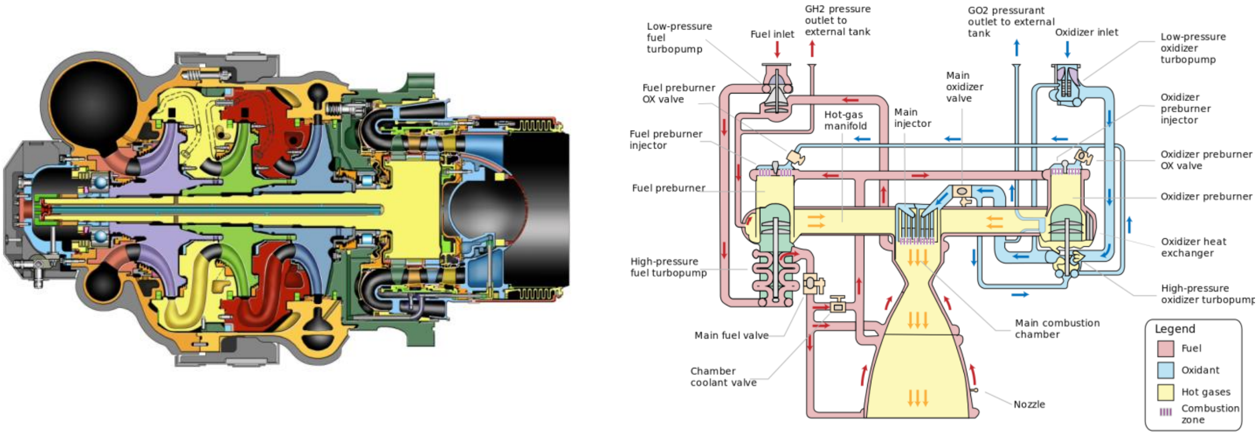

Figure 2.7 : Space Shuttle Main Engine (RS-25) and the powerful HPFTP

These kind of performance result in machines that are likely and easily to be unstable in sub-synchronous whirl. Designing multiple stages on one single shaft result in long, flexible shafts with accentuated bending modes, which makes difficult the suppression of any instability. Because these machines must always be lightweight, the rotors are consequently even more flexible, making balancing more difficult.
The presence of many stages on one shaft produce multiple critical speeds, which in theory can be balanced by having a number of balance planes which is identical to the number of critical speed traversed. In practice, however, is often difficult to realize a large number of balance planes, so some methods have been developed to achieve excellent results with fewer of these planes. The most popular is the *least-square balancing method* published by Goodman at General Electric in 1964, as an extension of the *influent coefficient method*, developed only a few years earlier in the US thanks to the progress of the computers.

In the latter half of the last century, various vibrations due to fluid were studied, but these arguments are well beyond the scope of this work. A more recently developed topic is the study of the non-linear field.

As rotors became lighter and their operational speeds continue to grow higher, the occurrence of nonlinear resonances became a serious problem. Yamamoto studied various kinds of nonlinear resonances after reported on subharmonic resonances due to ball bearings in 1955. He also discussed systems with weak nonlinearity that can be expressed by a power series of low order. In general, it turned out that the most frequent cause of strong nonlinearity in aircraft gas turbines is the radial clearance of squeeze-film damper bearings.

Much more recent is the study of rotordynamics in the non-linear deformation field of the material, which can deform beyond its elastic range given the enormous forces and stresses involved in today's turbomachinery.

This thesis work will be carried out in this precise context, exploiting the potential of the finite element method to perform the calculations of natural frequencies.

During the practical design of rotating machinery it is in fact compulsory to know accurately the values of the natural frequencies, modes, and forced responses to unbalances in complex-shaped rotor systems. The representative techniques used for this purpose are the transfer matrix method and, nowadays, the finite-element method.

The latter was first developed in structural dynamics and then used in almost all fields of modern engineering: the very first application of this method to a rotordynamic problem, a rotor system in particular, was made by Ruhl and Booker in 1972. Since then, the use of FEM in rotordynamics has taken off, and it was generalized by considering rotating inertia, gyroscopic moment and axial forces.

In this chapter, we have tried to briefly summarize the history of rotordynamics: from antiquity, passing through the Renaissance, the industrial revolution, wars and until today, numerous other pages still remain to be written in this exciting field of engineering.

Part II

UNIFIED FORMULATION THEORY

Chapter III

Theoretical References and CUF

We now consider a beam structure with an Ω cross section which lays on the xz plane of a Cartesian reference system (Fig 3.1). As a consequence, for the right-hand-rule, the beam axis is placed along the Cartesian y and it measures L **[11]**.

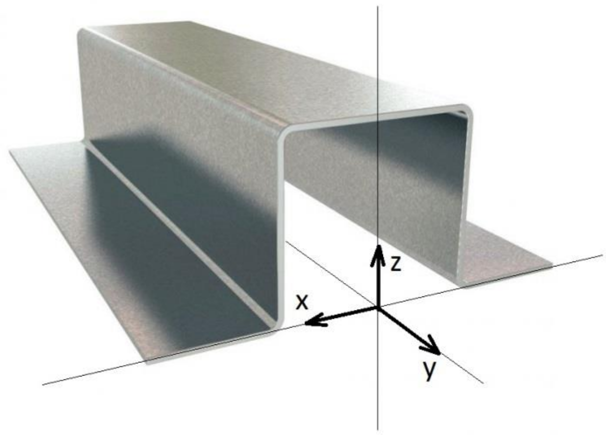

Figure 3.1 : Omega cross sectioned beam

The transposed displacement vector is therefore given by the following expression:

$$\mathbf{u}(x, y, z) = \{u_x \quad u_y \quad u_z\}^T$$

where $u_x \quad u_y \quad u_z$ are the displacement components along the 3 main directions.

The stress, $\boldsymbol{\sigma}$, and engineering strain, $\boldsymbol{\epsilon}$, components are expressed in vectorial form in the same way, with no loss of generality:

$$\boldsymbol{\sigma} = \{\sigma_{xx} \quad \sigma_{yy} \quad \sigma_{zz} \quad \sigma_{xz} \quad \sigma_{yz} \quad \sigma_{xy}\}^T$$

$$\boldsymbol{\epsilon} = \{\epsilon_{xx} \quad \epsilon_{yy} \quad \epsilon_{zz} \quad \epsilon_{xz} \quad \epsilon_{yz} \quad \epsilon_{xy}\}^T$$

In this thesis project, linear elastic metallic beam structures will considered initially. Hence, the Hooke's law provides these constitutive relations:

$$\boldsymbol{\sigma} = \mathbf{C}\boldsymbol{\epsilon}$$

The characters used in this formula are deliberately in bold and not in italics, to indicate the operation between vectors, where the material matrix $\mathbf{C}$ is given by the following:

$$\mathbf{C} = \begin{bmatrix} C_{11} & C_{12} & C_{13} & 0 & 0 & 0 \\ C_{12} & C_{22} & C_{23} & 0 & 0 & 0 \\ C_{13} & C_{23} & C_{33} & 0 & 0 & 0 \\ 0 & 0 & 0 & C_{44} & 0 & 0 \\ 0 & 0 & 0 & 0 & C_{55} & 0 \\ 0 & 0 & 0 & 0 & 0 & C_{66} \end{bmatrix}$$

The coefficients of the stiffness matrix depend only on the Young modulus E and the Poisson ratio ν, in these forms:

$$C_{11} = C_{22} = C_{33} = \frac{(1-\nu)E}{(1+\nu)(1-\nu)}$$

$$C_{12} = C_{13} = C_{23} = \frac{\nu E}{(1+\nu)(1-\nu)}$$

$$C_{44} = C_{55} = C_{66} = \frac{E}{2(1+\nu)}$$

As far as the geometrical relations are concerned, the Green-Lagrange nonlinear strain components are considered. For this reason, the displacement-strain relations are expressed as:

$$\boldsymbol{\epsilon} = \boldsymbol{\epsilon}_l + \boldsymbol{\epsilon}_{nl} = (\mathbf{b}_l + \mathbf{b}_{nl})\mathbf{u}$$

where clearly the l and nl subscripts stand for “linear” and “non-linear”, so $\mathbf{b}_l$ and $\mathbf{b}_{nl}$ are the linear and nonlinear differential operators, respectively. For the sake of completeness, these differential matrix operators are given below:

$$\mathbf{b}_l = \begin{bmatrix} \partial_x & 0 & 0 \\ 0 & \partial_y & 0 \\ 0 & 0 & \partial_z \\ \partial_z & 0 & \partial_x \\ 0 & \partial_z & \partial_y \\ \partial_y & \partial_x & 0 \end{bmatrix} \qquad \mathbf{b}_{nl} = \begin{bmatrix} \frac{1}{2}(\partial_x)^2 & \frac{1}{2}(\partial_x)^2 & \frac{1}{2}(\partial_x)^2 \\ \frac{1}{2}(\partial_y)^2 & \frac{1}{2}(\partial_y)^2 & \frac{1}{2}(\partial_y)^2 \\ \frac{1}{2}(\partial_z)^2 & \frac{1}{2}(\partial_z)^2 & \frac{1}{2}(\partial_z)^2 \\ \partial_x\partial_z & \partial_x\partial_z & \partial_x\partial_z \\ \partial_y\partial_z & \partial_y\partial_z & \partial_y\partial_z \\ \partial_x\partial_y & \partial_x\partial_y & \partial_x\partial_y \end{bmatrix}$$

Obviously, the notation used is that $\partial_x = \frac{\partial(.)}{\partial x}$ $\quad \partial_y = \frac{\partial(.)}{\partial y}$ $\quad \partial_z = \frac{\partial(.)}{\partial z}$

Matrix $\mathbf{b}_l$ and $\mathbf{b}_{nl}$ are also used to define the equilibrium conditions and equations, which can be written in vectorial form invoking a loading vector $\boldsymbol{g}$:

$$(\mathbf{b}_l + \mathbf{b}_{nl})\mathbf{u} = \mathbf{b}^{\mathrm{T}}\boldsymbol{\sigma} = \boldsymbol{g} \qquad \boldsymbol{g}^{\boldsymbol{T}} = \{g_x \quad g_y \quad g_z\}$$

Mechanical boundary conditions must be fulfilled on S_m which represents the portion of the body surface where the mechanical conditions on the loading are given, with normal $\mathbf{n}$ vector.

$$\begin{cases} \sigma_{xx}n_x + \sigma_{yx}n_y + \sigma_{zx}n_z = p_x \\ \sigma_{xy}n_x + \sigma_{yy}n_y + \sigma_{zy}n_z = p_y \\ \sigma_{xz}n_x + \sigma_{yz}n_y + \sigma_{zz}n_z = p_z \end{cases}$$

In this formula $\boldsymbol{p} = \{p_x \quad p_y \quad p_z\}$ is the applied loading vector per unit area on the aforementioned surface S_m.

As stated in reference **[9],** the mechanical and geometrical boundary conditions must be fully defined to complete the set of equations related to the displacement formulation of the 3D problems: these can be obtained by merging Hooke's Law and the strain-displacement relation, obtaining a vectorial formula which represents the boundary-value problem of the 3D elasticity problem, whose solution then leads to the calculation of the deformed configuration, as well as the calculation of the unknown displacements $u_x \quad u_y \quad u_z$.

This equation of elasticity and the related displacement approach can conveniently be formulated by means of the PVW (Principle of Virtual Work) or the PVD (Principle of Virtual Displacement). This variational approach is a very powerful and effective method, which can deal with weak forms and the derivation of Finite-Element (FE) matrices, easily processable by a calculator.

Some multi-dimensional models of aerospace rotordynamic-related structures will be developed using the formalism from the Carrera Unified Formulation (CUF) **[9]**. The CUF provides one-dimensional (beam) and two-dimensional (plates and shells) theories that can extend well beyond the classical theories (Euler, Kirchhoff, Reissner, Mindlin), exploiting a condensed notation. The latter works by expressing the displacement fields in correspondence of the cross section (when we consider a beam) and along the thickness (in the case of plate and shell) in terms of basic functions, whose forms and orders are arbitrary and can be chosen by the user itself. The use of a unified notation leads to the definition of the so-called fundamental nucleus (FN) of all the matrices and FEM vectors involved.

The FNs consist of just a few mathematical statements, whose forms are totally independent from the theory of structures (TOS) employed. The FNs derive from the 3D elasticity equations by the application of the principle of virtual displacements (PVD) and can be easily obtained for many cases, in every number of dimensions considered (1D, 2D or 3D).

Generally, the 1D and 2D Finite-Elements obtained with the CUF present some advanced functionalities, as they are able to achieve results which are usually provided only by 3D elements, but with a much higher computational costs. Moreover, the 1D elements are particularly advantageous as they can deal with 2D and 3D problems in a proper and exact way.

In this master thesis work the 1D elements will be mostly utilized, since the various structures which will be analyzed can be effectively studied using a combination of these simple elements.

The CUF can be defined as a hierarchical formulation, which considers the order of the theory as an input of the analysis: it enables one, at least theoretically, to derive an infinite number of sophisticated displacement models **[10]**. This particularity makes it able to deal with a wide variety of structural problems without the need to introduce specifically designed formulations for each one of them, and right here lies the powerful potential of this theory.

The so-called non-classical effects, such as warping, planar deformations, shear effects, flexural-torsional coupling, are taken in consideration simply increasing the order of the theory in an appropriate manner.

In the first stages of its development, the CUF theory was founded on the use of Taylor-like polynomials to define the range of displacements on the beam cross-section. Static analyzes carried out in the past showed the effectiveness of the theory when dealing with warping phenomena, deformations in the plane and when dealing with effects due to the Shear loading.

Taylor Expansion (TE) models proved to be very efficient when considering prismatic structures, but they also showed some limitations when the rotor components presented different deformability. For this reason the use of Taylor polynomials has some intrinsic limitations, mainly due to the fact that the terms of the expansion of the displacement range do not have always a physical meaning.

In order to overcome these problems it has recently been implemented a new beam theory, which describe the displacement field of the cross section with Lagrange-like polynomials. The choice of these kind of expansions leads us to have only variables of displacements. The component-wise (CW) approach has therefore been extended, within the CUF framework, to the rotordynamics problem, and Lagrange-like polynomial expansions have been adopted to develop the refined displacement theories.

The choice of Lagrange polynomials, besides bringing numerous benefits in terms of versatility of the structural models, allows the user to find even more accurate results than Taylor's expansion-based polynomials models. This permits us to consider many phenomena that otherwise would only be identifiable via 2D or 3D models, with their higher time-consuming and computational cost. In addition, the LE elements allows us to model each structural component of the rotor with an arbitrary degree of accuracy **[10]**, giving us the chance to focus the analysis in pre-established areas, where we think the core of the problem lies and where we can adopt some localized mesh refinements.

Derivation of solid beam finite elements by Carrera unified formulation

In the 1D-CUF framework, the tridimensional displacement field $\mathrm{u}(x,y,z,t) = (u_x, u_y, u_z)$ is approximated with an expansion of generic cross-sectional functions F_τ which allow us to isolate the effect of the axial coordinate y to the shape functions only:

$$3D\ FE: \qquad \mathrm{u}(x,y,z,t) = \mathrm{u}_{i\tau}(t) \cdot N_i(x,y,z) \cdot 1 \qquad i = 1 \dots N_n^{3D}$$

$$1D\ FE: \qquad \mathrm{u}(x,y,z,t) = \mathrm{u}_{i\tau}(t) \cdot N_i(y) \cdot F_\tau(x,z) \qquad i = 1 \dots N_n^{1D}; \qquad \tau = 1 \dots M$$

N_i is the 1D shape function, $\mathrm{u}_{i\tau}$ is the vector of the generalized displacements, M represents the number of terms of the expansion, which is an input by the user, and the index i refers to the FE discretization, varying from 1 to the maximum number of nodes in the finite-element. In accordance with the generalized Einstein's notation, τ indicates summation, while the $F_\tau(x,z)$ are the cross-sectional Lagrange polynomials used to deal with the arbitrary shape geometry. As mentioned before, even if we can use every type of F_τ functions, the connection between the elements becomes very simple when we use Lagrange-type expansions.

In this case, the beam kinematics is obtained as a combination of Lagrange polynomials, which are defined within sub-regions (or elements) delimited by an arbitrary number of points. This number of points determines the order of the polynomial. For the nine-point element L9 shown in the figure below (**Fig 3.2**) the interpolation functions are the following:

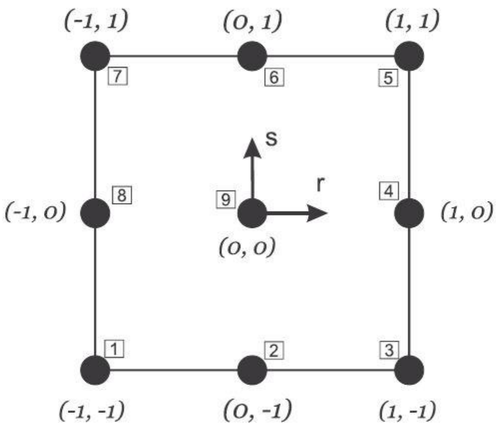

Figure 3.2 : L9 element in the natural coordinate system [10]

$$F_\tau = \frac{1}{4}(r^2 + r\,r_\tau)(s^2 + s\,s_\tau) \qquad \tau = 1,3,5,7$$

$$F_\tau = \frac{1}{2}s_\tau^2(s^2 - s\,s_\tau)(1 - r^2) + \frac{1}{2}r_\tau^2(r^2 - r\,r_\tau)(1 - s^2) \qquad \tau = 2,4,6,8$$

$$F_\tau = (1 - r^2)(1 - s^2) \qquad \tau = 9$$

Here, r and s vary from -1 to $+1$, whereas r_τ and s_τ are the coordinates of the nine points of the element, whose locations in the natural coordinate frame are shown in **Fig 3.2**. As a consequence, the displacement field of the L9 element is:

$$\begin{aligned} u_x &= F_1 u_{x1} + F_2 u_{x2} + F_3 u_{x3} + \cdots + F_9 u_{x9} \\ u_y &= F_1 u_{y1} + F_2 u_{y2} + F_3 u_{y3} + \cdots + F_9 u_{y9} \\ u_z &= F_1 u_{z1} + F_2 u_{z2} + F_3 u_{z3} + \cdots + F_9 u_{z9} \end{aligned}$$

In these equations all the unknowns $(u_{x1}, \dots, u_{x9})$ have the same dimension: they are the displacement variables of the problem and represent the translational displacement of each of the nine points used to define the L9 element of the cross-section. these formulas can now be used to derive the expressions of the normal and tangential strains and stresses: together with Hooke's Law and the application of the classical finite element technique, this leads to the following expression for the generalized ($\mathbf{u}$) and nodal ($\mathbf{q}$) displacement vector.

$$\mathbf{u}(y,t) = N_i(y)\mathbf{q}_{\tau i}(t) \qquad \mathbf{q}_{\tau i}(t) = \{q_{u_{x_{\tau i}}} \quad q_{u_{y_{\tau i}}} \quad q_{u_{z_{\tau i}}}\}^T \qquad \textbf{\textit{Eq.}}\ \mathbf{1}$$

At this point, it should be underlined that the choice of the cross-section polynomials sets for the Lagrange-Expansion kinematics is completely independent of the choice of the beam finite element to be used along the beam axis.

This means that the selection of the type, the number and the distribution of cross-sectional polynomials does not affect the discretization along the y axis: the 1D CW approach has in fact allowed us to greatly simplify the problem, as we can choose whatever elements we find appropriate to describe the kinematics in this axial direction. In this thesis work classical 1D finite elements with four nodes (B4) are adopted, so a cubic approximation along the y-axis is generally assumed.

Geometrically Nonlinear analysis of a structure

Structural analyses are commonly carried out in the linear elastic field, where the following hypothesis are assumed:

- the material is elastic-linear, and its mechanical properties are invariable with respect to the level of stress applied to the structure;
- the equilibrium equations are formulated in the undeformed configuration or, in the case of structures subject to a state of pre-stress, in an initial reference state;
- the deformations to which the structure is subjected are considered "*small*" and do not significantly influence the structural response.

These hypotheses allow considerable and very often valid simplifications in the structural analysis, while the removal of one or more of them leads to the introduction of elements of non-linearity in the analysis. In general, a structural analysis can take into account two types of non-linearity.

The first one is the physical non-linearity of the material, which arises when it presents a non-linear constitutive bond, entering the plastic field once the elastic limit has been exceeded. This effect can be seen on the *stress-strain curve* (**Fig 3.3**) for a specific material, that gives the relationship which holds between the stress applied to it and the strain with it responds.

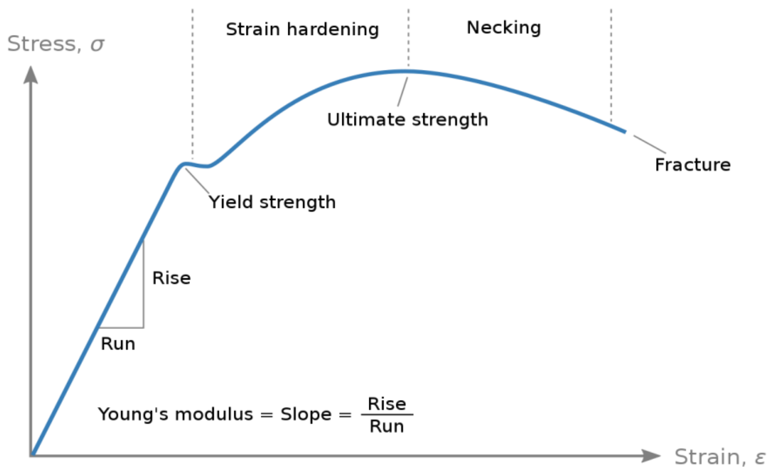

Figure 3.3 : Stress-strain curve of a sample material

These diagram is obtained by gradually applying a load to a test coupon and measuring the deformation: from this two data the stress and strain can be determined and plotted on a graph as a curve, which reveal many of the properties of the material, such as the Young's modulus, the yield strength and the ultimate tensile strength.

The second typology of non-linear effects are those that will be treated in this thesis, namely geometric non-linearity. The before mentioned hypothesis of small displacements is here abandoned, as first order deformations produce a non-negligible displacement of the load application point. It follows that the stresses and displacements of the model need to be recalculated considering the loads applied to the deformed configuration and following an iterative procedure. This phenomenology can occur in the following cases:

- in presence of large displacements, when there is a big difference between the undeformed and the deformed configuration of the structure;
- when the so-called follower forces arises and the deformation changes the direction of the load with respect to the undeformed configuration;
- In general, the stress-state of the structure always introduces a side effect, which can be defined as stress stiffening or stress softening. For example, from previous studies we know that the rotation and the consequent centrifugal forces that derive from it tend to stiffen the structure, increasing the value of the natural frequencies.
  We therefore expect to find this trend in the analysis of the Campbell diagrams that will be carried out in the following chapters. On the other hand, stress softening can manifest itself, for example, with elastic instability and buckling (**Fig 3.4**) produced by the compression-state.

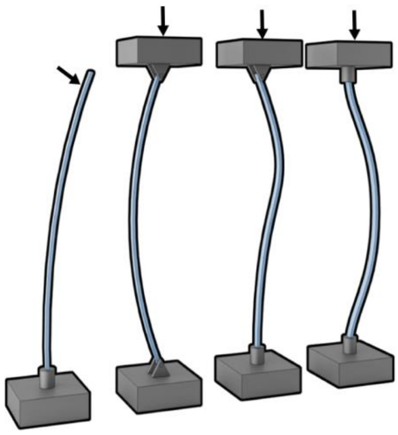

Figure 3.4 : Geometrical Nonlinearity example =Buckling

In most cases, the structural analyses are limited to the study of small displacement field. However, today's engineering applications, especially in rotor components, have reached rotational speeds and applied forces so high that they can deform the structure substantially, radically changing its dynamic properties.

A geometrically non-linear FEM analysis allows us to consider the increase or reduction in stiffness due to the stress-state related to large displacement, and it is therefore very important to have suitable tools to analyze this situation as well, as it implies a much more in-depth and complex mathematical treatment.

This type of analysis leads to results that are strictly dependent on the basic hypotheses from which we started and consequently it will be necessary to pay particular attention to their validation: as we said, the geometrically non-linear analysis provides looser assumptions only regarding the deformations magnitude, while it predicts that the material always remains in the linear-elastic range, where the stress-strain graph takes the form of a straight line.

Nonlinear Governing Equations of Vibrating Structures

Consider now an elastic system which is in equilibrium under a set of applied forces and some prescribed geometrical constraints. The principle of virtual work (PVW) establishes the well-known equilibrium condition between the virtual variations of works done by the deformations δL_{int}, inertia δL_{ine} and external forces δL_{ext}. In particular, the PVW states that **[12]**:

$$\delta L_{int} = \delta L_{ine} + \delta L_{ext} \qquad \textbf{\textit{Eq.2}}$$

In this case, the strain energy is defined as the body volume integral of the virtual strains multiplied by the stress vector, according to the following formulation:

$$\delta L_{int} = \langle \delta \varepsilon^T \sigma \rangle \qquad where \qquad \langle (\dots) \rangle = \int_V (\dots) dV$$

If we apply the hypothesis of small deformations, using the Green-Lagrange nonlinear strain components already mentioned in the previous pages the displacement-strain relation becomes

$$\boldsymbol{\varepsilon} = \varepsilon_l + \varepsilon_{nl} = (\mathrm{b}_l + \mathrm{b}_{nl})\mathbf{u} = \left(\boldsymbol{B}_l^{\tau i} + \boldsymbol{B}_{nl}^{\tau i}\right)\mathbf{q}_{\tau i}$$

While the 3D constitutive equation is still given by the well-known Hooke's Law formula:

$$\sigma = \boldsymbol{C}\varepsilon$$

In this case, $\boldsymbol{B}_l^{\tau i}$ and $\boldsymbol{B}_{nl}^{\tau i}$ are the linear and nonlinear matrices obtained within the CUF finite element method framework as described above, while $\boldsymbol{C}$ is the 6×6 matrix of linear elastic material coefficients. Substituting these equations into the $Eq.2$ and using the s and j indexes for the terms related to the virtual variation, we obtain that:

$$\begin{aligned} \delta L_{int} &= \langle \delta \varepsilon^T \sigma \rangle = \delta \mathbf{q}_{sj}^T \left\langle \left(\boldsymbol{B}_l^{sj} + 2\boldsymbol{B}_{nl}^{sj}\right)^T \boldsymbol{C}\left(\boldsymbol{B}_l^{\tau i} + \boldsymbol{B}_{nl}^{\tau i}\right) \right\rangle \mathbf{q}_{\tau i} \\ &= \delta \mathbf{q}_{sj}^T\, \mathbf{K}_0^{ij\tau s} \mathbf{q}_{\tau i} + \delta \mathbf{q}_{sj}^T\, \mathbf{K}_{\boldsymbol{lnl}}^{ij\tau s} \mathbf{q}_{\tau i} + \delta \mathbf{q}_{sj}^T\, \mathbf{K}_{nll}^{ij\tau s} \mathbf{q}_{\tau i} + \delta \mathbf{q}_{sj}^T\, \mathbf{K}_{nlnl}^{ij\tau s} \mathbf{q}_{\tau i} \qquad \textbf{\textit{Eq.3}} \\ &= \delta \mathbf{q}_{sj}^T\, \mathbf{K}_S^{ij\tau s} \mathbf{q}_{\tau i} \end{aligned}$$

In this last equation several K matrices appear, which will now be analyzed in detail: the secant stiffness matrix $\mathbf{K}_S^{ij\tau s}$ includes the linear terms $\mathbf{K}_0^{ij\tau s}$, the two first-order nonlinear contributions $\mathbf{K}_{\boldsymbol{lnl}}^{ij\tau s}$ and $\mathbf{K}_{nll}^{ij\tau s}$, and the second-order nonlinear matrix, given by $\mathbf{K}_{nlnl}^{ij\tau s}$. These are 3×3 arrays, called Fundamental nuclei (FN) and their expressions are not affected by the type or the number of functions which we decided to use for the kinematic expansion. As a consequence, every type of beam theories can be automatically implemented by exploiting the indicial notation of this unified formulation.

If we are looking for a non-linear solution, we must necessarily identify the equilibrium point reached by the structure, and then consider the oscillations around this point. In fact, similarly to that of the internal forces, the virtual work done by the inertial forces $\boldsymbol{F_I}$ is defined as the body volume of the small perturbations vector around a steady nonlinear equilibrium position $\hat{\mathbf{u}}^T = [\widehat{u_x} \quad \widehat{u_y} \quad \widehat{u_z}]$, multiplied by the expression of the inertial forces itself:

$$\delta L_{ine} = \langle \delta \hat{\mathbf{u}}^T \boldsymbol{F_I} \rangle = \int_V (\delta \hat{\mathbf{u}}^T \boldsymbol{F_I}) dV \qquad \boldsymbol{Eq. 4}$$

All these terms are expressed with respect to a coordinate reference frame attached to the rotor that rotates at constant speed Ω about its y-axis. According to that, the inertial forces are given by:

$$\boldsymbol{F_I} = -\rho \begin{pmatrix} \ddot{\widehat{u_x}} \\ \ddot{\widehat{u_y}} \\ \ddot{\widehat{u_z}} \end{pmatrix} - 2\rho\Omega \begin{pmatrix} -\dot{\widehat{u_z}} \\ 0 \\ \dot{\widehat{u_x}} \end{pmatrix} + \rho\Omega^2 \begin{pmatrix} \widehat{u_x} \\ 0 \\ \widehat{u_z} \end{pmatrix} + \rho\Omega^2 \begin{pmatrix} x_e \\ 0 \\ z_e \end{pmatrix} \qquad \boldsymbol{Eq. 5}$$

Combining and merging $Eq. 1, 4$ and 5 the FN of the mass matrix $\boldsymbol{M}^{ij\tau s}$ is readily obtained, as well as the Coriolis matrix $\boldsymbol{G}^{ij\tau s}$, the centrifugal matrix $\boldsymbol{K}_{\boldsymbol{\Omega}}^{ij\tau s}$ and the vector of centrifugal forces $\boldsymbol{F}_{\boldsymbol{\Omega}}^{js}$.

We now have all the ingredients needed to carry out our goal: the non-linear analysis. If any external loads $\boldsymbol{F}_{\text{ext}}^{js}$ are applied to the structure, the nonlinear equation to be solved becomes:

$$\boldsymbol{K}_S \mathbf{q}_e = \boldsymbol{F}_{ext} + \boldsymbol{F}_\Omega$$

However, this formulation is still too complex to be solved analytically, as we explained how the $\mathbf{K}_S$ matrix still contains all the non-linear terms: the solution $\mathbf{q}_e$ needs to be determined through a Newton-Raphson incremental scheme, which requires the linearization of $Eq. 3$:

$$\begin{aligned} \delta(\delta L_{int}) &= \langle \delta \boldsymbol{\varepsilon}^T \delta \boldsymbol{\sigma} \rangle + \langle \delta(\delta \boldsymbol{\varepsilon}^T) \boldsymbol{\sigma} \rangle \\ &= \delta \mathbf{q}_{sj}^T \left(\mathbf{K}_0^{ij\tau s} + \mathbf{K}_{T_1}^{ij\tau s} + \mathbf{K}_\sigma^{ij\tau s} \right) \delta \mathbf{q}_{\tau i} \\ &= \delta \mathbf{q}_{sj}^T \, \mathbf{K}_T^{ij\tau s} \delta \mathbf{q}_{\tau i} \end{aligned} \qquad \boldsymbol{Eq. 6}$$

Here we introduced the tangent stiffness matrix, $\mathbf{K}_T^{ij\tau s}$, whose fundamental nucleus includes the before mentioned nonlinear contribution of the Hooke's law, the linear stiffness matrix $\mathbf{K}_0^{ij\tau s}$ and the geometric stiffness matrix $\mathbf{K}_\sigma^{ij\tau s}$.

The analysis of this thesis is aimed at the calculation of the natural frequencies of some structural models. These natural frequencies ω and mode shapes $\bar{q}$ associated with small-amplitude vibrations are significantly affected by the equilibrium point they oscillate about, and can be obtained assuming a harmonic solution for the following dynamic equation:

$$\boldsymbol{M}\ddot{\hat{\boldsymbol{q}}} + \boldsymbol{G}\dot{\hat{\mathbf{q}}} + (\boldsymbol{K}_{\boldsymbol{T}}(\mathbf{q}_{\mathrm{e}}) + \boldsymbol{K}_{\boldsymbol{\Omega}})\hat{\mathbf{q}} = \mathbf{0} \qquad \hat{\mathbf{q}} = \bar{\mathbf{q}}\, e^{i\omega t} \qquad \boldsymbol{Eq.7}$$

This formulation holds for large displacements and large rotations of the structure until reaching its equilibrium state, around which only small vibrations are allowed.

In the following chapters comparative analyses between non-linear theory and linearized theory will often be carried out. In fact, in order to reduce the computational effort and the mathematical complexity, this last $Eq.7$ can be linearized, considering only the linear part of the geometric stiffness matrix $\mathbf{K}_{\sigma}$.

$$\mathbf{K}_{T} = \mathbf{K}_{0} + \mathbf{K}_{T_1} + \mathbf{K}_{\sigma} \qquad Nonlinear$$
$$\mathbf{K}_{T} \approx \mathbf{K}_{0} + \mathbf{K}_{\sigma}^{*} \qquad Linearized$$

This new geometric stiffness matrix $\mathbf{K}_{\sigma}^{*}$ derives from the geometric strain energy, obtained by the product between the nonlinear component of strains $\boldsymbol{\varepsilon}_{nl}$ and the initial stress vector $\boldsymbol{\sigma}_{0}$. The computation of the rotation-induced stresses is performed by a static linear analysis in which the rotation force F_{Ω} appears.

$$(\mathbf{K}_{0} + \mathbf{K}_{\Omega})|_{\Omega=1}\hat{\mathbf{q}} = \boldsymbol{F}_{\Omega}|_{\Omega=1}$$

It is important to specify that the newly obtained $\mathbf{K}_{\sigma}^{*}$ matrix differs from the previous one $(\mathbf{K}_{\sigma})$ because in this particular case the stress field is computed only considering the linear part of the strain field, since the problem is being linearized. The dynamic system therefore becomes linearized, which means that it is analytically solvable, and requires much less computational effort:

$$\boldsymbol{M}\ddot{\hat{\boldsymbol{q}}} + \boldsymbol{G}\dot{\hat{\mathbf{q}}} + (\mathbf{K}_{0} + \Omega^{2}\mathbf{K}_{\sigma}^{*} + \boldsymbol{K}_{\boldsymbol{\Omega}})\hat{\mathbf{q}} = \mathbf{0} \qquad \hat{\mathbf{q}} = \bar{\mathbf{q}}\, e^{i\omega t} \qquad \boldsymbol{Eq.8}$$

The Assembly Procedure

The structural configuration of **Fig 3.5** is now used to explain the assembly procedure of the various matrix involved in the previous dynamic systems. Theoretically speaking, a prismatic structure can be modeled with beam or solid elements: in this example one Lagrange element with 4 nodes (L4) is used on the cross-section, while 2 beam elements with two nodes are used to model our structures along its longitudinal axis. The image shows that the every beam model has four nodes in each transversal section. The unknown displacements are, therefore, given by:

$$u_i = (u_x \quad u_y \quad u_z)_{i\tau} \qquad i = 1,2,3,4 \quad \tau = 1,2,3,4$$

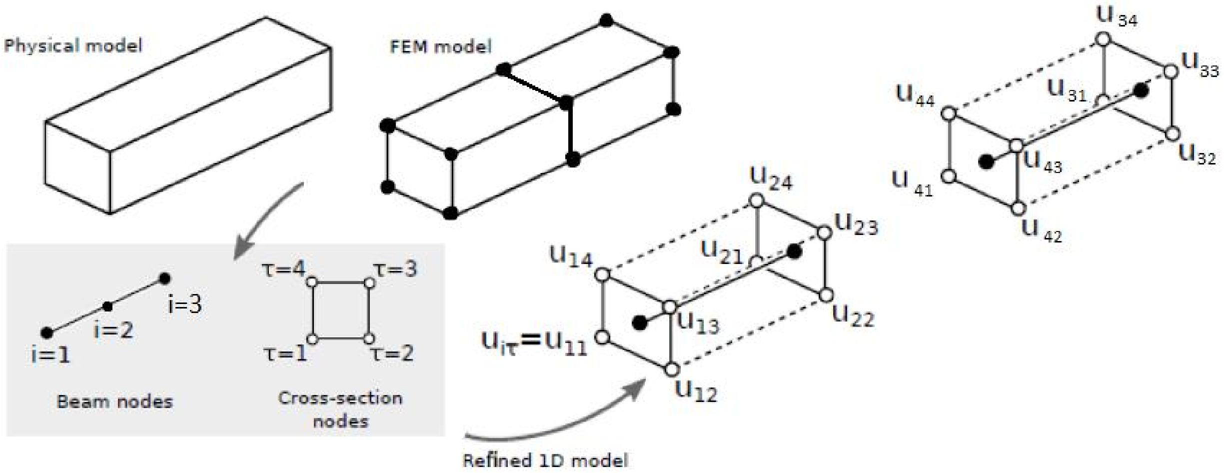

Figure 3.5 : Example of a 1D Lagrange Expansion FEM model

Otherwise, we also could have modeled the structure with a generic number of 3D elements, with 8 nodes each. The latter is usually the strategy of commercial FEM codes, which automatically generate a very dense mesh with a huge number of elements, that determines an increase in the computational cost.

For this reason, now we want to focus on the numerical procedure that allows us to derive and assemble the stiffness and mass matrices of the entire structure, starting from the 1D and Lagrange elements, that will be used in the course of this thesis.

As both beam models have the same unknowns, the imposition of the compatibility condition between shared nodes is very simple, considering that nodes 2 and 4 coincides in the final assembled model:

$$u_{21} = u_{41} \qquad u_{22} = u_{42} \qquad u_{23} = u_{43} \qquad u_{24} = u_{44}$$

These conditions can be used during the assembly procedure to identify the nodes to be connected (Fig 3.6). As usually done in finite element solution schemes, the matrices of the two elements can be used to build the global matrix of the entire structure simply adding the contributions of the shared nodes.

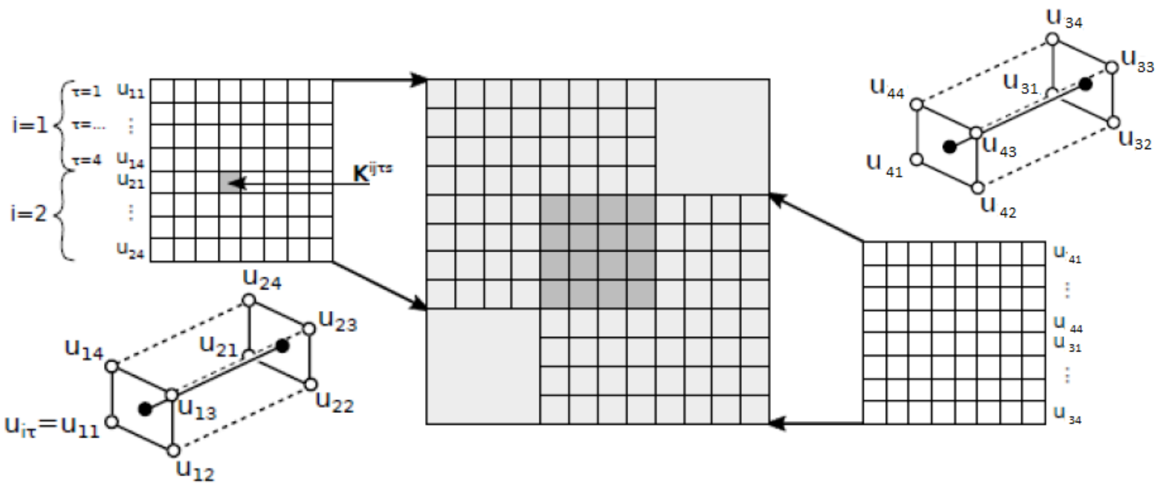

Figure 3.6 : Assembly procedure for the 1D Lagrange Expansion FEM model

Since the assembled mathematical model of this simple example has twelve structural nodes (SN), the total number of degrees of freedom will be:

$$DoF = SN \times 3 = 12 \times 3 = 36$$

Part III

STATIC AND DYNAMIC ANALYSES

Chapter IV

Validation

In this chapter many analyses will be carried out in order to obtain the natural frequencies of some structures with particularly simple geometries. Some reference results, obtained from previous papers by Filippi, Carrera, Entezari and others **[13]**, **[14]**, are available in the bibliography, and will be used to compare and validate the new code, initially still in its linear analysis configuration.

During these first steps, particular attention will be paid to describing the construction processes of the FEM model and the mesh of the section used, crucial for the good functioning of the Mul2 code.

This code allows to perform structural and free-vibrations analysis through the application of the CUF (Carrera Unified Formulation), which, as we said, is a very powerful and capable tool, which can drastically reduce the computational cost of these calculations.

As we are working with 3D structures, models with Lagrange series expansions were chosen, which showed good adherence with the results obtained with commercial FEM software such as Ansys or Femap.

Free vibration analysis of a longeron

Following the first example of the CUF book **[9]**, we start our validation with the free vibration analysis of a longeron with three longitudinal stiffeners. The geometry of the structure is shown in the following picture (**Fig 4.1**), and it has been modelled as a beam, only clamped at its end at $y = 0$. The geometrical characteristics are:

- Axial length $L = 3\ m$
- Cross sectional height $h = 1\ m$
- Area of the stringers $A_S = 1{,}6\ \cdot 10^{-3}\ m^2$
- Thickness of the panels $t = 2 \cdot 10^{-3}\ m$
- Distance b $b = 0.18\ m$

The whole structure is made of an Aluminum Alloy, which is an isotropic material, endowed with these properties:

$$E = 75\ GPa, \qquad \nu = 0.33, \qquad \rho = 2700\,\frac{Kg}{m^3}$$

It should be remembered that this structure was analyzed as a first test, only to learn how to use the code provided by the university department. The component-wise CW model was obtained by discretizing the cross section with 5 L9 elements one for each spar component (stringers and webs) following the model of the book. This results in 41 points for each station of the beam.

A 10 B4 mesh (31 nodes) is adopted along the y-axis, since it leads to convergent results in terms of natural frequencies, when a free-vibration analysis is performed.
After some simple calculations necessary to obtain the unspecified dimensions, it was possible to define the mesh and the coordinates of each node of the structure. The discretization used leads to having a quite large number of degrees of freedom (DOFs), which is calculated in this way:

$$41\,\frac{points}{node} * 31\,nodes * 3\,\frac{DOF}{point} = 3813\ \ DOFs$$

Performing the analysis using the Mul2 code, among other results, a *paraview* file is also generated with the natural modes, which can be displayed using the software of the same name (**Fig 4.2**).

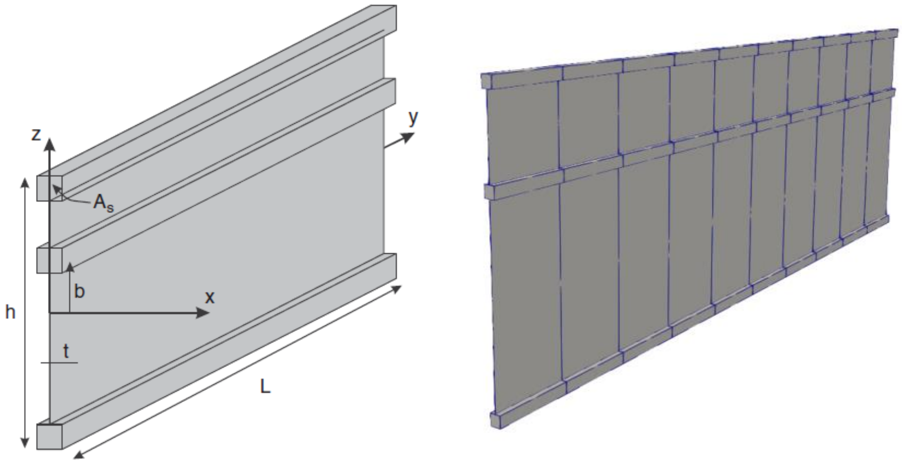

Figure 4.1 = Three-stringer spar

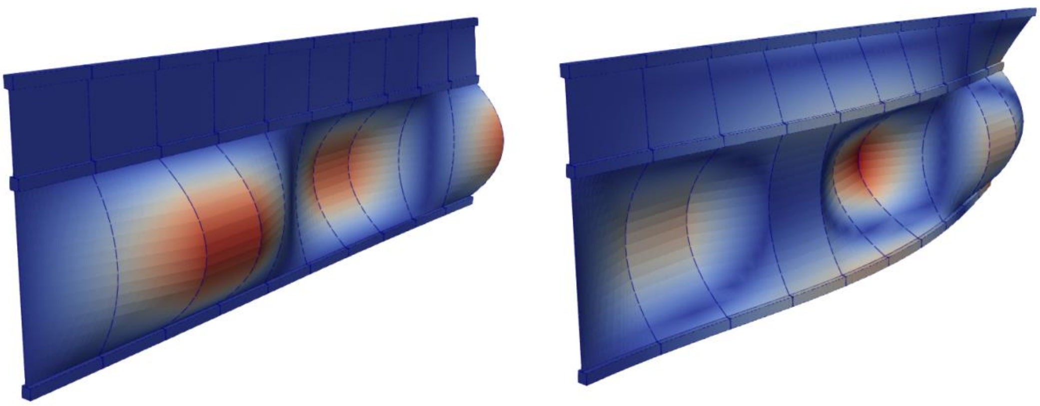

Figure 4.2 = Natural modes in Paraview: mode 6 (17.67 Hz) and mode 10 (25.1 Hz)

The first 15 natural frequencies of this structure have been calculated with the Mul2 code and compared with the results reported in **Fig 4.3**, taken from reference **[9]**. It shows the values of different modes (b: bending modes; t: torsional mode; s: shell-like mode; e: extensional mode).

	EBBT	TBT	$N=1$	$N=2$	$N=3$	$N=4$	5 L9	Solid
DOFs	93	155	279	558	930	1395	3813	62 580
Mode								
1	3.24^b	3.24^b	3.24^b	3.43^b	3.35^b	3.31^b	3.46^t	3.15^b
2	20.29^b	20.28^b	20.28^b	16.70^t	16.34^t	16.13^t	3.52^b	3.55^t
3	56.81^b	56.74^b	56.74^b	21.39^b	20.97^b	20.75^b	3.76^b	3.82^b
4	111.36^b	108.81^b	108.81^b	55.25^t	52.90^t	51.70^t	14.27^s	13.30^s
5	117.60^b	111.11^b	111.11^b	60.11^b	59.23^b	58.24^b	16.73^s	15.06^s
6	184.30^b	183.57^b	183.57^b	108.19^t	100.81^t	97.87^t	17.67^s	16.33^s
7	275.94^b	274.23^b	269.29^t	109.44^b	105.55^b	102.26^b	21.17^s	19.81^s
8	386.89^b	383.36^b	274.23^b	117.79^b	116.61^b	113.20^b	21.71^t	21.49^t
9	439.21^e	439.20^e	383.36^b	181.03^t	165.23^t	119.39^s	22.95^b	22.81^b
10	517.91^b	455.17^b	439.20^e	194.59^b	183.16^s	161.07^t	25.11^s	24.07^s
11	622.84^b	511.36^b	455.17^b	276.03^t	197.98^b	176.65^s	25.73^s	24.63^s
12	669.05^b	658.20^b	511.36^b	290.25^b	229.97^s	189.01^b	31.21^s	29.69^s
13	830.95^b	817.28^b	658.20^b	325.69^s	248.76^t	243.58^t	37.92^s	36.24^s
14	1104.56^b	972.68^b	807.88^t	393.92^t	290.54^b	258.64^s	45.79^s	43.88^s
15	1317.62^e	1055.78^b	817.28^b	406.78^b	302.06^s	281.59^b	54.86^s	51.64^s

Figure 5.3 : First 15 natural frequencies (Hz) of the three-stringer spar [9]

A summary of these results and the relative error is shown in the table below (**Tab 4.1**):

Frequency	*RESULTS*	*REFERENCE [9]*	*ERROR [%]*
1	3.16804	3.46	-8.43829
2	3.83044	3.76	1.87333
3	3.56010	3.52	1.13918
4	14.26918	14.27	-0.00574
5	16.73470	16.73	0.02809
6	17.67062	17.67	0.00353
7	21.16814	21.17	-0.00880
8	21.69645	21.71	-0.06240
9	22.94795	22.95	-0.00895
10	25.09775	25.11	-0.04877
11	25.74817	25.73	0.07061
12	31.20558	31.21	-0.01415
13	37.91634	37.92	-0.00966
14	45.78556	45.79	-0.00970
15	54.84760	54.86	-0.02261

Table 4.1 : Free vibration analysis of the three-stringer longeron

Except for the value of the first natural frequency, all the others have a limited and perfectly acceptable percentage error, probably due to the different hardware architecture of the computers on which the code was run.

Structural analysis of a Thin and Thick-walled Cylinder

A thin-walled cylinder is considered with the cross-section geometry shown in the figure on the right (**Fig 4.4**) taken from ref. **[9]**, where the diameter, d, is equal to $2\ m$, and the thickness, t, is equal to $0.02\ m$. The length of the cylinder, L, is equal to $20\ m$. The structure has been modelled as a clamped-clamped beam made of an aluminum alloy, which is an isotropic material:

$$E = 75\ GPa, \qquad \nu = 0.33, \qquad \rho = 2700\frac{Kg}{m^3}$$

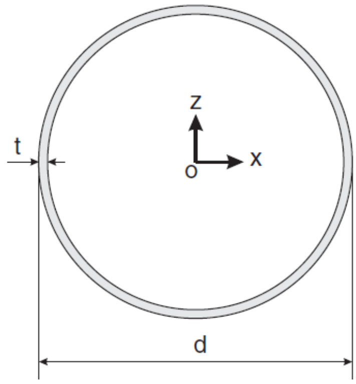

Figure 4.4 : Thin-walled cylinder

As a reference, the same free-vibration analysis has been performed over a thick-walled cylinder, which has the same diameter and length as the previous, while the thickness, t, is now equal to $0.3\ m$.

FEM model and MESH construction:

The co-rotating reference system allows the analysis of axisymmetric structures, therefore a Cartesian system has been adopted, placing the y-axis in coincidence with the longitudinal axis of the beam, while the x and z-axes define the circular cross section.

A 10 B4 mesh (31 nodes) is adopted along the y-axis, since it leads to convergent results in terms of natural frequencies, when a free-vibration analysis is performed. Given the geometry of the structure, a null value of the x and z coordinates has been attributed to each node, making only the longitudinal coordinate vary.

For the cross section 8×1 **L16** elements were used in the circumferential and radial direction respectively, each formed by 16 nodes, defined by a corresponding number of coordinate triples (**Fig 4.5**). Using MATLAB, a software has been created to generate the mesh of the section by acting only on a few parameters, which will be used several times also in subsequent analyzes.

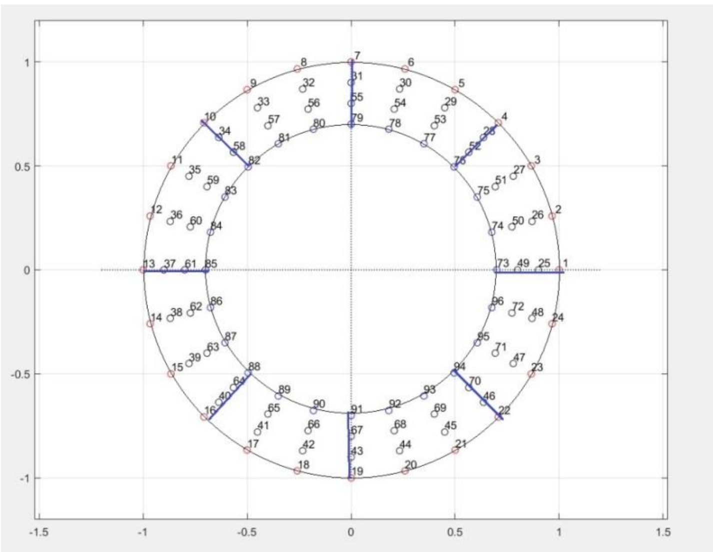

Figure 4.5 : 8 X 1 L16 Mesh

It is also very important to accurately define the connectivity matrix among the elements, in order to correctly describe the section to be analyzed. Most of the pre-processing time is spent in this phase, and the effort is shown in the following table (**Tab 4.2**).

TYPE	N°	Number of the 16 Nodes which define the element															
Q16	1	1	2	3	4	28	52	76	75	74	73	49	25	26	27	51	50
Q16	2	4	5	6	7	31	55	79	78	77	76	52	28	29	30	54	53
Q16	3	7	8	9	10	34	58	82	81	80	79	55	31	32	33	57	56
Q16	4	10	11	12	13	37	61	85	84	83	82	58	34	35	36	60	59
Q16	5	13	14	15	16	40	64	88	87	86	85	61	37	38	39	63	62
Q16	6	16	17	18	19	43	67	91	90	89	88	64	40	41	42	66	65
Q16	7	19	20	21	22	46	70	94	93	92	91	67	43	44	45	69	68
Q16	8	22	23	24	1	25	49	73	96	95	94	70	46	47	48	72	71

Table 4.2 : Connectivity Matrix (Thin and Thick walled Cylinder)

The first 30 natural modes and natural frequencies have been evaluated and are reported below for the two case studies: since in this case no paper with previously obtained results was available, an ANSYS parallel analysis was performed to compare the frequencies and the approximation introduced by the MUL2 code (**Fig 4.6**).
In doing this, it was noted the absolute importance of defining an axisymmetric mesh in ANSYS in order to obtain natural modes with multiplicity equal to 2.

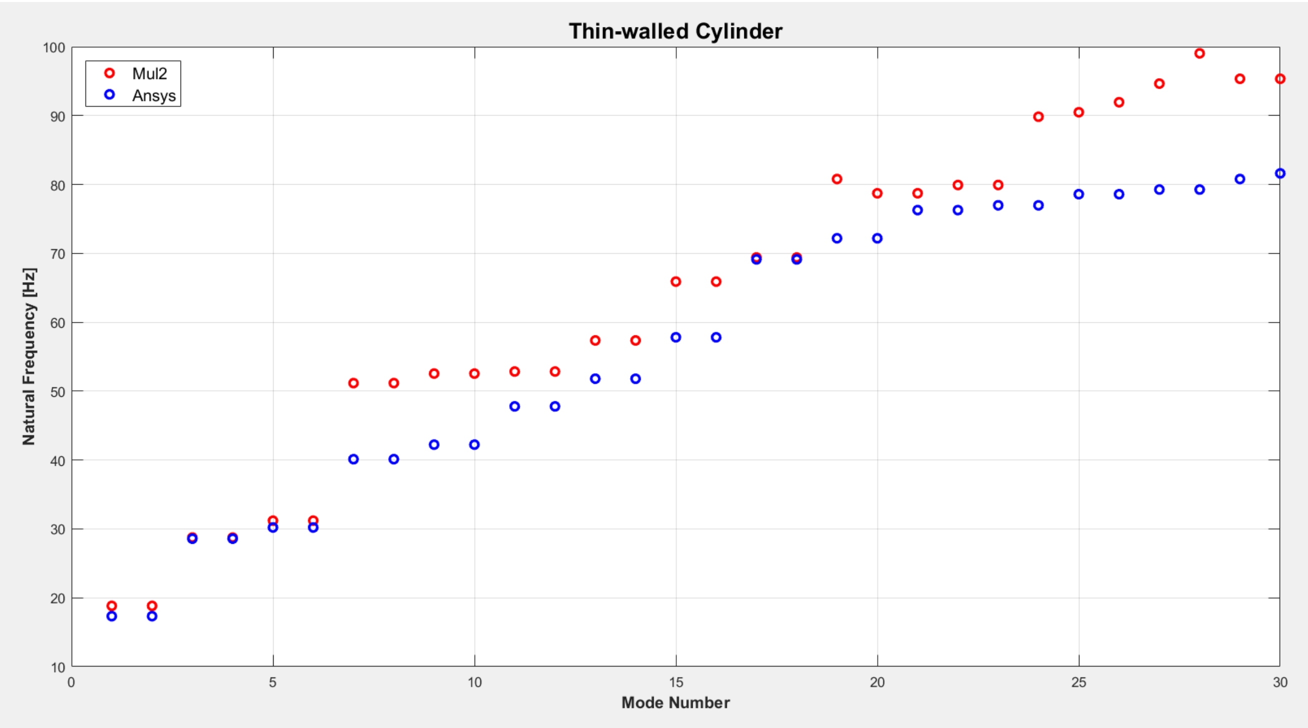

Figure 4.6 : Thin-walled Cylinder Natural Frequency Chart [Hz]

From the previous graph we can see that there is a significant difference between the two codes. Analyzing and identifying in detail the natural modes we can obtain the following result:

Natural Mode	*Identification*	*Wave number*	*MUL 2*	*ANSYS*	*Rel. Error [%]*
1	Shell	I	18.828	17.331	8.64
2	Bending	I	28.747	28.583	0.57
3	Shell	II	31.197	30.206	3.28
4	3 Lobe Shell	I	51.165	40.119	27.53
5	Shell	III	52.547	51.8	1.44
6	3 Lobe Shell	II	52.842	42.234	25.12
7	3 Lobe Shell	III	57.359	47.784	20.04
8	3 Lobe Shell	IV	65.896	57.811	13.99
9	Bending	II	69.4	69.125	0.40
10	3 Lobe Shell	V	78.721	72.187	9.05
11	Shell	IV	79.925	79.263	0.84
12	Torsion	I	80.788	80.788	0.00
		NODES	2976	30780	
		DOFs	8928	92340	

Table 4.3 : Natural Frequency results for the Thin-walled Cylinder [Hz]

Within the table (**Tab 4.3**), the rows related to bending and torsional modes have been highlighted to underline the very limited relative error obtained between the two FEM codes, despite the large differences in computational cost, presented through the number of degrees of freedom (DOFs) in the bottom right corner.

Thanks to this analysis it can be seen that the shell-like modes need a specific treatment, since they aren't captured precisely by this particular application of the Lagrange-expansion based Mul2 software. However, the magnitude of this error behaves in a way which is inversely proportional to the number of half waves, as confirmed, for example, by the frequency values of the Shell IV mode. For the sake of completeness, some vibrational modes of the analyzed structure are shown on the next page (**Fig 4.7**).

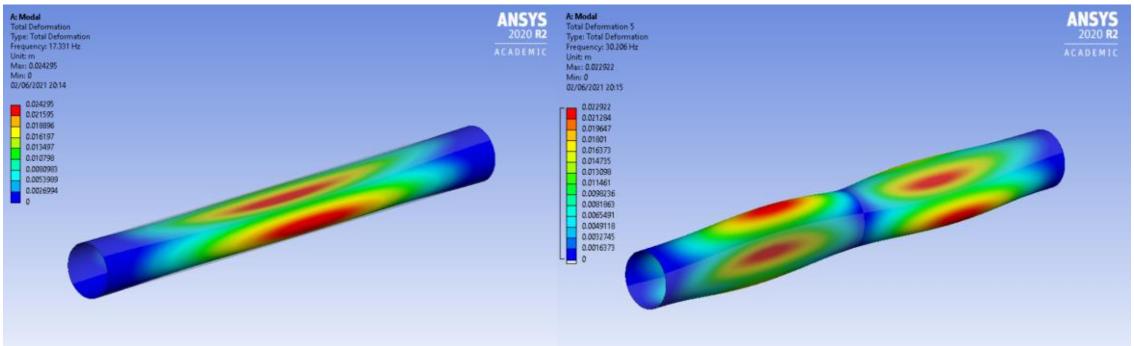

Shell mode: I and II

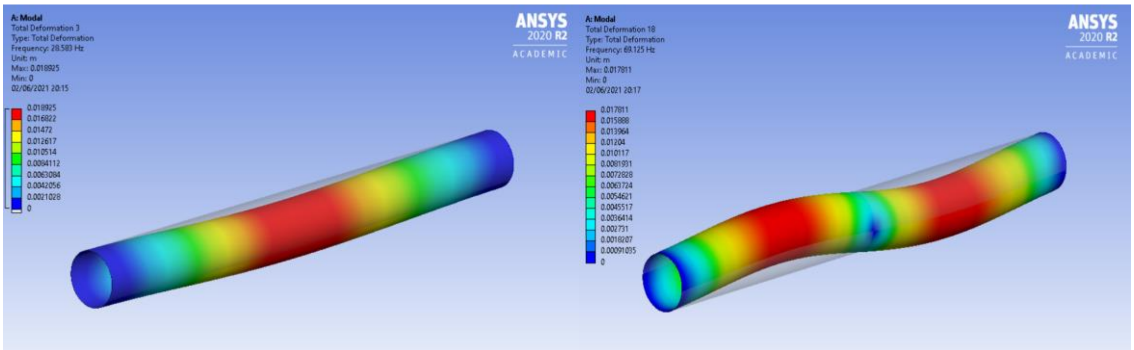

Bending mode: I and II

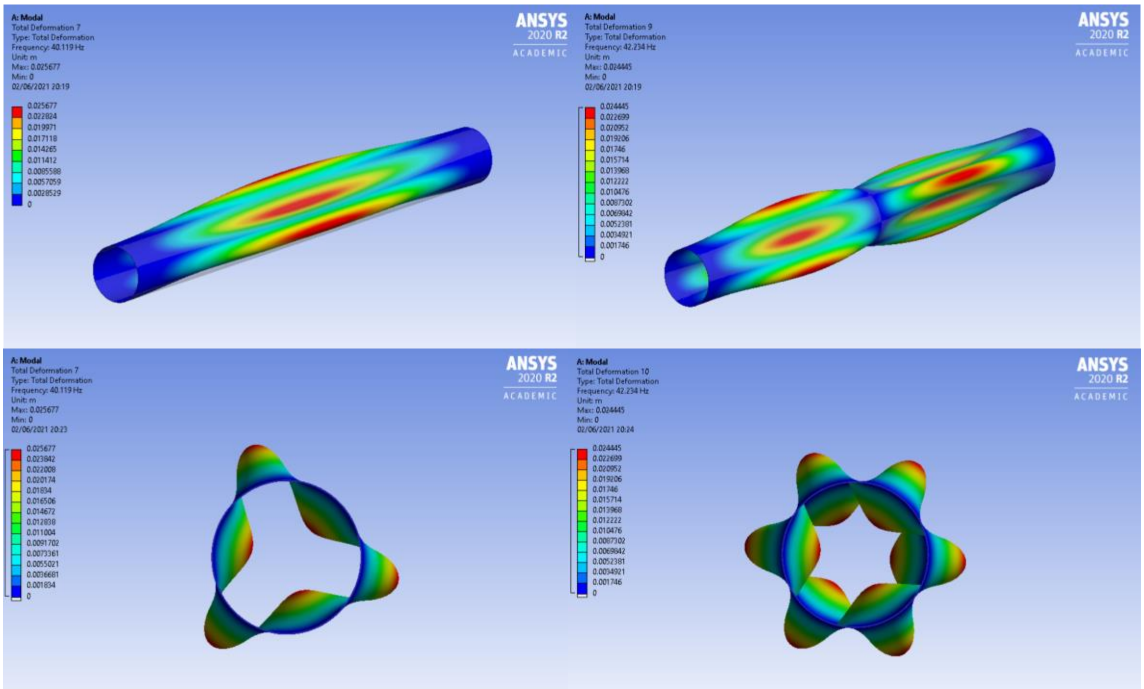

3 Lobe Shell mode (with sections): I and II & Torsional mode (below)

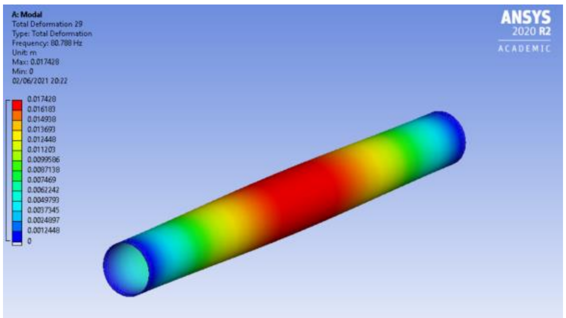

Figure 4.7 : Thin-walled Cylinder modes (ANSYS)

The same analysis was performed on the ***thick-walled cylinder*** described above. Looking at the graph of the results (**Fig 4.8**), one can immediately notice an increase in natural frequencies values caused by the greater thickness and therefore by the greater stiffness of the structure. As a very first approximation it is in fact possible to consider this beam as a 1-DOF dynamic system, whose next formulation for the natural frequency is well known:

$$\omega = \sqrt{\frac{k}{m}}$$

We also notice a minor difference between the results of the two codes, and this occurs because the shell modes, which we have seen to be the most problematic, tend to occur at higher frequencies, while they were dominant in the thin-walled cylinder dynamics (**Tab 4.4**)

Natural Mode	***Identification***	***Wave number***	***MUL 2***	***ANSYS***	***Rel. Error [%]***
1	Bending	I	26.12	26.015	0.40
2	Bending	II	64.86	64.645	0.33
3	Torsion	I	80.79	80.785	0.01
4	Bending	III	114.18	113.89	0.25
5	Torsion	II	161.58	161.57	0.01
6	Bending	IV	169.7	169.35	0.21
7	Bending	V	229	228.61	0.17
8	Torsion	III	242.37	242.36	0.00
9	Shear	I	264.27	263.68	0.22
10	Shell	I	272.42	270.87	0.57
11	Shell	II	276.37	274.84	0.56
12	Shell	III	284.22	282.72	0.53
13	Bending	VI	290.4	289.93	0.16
14	Shell	IV	297.18	295.71	0.50
15	Shell	V	316.07	314.61	0.47
16	Torsion	IV	323.16	323.14	0.01
17	Shell	VI	341.16	339.67	0.44
		NODES	2976	26884	
		DOF	8928	80652	

Table 4.4 : Natural Frequency results for the Thick-walled Cylinder [Hz]

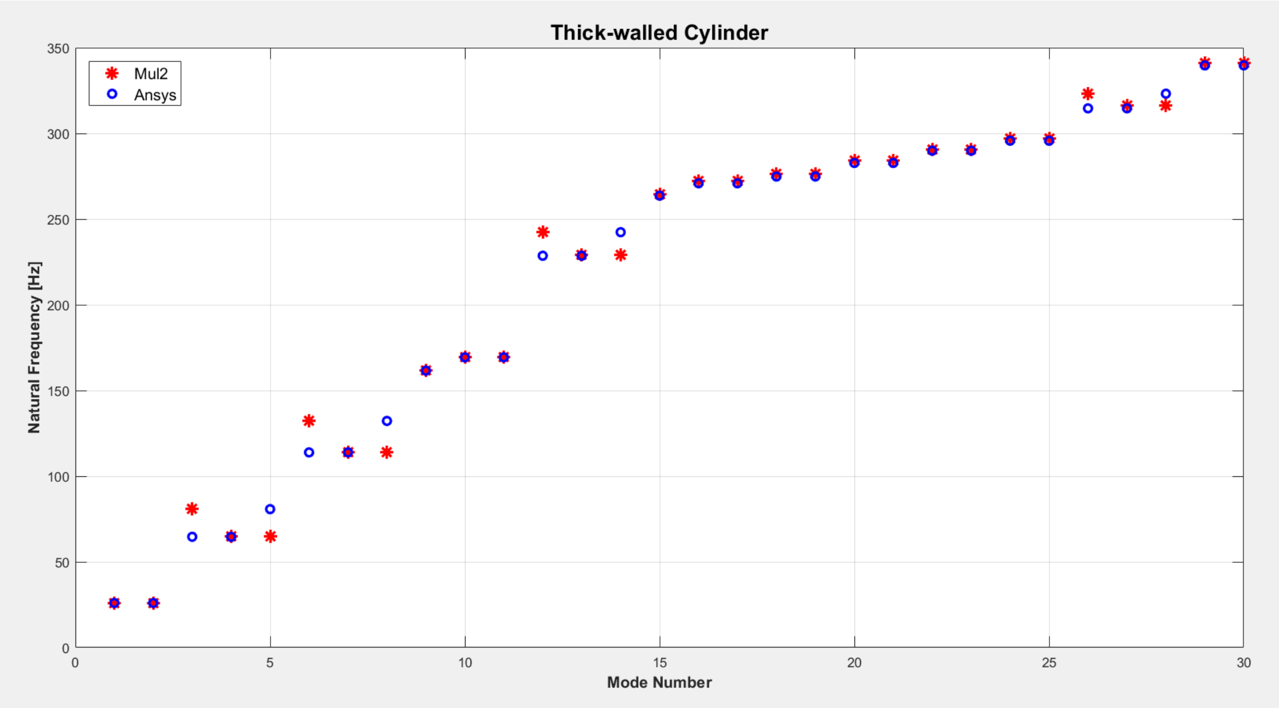

Figure 4.8 : Thick-walled Cylinder Natural Frequency Chart [Hz]

In this case we notice a perfect fit between the results of the two codes, which allows us to confirm the power of the Mul2 code and its reliability in finding exact results with significantly reduced computational effort compared to FEM analysis with 3D solid elements such as ANSYS.

The following images show the deformed configurations of some significant vibration modes: under each pair of graphs the type of mode and the associated number of half-waves are indicated (**Fig 4.9** - **Fig 4.10**).

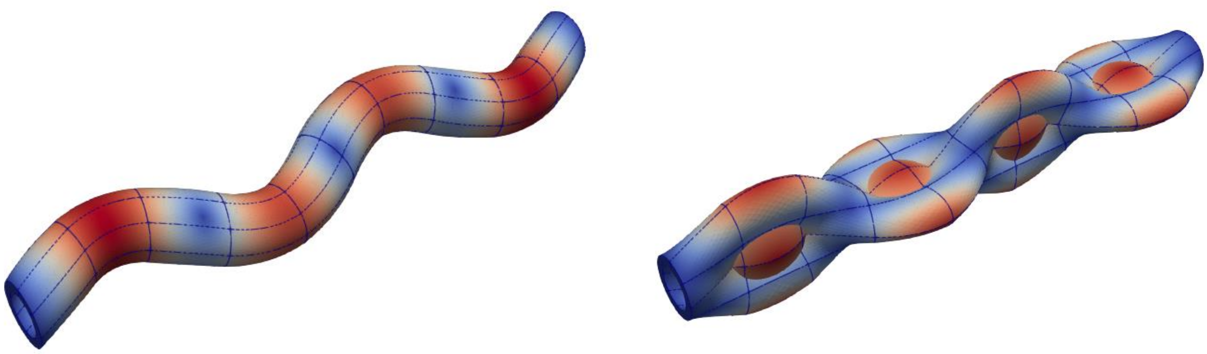

Figure 4.9 : Thick-walled Cylinder modes: Bending IV and Shell IV (Paraview)

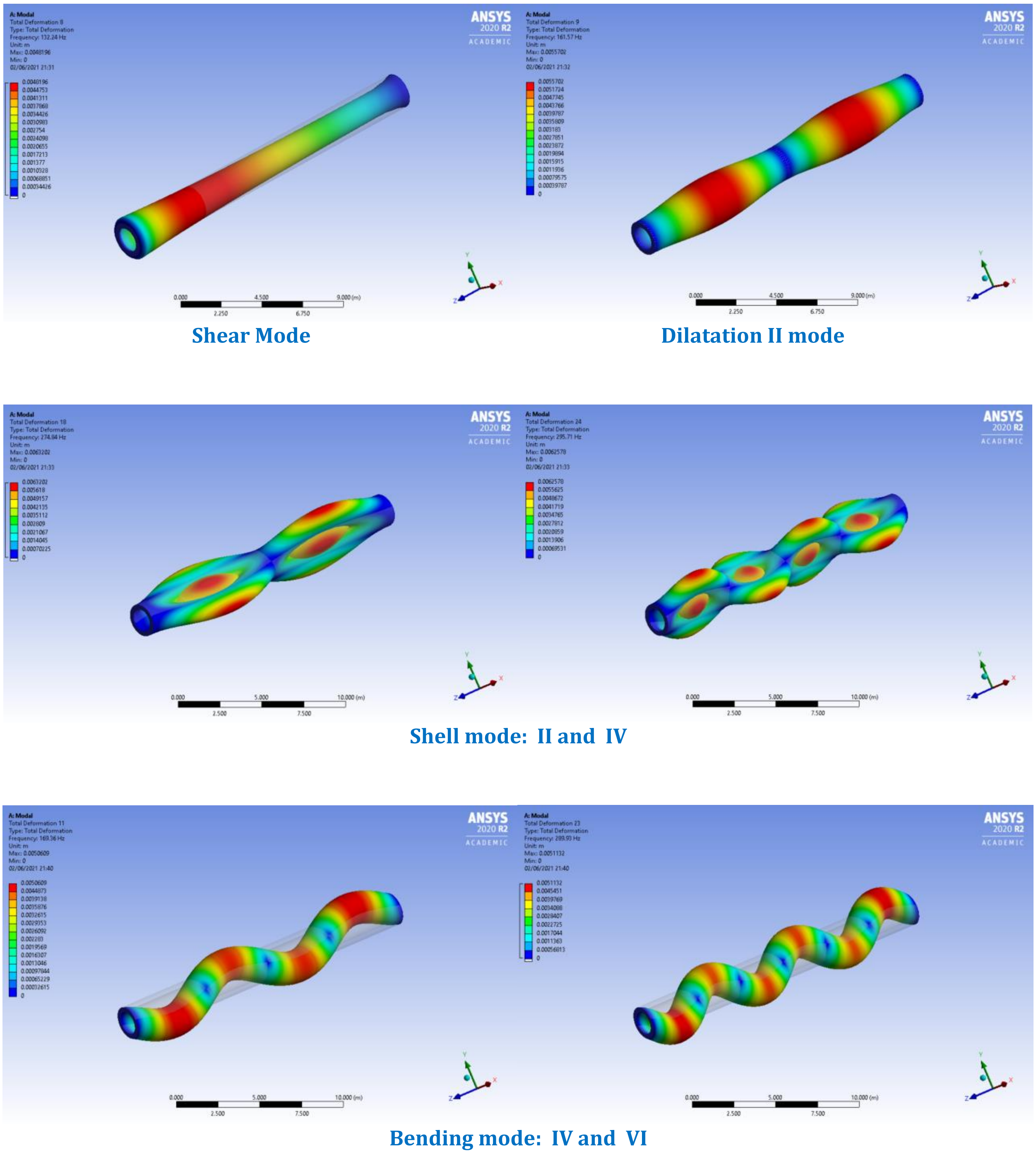

Figure 4.10 : Thick-walled Cylinder modes (ANSYS)

Thin disk with constant thickness

In this section we tried to prepare the geometry of some very important structures for the purpose of this thesis focused on the rotordynamic field: the first example of a rotating body that will be analyzed will in fact be the disk with constant thickness, already investigated by Entezari, Filippi and Carrera in their paper. **[13]**

The disk is forged in steel, an isotropic material with the following properties:

$$E = 210\,GPa, \qquad \nu = 0.3, \qquad \rho = 7800\,\frac{kg}{m^3}$$

The inner and outer radii and the thickness of the disk are assumed to be 0.1016, 0.2032 and $1.016 \cdot 10^{-3}\,m$ respectively, and the disk is considered as mounted on a rigid shaft, with its inner boundary fully fixed at the hub.
In contrast, the outside boundary is assumed to be traction free, as rotation and centrifugal effects will be introduced later in this work. This structure is meant to be analyzed using the 1D-CUF theory, where the capabilities of Lagrange-type elements will be evaluated.

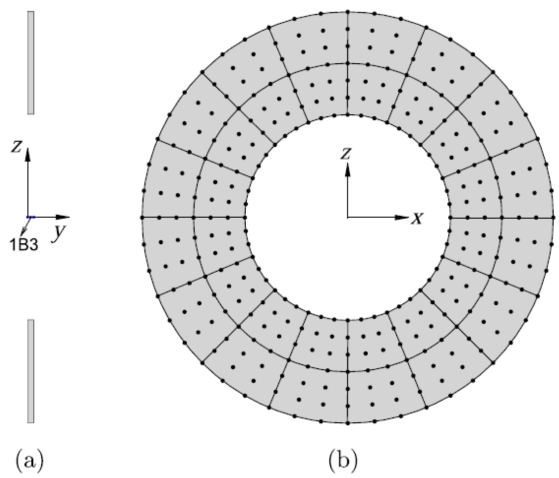

Figure 4.11 : Constant thickness disk mesh: (a) 1B3 along the axis; (b) 2 X 16 L16

As we can see in the **Fig. 4.11** image taken from the paper **[13]**, the mathematical model used for the simulation consists of a single 3-node beam element along the y-axis, and 2×16 cross-sectional mesh of L16 elements. In fact, from a convergence analysis performed previously, it emerged that this model already provides accurate results for the considered structure.

The same Matlab code was used to define the coordinates of the mesh points and to display them on a Cartesian plane: they were numbered to facilitate the construction of the connectivity matrix, formed, as we said, by 32 L16 elements that connect 336 points for each node of the structure (**Fig 4.12**):

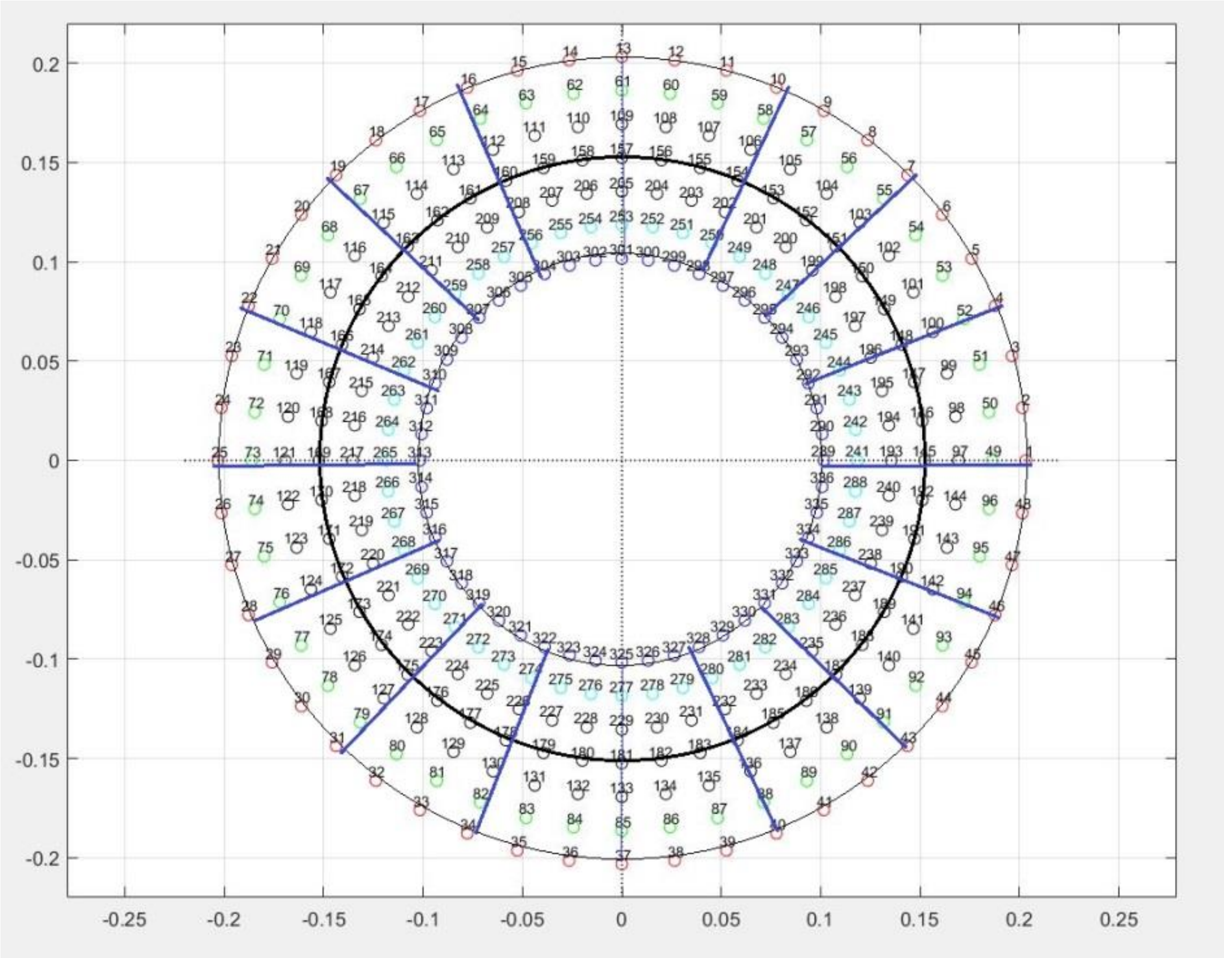

Figure 4.12 : MUL2 mesh for the constant thickness disk

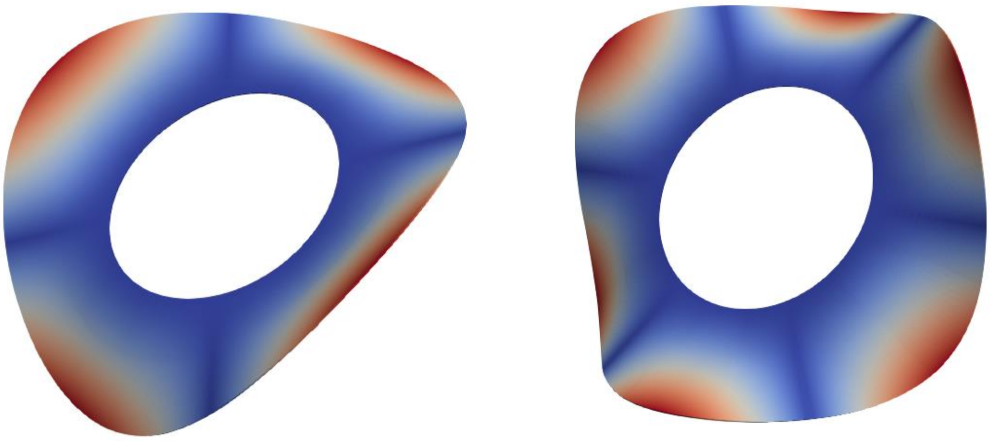

Figure 4.13 : Mode 4 (91.7 Hz) and Mode 7 (115.5 Hz) in Paraview

The results obtained from the simulation (**Fig. 4.13**) are completely identical to those present in the paper, so we now proceed to complicate the geometry of the structure, to make it more realistic.

Disk with variable thickness

It is rare for the rotors for real aeronautical applications to have a regular shape like the one analyzed above: often the rotors are machined from solid material and, for weight reduction needs (reduction of vibration and mass in flight to be transported, reduction of fuel consumption) they are usually tapered at their extremity, towards the external radius.
For this reason, the case of the variable thickness disk present in the same reference paper **[13]** was considered: although it presented a hyperbolic thickness profile, the disk was modeled through a 4 sections discretization, in order to be able to analyze it through the Mul2 code.
Among the various possible types of cross-section discretization, the one with 4×8 L16 elements has been here implemented, as shown in the **Fig. 4.14**.

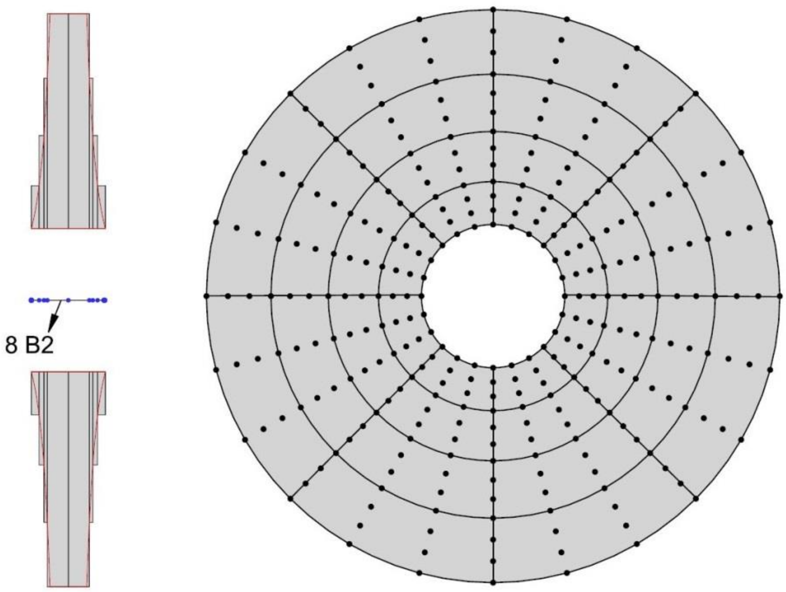

Figure 4.14 : 1D-CUF model of the variable thickness disk, $(1/2/3/4) \times 8$ L16

The results obtained from the first 20 natural frequencies show good adherence with the results of the paper and with the references of the bibliography (**Fig. 4.15**).

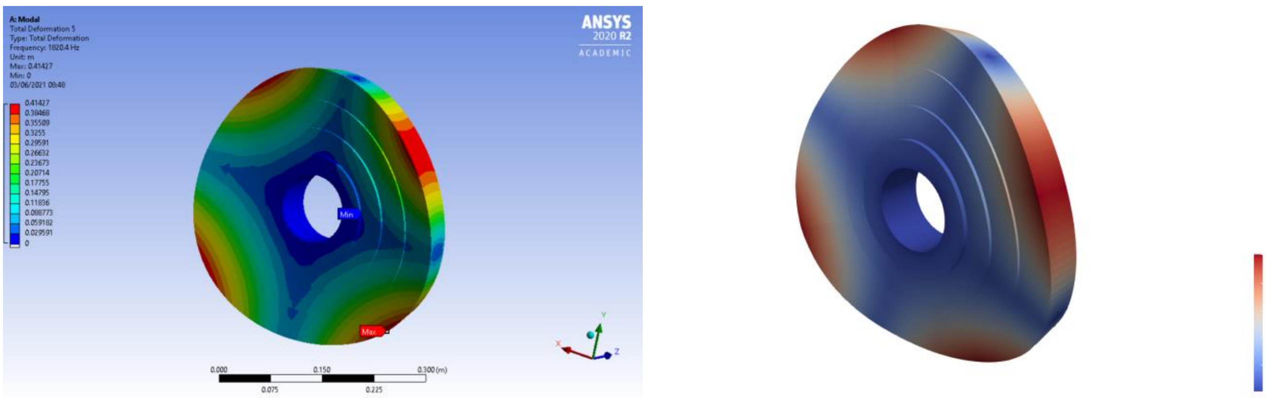

Figure 4.15 : Mode comparison between ANSYS and Paraview (Disk)

Complex rotor:

To extend our analysis to the most realistic case possible, the structure of the paper by Entezari, Kouchakzadeh, Carrera and Filippi **[14]** is now considered. The structure is an axisymmetric rotor, consisting of a main shaft on which a single turbine (with the same shape and size as the variable thickness disk considered previously) is keyed as well as two identical discs that simulate the compressor stages. It is assumed that the main shaft is hollow and flexible, and that it is fixed at both of its ends.
As in the previous case, the hyperbolic profile of the compressor and turbine discs was approximated by a discretization in 4 sections: we notice that the two compressor stages have a smaller radius than the turbine, as it usually happens in aircraft engines. The material of this complex rotor is assumed to be steel with:

$$E = 207\ GPa, \qquad \nu = 0.28, \qquad \rho = 7860\,\frac{kg}{m^3}, \qquad \alpha = 13 \cdot 10^{-6}\ °C^{-1}$$

The model has been created for both Mul2 and ANSYS software: in the first case was chosen a discretization model with 32 elements B2 along the y-axis and with 4×8 L16 elements for the cross section, schematized in the picture (**Fig. 4.16**).
On the other hand, the model for the commercial FEM software was first created in Solidworks environment and then imported in ANSYS Workbench for modal analysis.

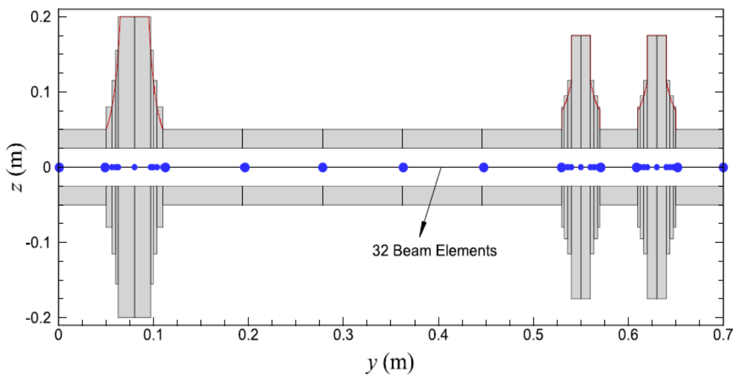

Figure 4.16 : Complex rotor Mesh schematization

The dimensioned blueprint of the rotor is shown in the following image (**Fig. 4.17**):

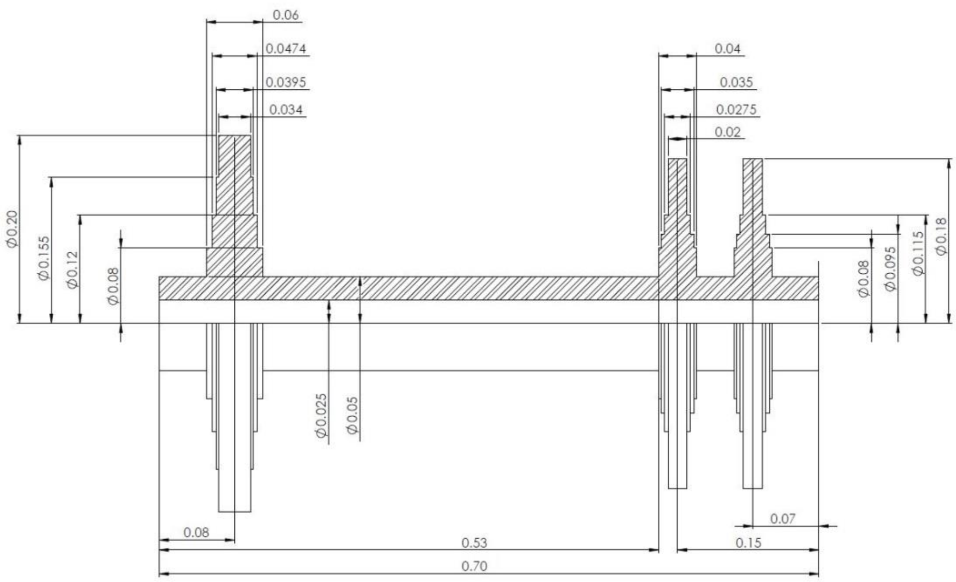

Figure 4.17 : Complex rotor Blueprint

Carrying out the analysis we obtained the frequencies reported in this summary table (**Tab 4.5**): comparisons with a converged 3D ANSYS solution revealed a good correspondence of the first 15 natural frequencies considered.

ω_n	*17820 DOF*	*Rel. Error [%]*	*17820 DOF*	*Rel. Error [%]*	*37293 DOF*	*Relative Error*
N°	*Present Model*	Present Model vs Paper **[8]**	*Paper [8] Mul2*	Paper **[8]** vs Ansys	*ANSYS*	Present Model vs Ansys
1	634.58	0.086	634.03	-0.95	640.12	-0.87
2	659.87	0.008	659.82	-3.34	682.6	-3.33
3	767.03	0.038	766.74	1.75	753.57	1.79
4	1012.12	0.051	1011.6	-2.19	1034.2	-2.14
5	1370.28	0.063	1369.42	1.03	1355.4	1.10
6	1607.85	0.073	1606.68	2.91	1561.2	2.99
7	1624.97	0.030	1624.49	3.74	1565.9	3.77
8	1679.54	0.056	1678.59	3.43	1623	3.48
9	1743.58	0.090	1742.01	2.21	1704.3	2.30
10	1766.58	0.057	1765.57	2.05	1730.1	2.11
11	1784.85	-0.104	1786.7	2.24	1747.5	2.14
12	1791.35	-0.017	1791.65	2.43	1749.2	2.41
13	1847.19	0.088	1845.57	2.72	1796.7	2.81
14	1857.51	0.016	1857.21	1.10	1837	1.12
15	2317.16	0.024	2316.6	0.59	2303.1	0.61

Table 4.5 : Natural frequencies obtained for the Complex rotor [Hz]

The deformed configuration of the 11^{th} natural mode is shown below as an example (**Fig. 4.18**), to show the effectiveness of the Mul2 code: the result obtained by ANSYS is presented on the left, while on the right we see the representation of the same mode calculated by Mul2 and post-processed through the Paraview 5.9.0 software.

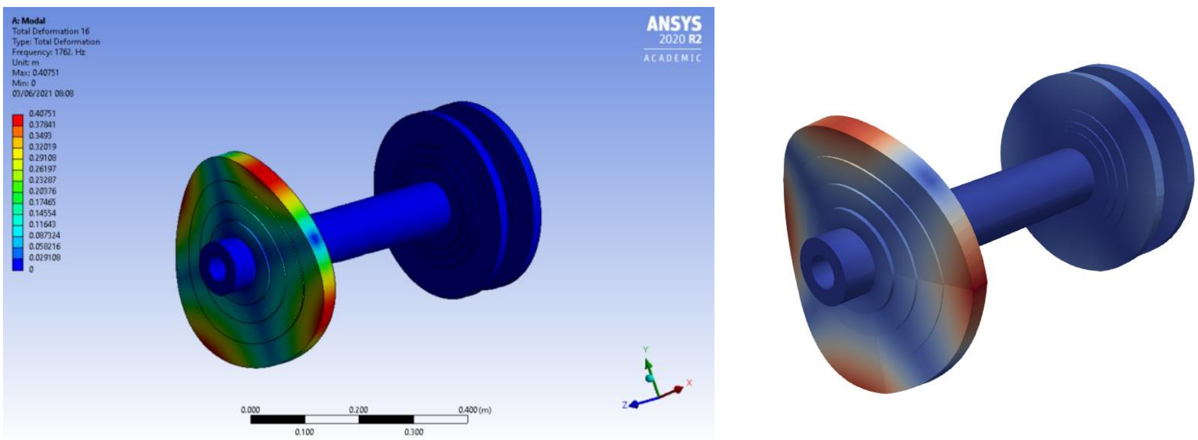

Figure 4.18 : Mode comparison between ANSYS and Paraview (Complex Rotor)

Bladed disk

The most realistic case analyzed will be that of the bladed disc shown in the figure: here we consider the same constant thickness disc of the previous, but we added 16 identical blades, each modeled as a thin rectangular section beam.

In this case we choose Inconel as the material, with the following mechanical properties:

$$E = 174\,GPa, \qquad \nu = 0.3, \qquad \rho = 8200\,\frac{kg}{m^3}$$

Each blade has been modelled using 4 Q9 Lagrange elements, and extends for a further 20 cm beyond the external radius of the disc, reaching a total diameter of 80 cm. All the blades are perfectly identical,; they have a width of 1.3 cm and their thickness is equal to that of the disc, specifically 6 cm (**Fig. 4.19**).

The first 50 natural frequencies were analyzed, in order to investigate various mode-types of the blades.

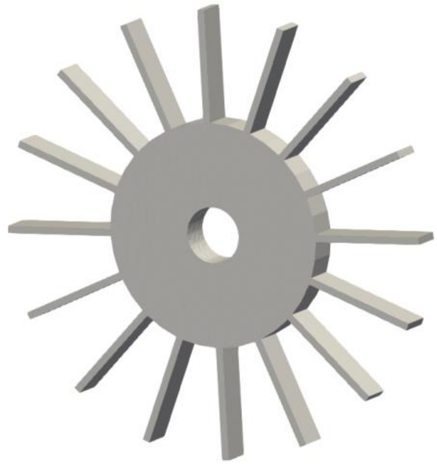

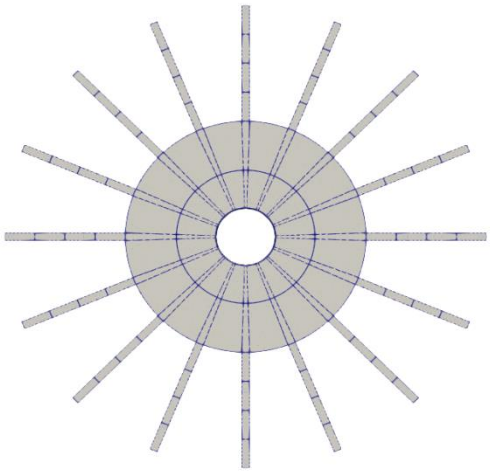

Figure 4.19 : Bladed Disk Model

As we can expect, the blades have obviously the lowest local stiffness, so the dynamics of this rotor will be dominated by their vibrations: the central hub will be treated almost as a rigid body, which is free from any deformation.

	MUL2		ANSYS	Rel. Error [%]
NODES	6336		24511	
DOFs	19008		73533	
Frequency N°				
1	240.87		233.23	3.27
2	243.82	m=2	235.68	3.46
3	243.82	"	235.69	3.45
4	243.49	m=8	235.76	3.28
5	243.74	m=3	235.78	3.38
6	243.74	"	235.81	3.36
7	243.66	m=4	235.82	3.32
8	243.66	"	235.9	3.29
9	243.53	m=6	235.91	3.23
10	243.53	"	235.91	3.23
11	243.50	m=7	235.91	3.22
12	243.50	"	235.94	3.20

13	243.61	m=1	235.98	3.23
14	243.61	"	236.01	3.22
15	243.59	m=5	236.01	3.21
16	243.59	"	236.07	3.19
17	639.44	Rotor Bending (m=1)	625.06	2.30
18	639.44	"	625.12	2.29
19	688.05	Umbrella Mode (m=0)	672.44	2.32
20	687.38	In phase Bending (m=2)	672.91	2.15
21	687.38	"	673.01	2.13
22	815.03	In phase Bending (m=3)	791.06	3.03
23	815.03	"	791.07	3.03
24	874.80	In phase Bending (m=4)	843.92	3.66
25	874.80	"	843.93	3.66
26	929.01	Alternating Bending (m=8)	868.44	6.97
27	918.84	In phase Bending (m=6)	868.45	5.80
28	918.84	"	880.94	4.30
29	903.55	In phase Bending (m=5)	881.2	2.54
30	903.55	"	887.32	1.83
31	926.61	In phase Bending (m=7)	887.32	4.43
32	926.61	"	889.23	4.20
33	1303.43	2° Harmonic (m=0)	1259.7	3.47
34	1528.34	Torsion (m=2)	1436	6.43
35	1528.34	"	1436	6.43
36	1530.02	Torsion (m=1)	1448.9	5.60
37	1530.02	"	1449.6	5.55
38	1531.50	Torsion (m=3)	1450.5	5.58
39	1534.43	Torsion (m=0)	1450.5	5.79
40	1534.15	Torsion (m=8)	1450.7	5.75
41	1533.96	Torsion (m=6)	1451	5.72
42	1533.96	"	1451.1	5.71
43	1534.10	Torsion (m=7)	1451.1	5.72
44	1534.10	"	1451.1	5.72
45	1532.96	Torsion (m=4)	1451.8	5.59
46	1532.96	"	1451.8	5.59
47	1533.63	Torsion (m=5)	1451.8	5.64
48	1533.63	"	1451.8	5.64
49	1533.01	2° Harmonic (m=1)	1483.9	3.31
50	1533.01	"	1484.3	3.28

Table 4.6 : Bladed Disk results in terms of natural frequencies [Hz]

The results shown in the previous table (**Tab 4.6**) show a good correspondence between the MUL2 model, characterized by a lower number of degrees of freedom, and the ANSYS model. The relative error calculated on the first 50 natural frequencies always oscillates between 3% and 6%, perfectly acceptable if we consider the computational cost reduced by almost 75% (19.008 vs 73.533 DOFS): the tradeoff is worth the candle (**Fig. 4.20**).

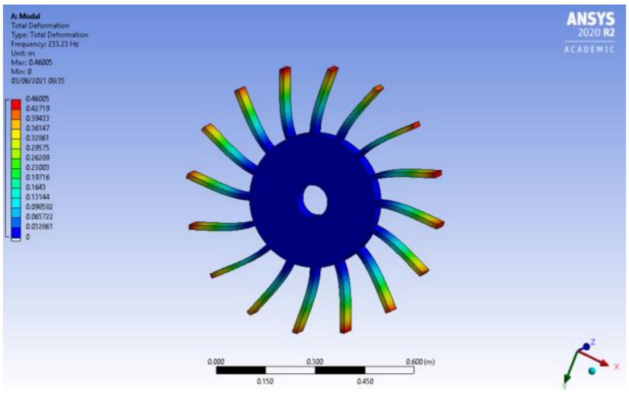

I Bending mode (all blades in sync)

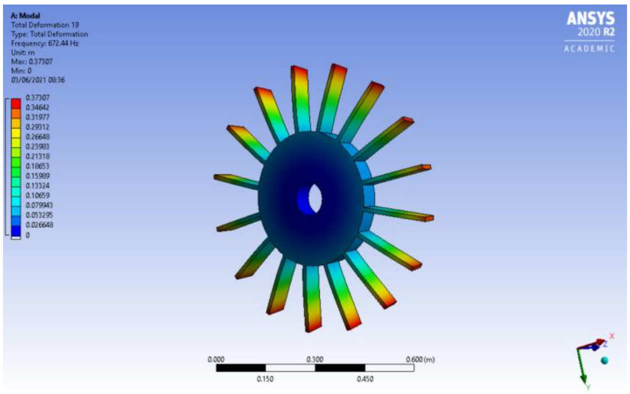

Umbrella Mode

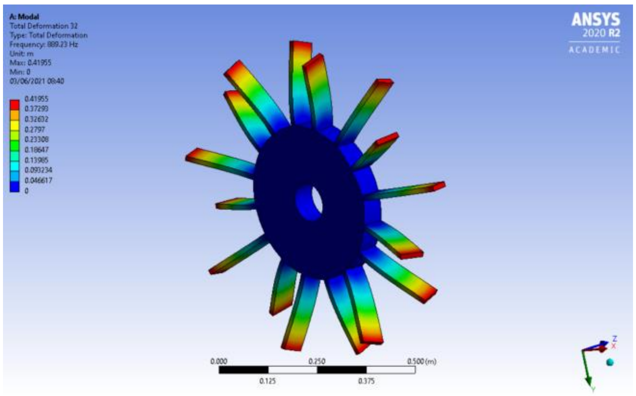

Out of plane B mode (Alternating bending)

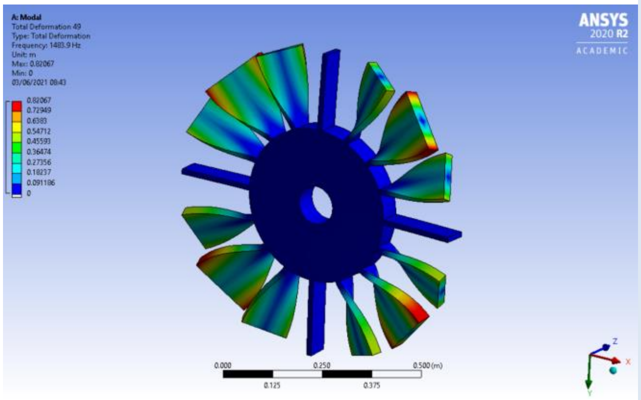

Torsional Mode (m=2)

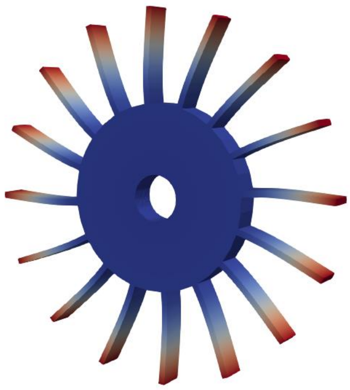

I Bending mode

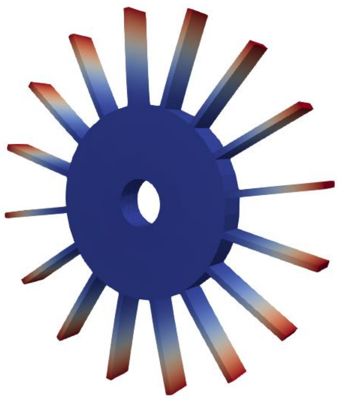

Umbrella Mode (m=2)

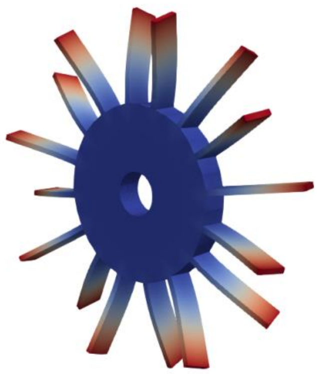

Alternating bending

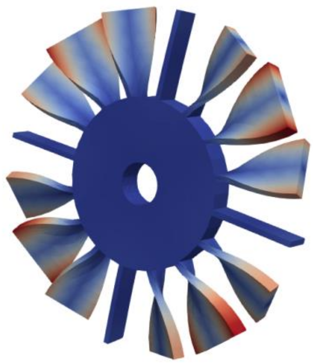

Torsional Mode (m=2)

Figure 4.20 : Bladed Disk modes (ANSYS & Paraview)

Chapter V
Campbell Diagrams

In this chapter the effects of the rotordynamics are introduced through the possibility of varying the rotation speed in a range which is pre-established by the user. A MUL2 code has been developed by the university department to be able to perform linearized (165) and non-linear (108) analyses solving the equations of the dynamical system previously introduced.

The results obtained through the non-linear and linearized analysis are presented superimposed on the same Campbell diagram, with the aim of observing the differences between them, when these are applied to the cases and structural models described above.

A Campbell diagram plot represents a system's response spectrum as a function of its oscillation regime. It is named for Wilfred Campbell, who introduced the concept, but it is also known as interference diagram.

In rotordynamical systems, the eigen-frequencies often depend on the rotation rates due to the centrifugal force, the induced gyroscopic effects or variable hydrodynamic conditions in fluid bearings if these are investigated. It might represent the following cases:

1. Analytically computed values of eigen-frequencies (natural frequencies) as a function of the shaft's rotation speed. Such chart takes also the name of "whirl speed map"and can be very helpful in turbine design. For example, in the numerically calculated Campbell diagram example shown in the **Fig. 5.1**, we can identify a critical speed whenever the rotation speed diagonal intercepts a curve.

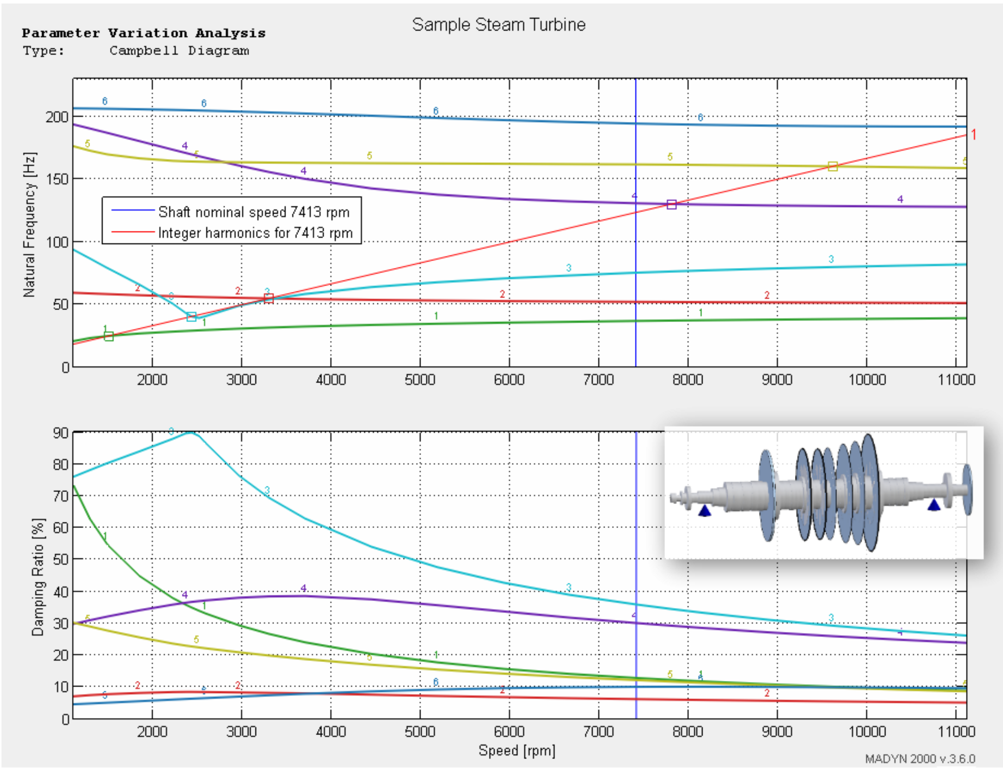

Figure 5.1 : Realistic example of a Campbell diagram [15]

Further analysis of this graph from reference **[15]** highlights that the first three critical speed happen at lower speed range and are very well damped. However, for this rotor, another critical speed at mode 4 is observed at 7810 rpm (130 Hz) in dangerous proximity of nominal shaft speed, but it has 30% damping, which is enough to ignore it by a good confidence margin regarding the operational safety of the machine.

2. The second type of Campbell Diagram plot the experimentally measured vibration response spectrum as a function of the shaft's rotation speed (waterfall plot), the peak locations for each slice usually corresponding to the eigen-frequencies (**Fig. 5.2**).

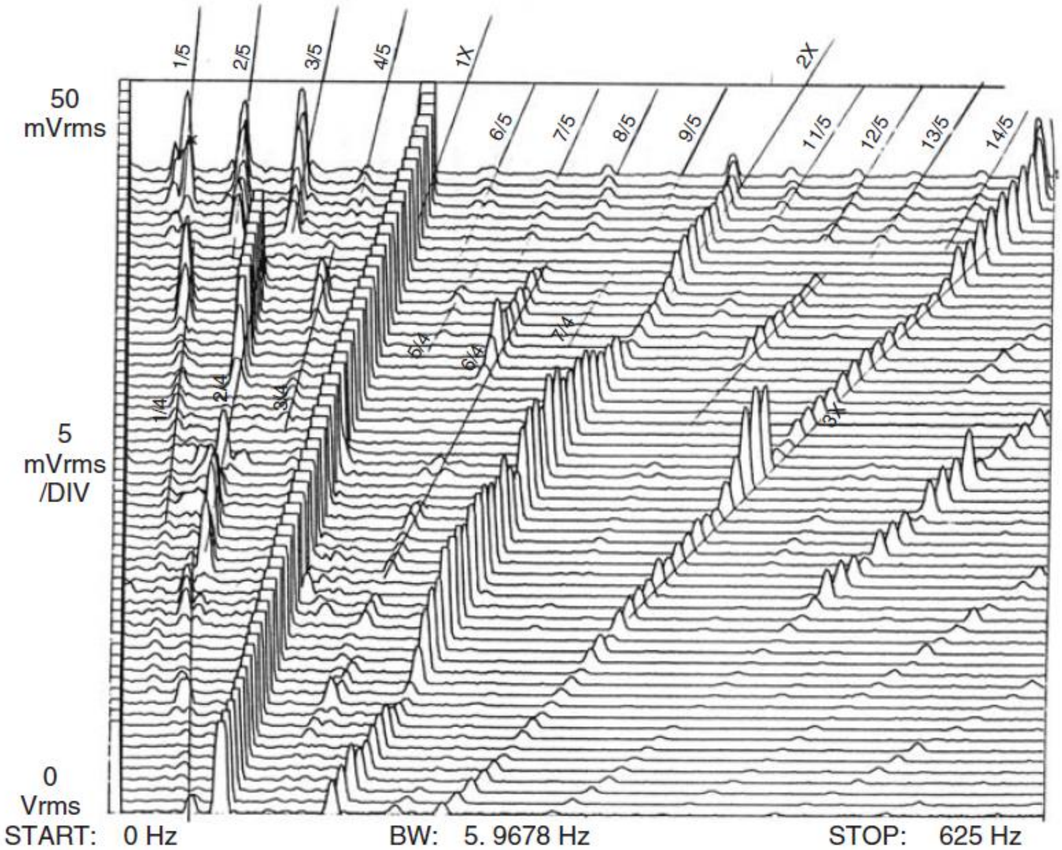

Figure 5.2 : Waterfall plot: influence of the bilinear spring effect on vibrations [4]

In the Campbell diagrams shown below, the natural frequencies calculated by the non-linear analysis (108) will always be identified by a purple square, while the results of the linearized analysis (165) are represented by a solid blue line.

Constant Thickness Disk

As a first analysis of this chapter, the results are presented for the case of the constant thickness disk, the model of which was described above (see page 55).

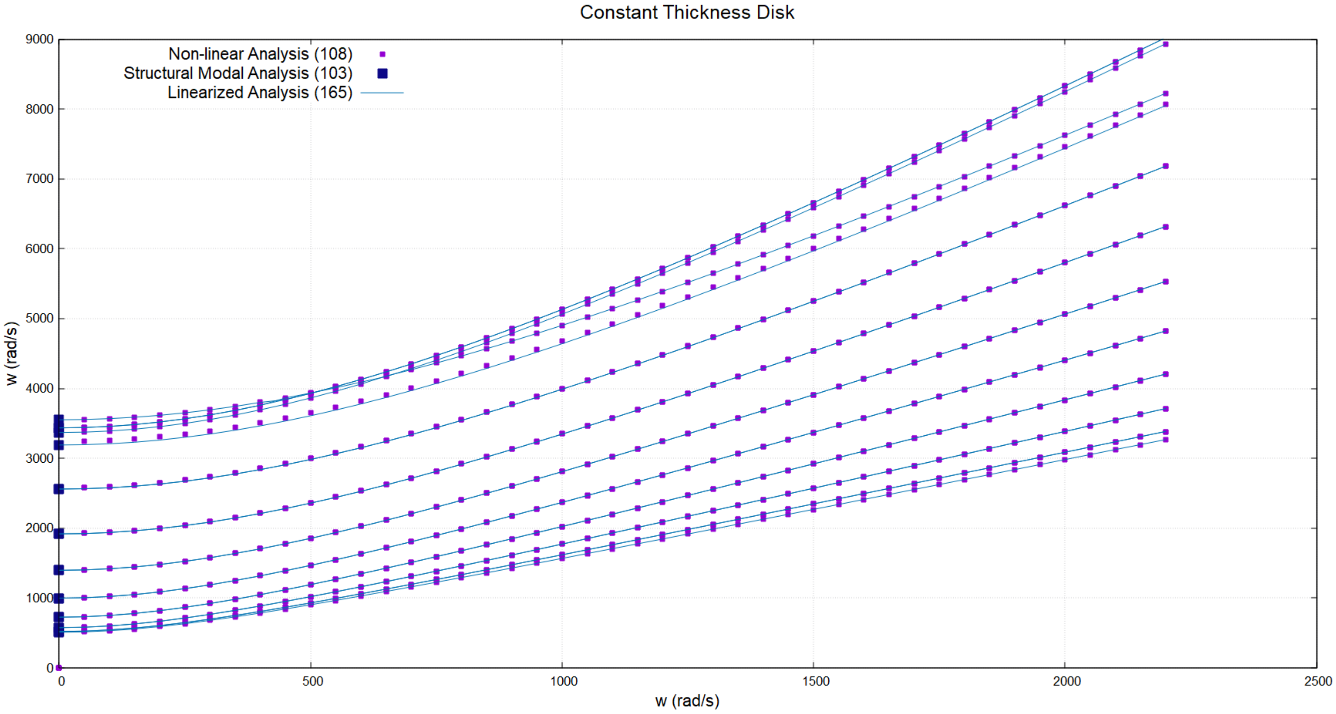

Figure 5.3 : Campbell Diagram for the constant thickness Disk

The rotation speed has been made to vary between 0 and 2200 radians per second (**Fig. 5.3**): this is already a considerable speed, if we convert to Hz or rpm:

$$2\pi\frac{rad}{s} = \frac{360°}{s} = 1\ Hz = \frac{rpm}{60} \quad\rightarrow\quad 2200\frac{rad}{s} \approx 350\ Hz \approx\ 21000\ rpm$$

However, we can see that both the Nonlinear (108) and linearized (165) analysis behave well, as both start from the correct values of the natural frequencies calculated at zero speed with the Structural Modal Analysis (103).
It is possible to visualize the phenomenon of stress stiffening caused by the deformation generated by centrifugal forces, with the consequent increase in the value of natural frequencies with the increasing rotation speed. The natural modes families are well delineated and tend to diverge continuing to the right.

More important, however, is to note that the results of the 2 types of analysis are perfectly consistent with each other: this was an expected event, as the shape of the disc has a sufficient thickness not to deform excessively in a geometrically non-linear field, which is why the linearized theory continues to follow the trend of the graph in a proper way even at very high speeds.

Variable Thickness Disk

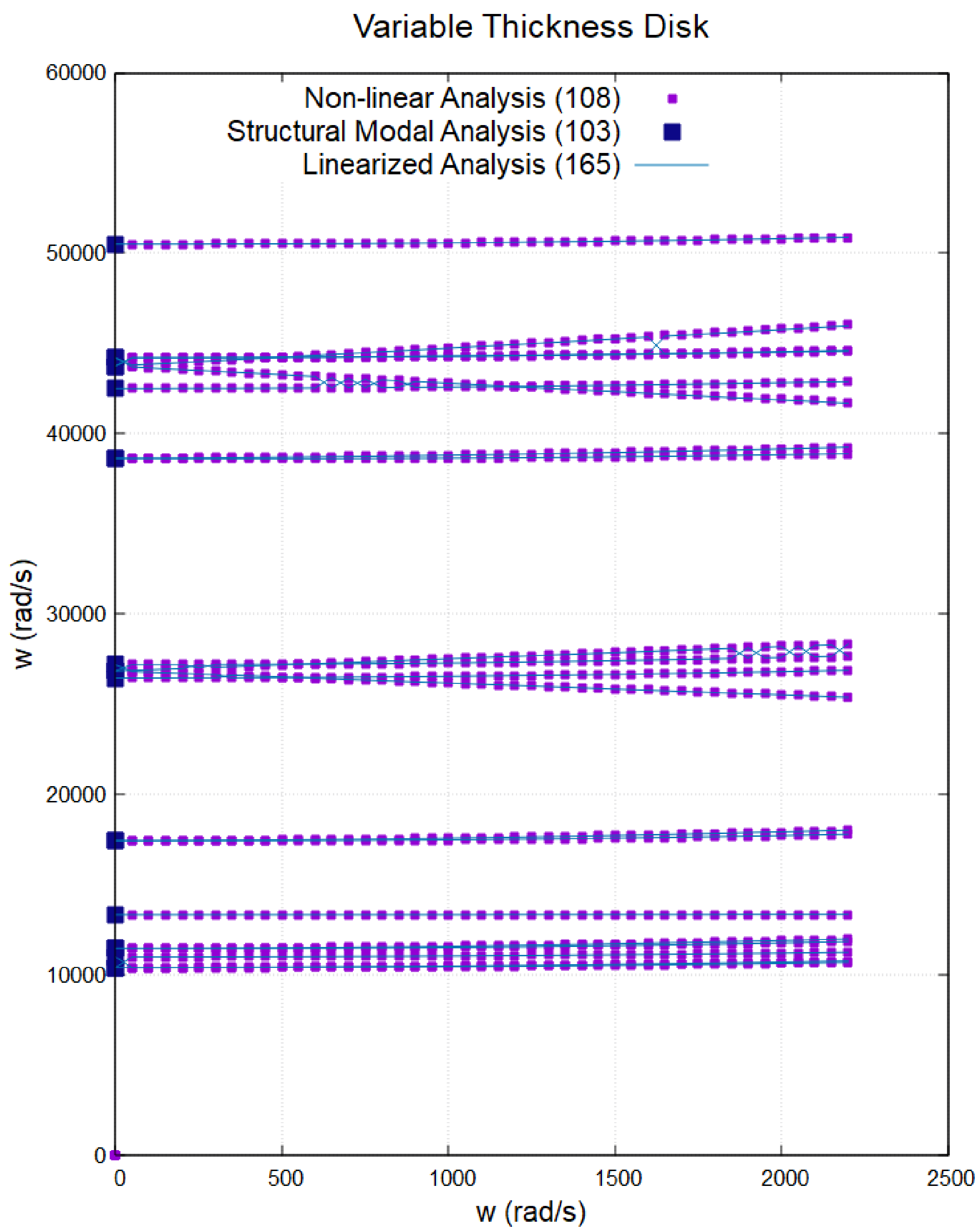

Figure 5.4 : Campbell Diagram for the Variable thickness Disk

This rotordynamic analysis doesn't show much difference: the effects of the rotational speed does not affect the natural frequencies very much: if we observe the shape of this disk (**Fig. 4.15**), which tries to resemble an axial turbine stage, we realize that it is much more rigid than the previous o (**Fig. 4.13**), since it has a higher thickness/diameter ratio. This fact is also confirmed by the much higher value assumed by the eigen-frequencies themselves, calculted with the rotor stopped (speed equal to zero). Nevertheless, we are witnessing an intersection between the families of natural-modes (**Fig. 5.4**), which occurs at approximately 1000 rad/s = 9550 rpm.

Thin Walled Cylinder

The focus of this thesis concerns the analysis of the differences that emerge between the two theories (linearized and non-linear) when these are applied to the same structure. In order to allow for greater differences, we will now analyze a whole series of thin-walled structures.

The cross-section is the same as that of the cylinder already analyzed on page 48 (**Fig. 5.5**), taken from reference **[9]**, just as the material is still an isotropic aluminum alloy with the following mechanical characteristics:

$$E = 75\,GPa, \qquad \nu = 0.33, \qquad \rho = 2700\,\frac{Kg}{m^3}$$

The thickness, t, is equal to $0.02\,m$, while the length of the cylinder, L, has changed and is now equal to $2\,m$. The structure has been modelled so that it can rotate on itself, but the points at both ends cannot exit from their plane. In a certain way this condition resembles that of a ball bearings, in which the only degree of freedom allowed is the of rotation around its own y −axis.

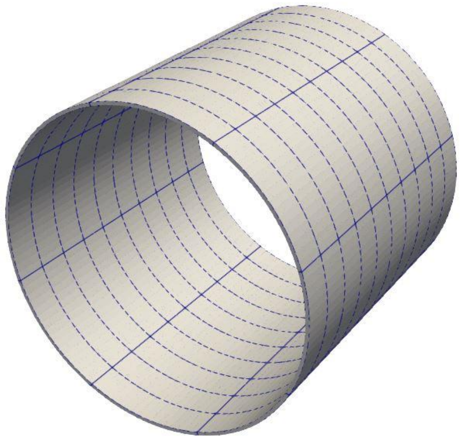

Figure 5.5 : Thin walled Cylinder (Rotordynamic analysis)

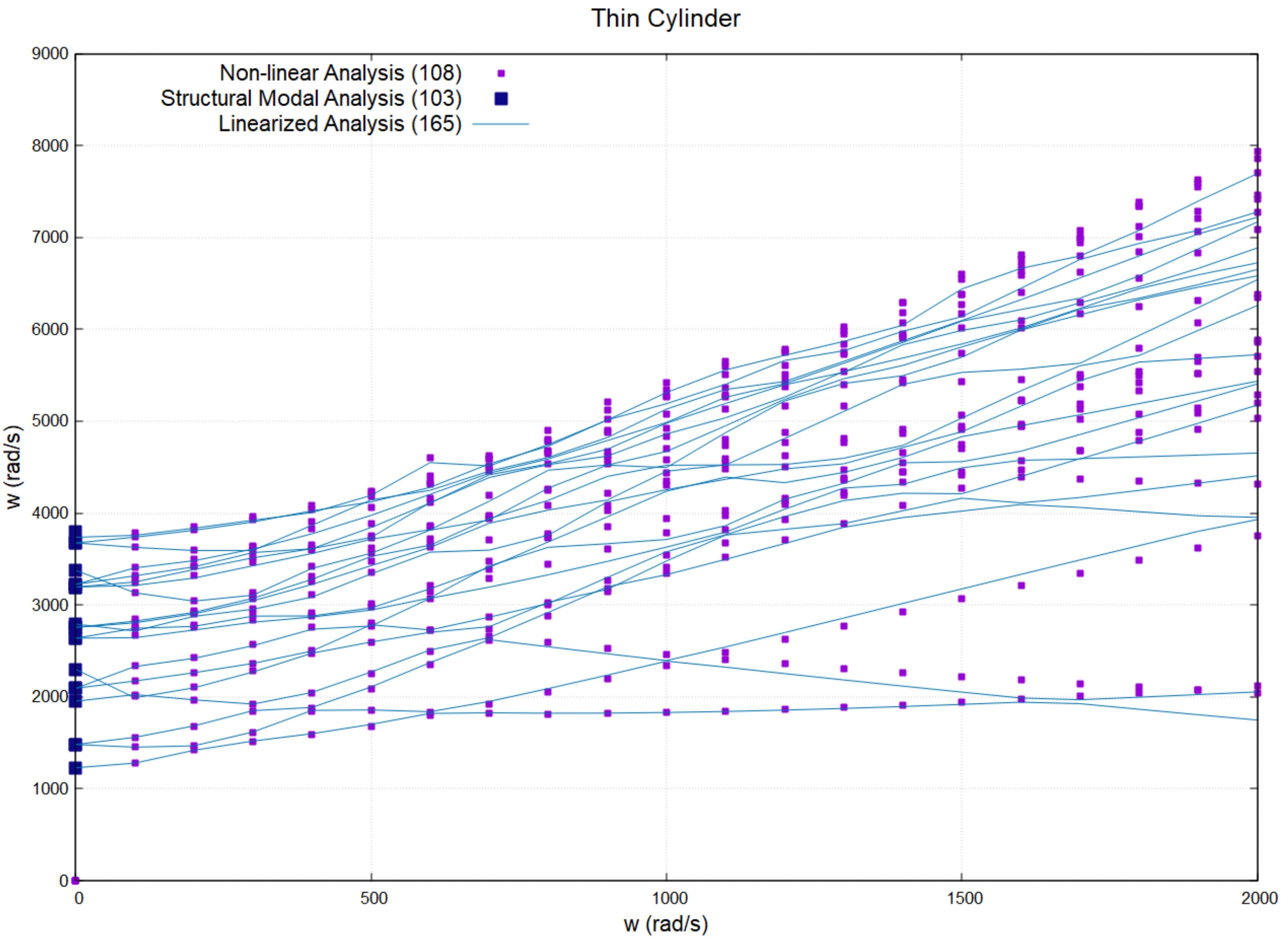

Figure 5.6 : Campbell Diagram for the Thin walled Cylinder

Thick Walled Cylinder

In order to further investigate these aspects, a dual structure is now investigated, which consists of a cylinder of the same length and diameter as the previous one, but with its thickness, t, increased to 0.3 m (**Fig. 5.7**).

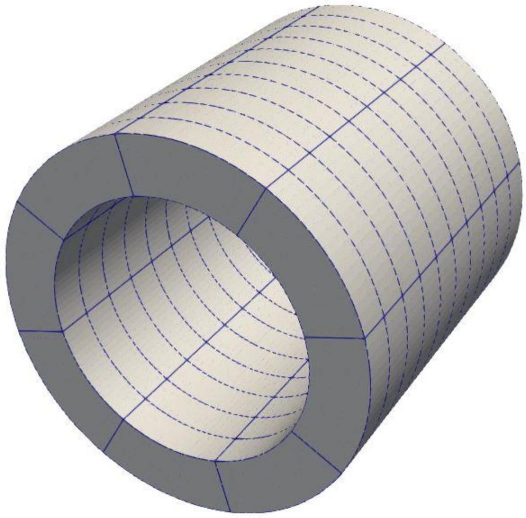

Figure 5.7 : Thick walled Cylinder (Rotordynamic analysis)

In the previous **Fig. 5.6** it is possible to appreciate a much richer and more varied structural dynamics: the solid blue lines of the linearized analysis help the reader to understand the real trend of the natural frequencies families, their intersections and the mode veering zones.

A similar good results can also be seen in the following **Fig. 5.8.**

The greater thickness presupposes a greater quantity of resisting material, which contributes to a greater rigidity of the structure and to higher values for the natural frequencies.

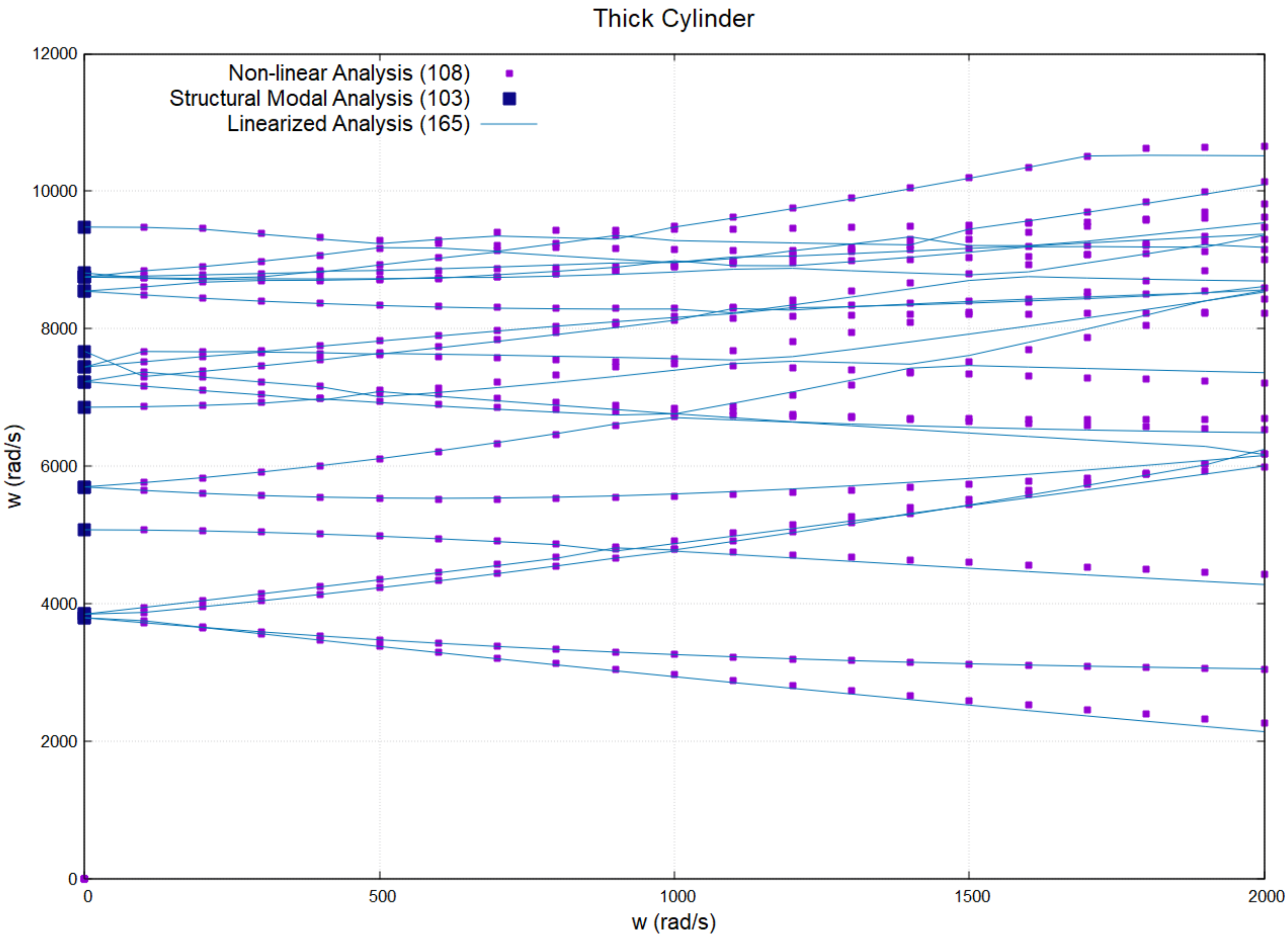

Figure 5.8 : Campbell Diagram for the Thick walled Cylinder

Shallow and deep Shells

A thorough investigation has been performed about the natural vibration of shell structures: in particular, the two configurations presented in the figure **Fig. 5.9** were tested.

The first one is a shallow Shell, obtained from an arc of a circle with a radius of 1 m and thickness $t = 0.02\ m$.

The second is a deep Shell, obtained from a an arc of a circle with a slightly smaller radius of 0.6 m, and a reduced thickness of $t = 0.01\ m$.

Both shell structures were modeled using 10 B4 1D elements along their $1m$ y-axis extension: however, the shallow Shell has only 6 L16 Lagrange elements in its circumferential direction, while the greatest curvature of the deep shell required a more refined discretization, with 10 L16 Lagrange elements.

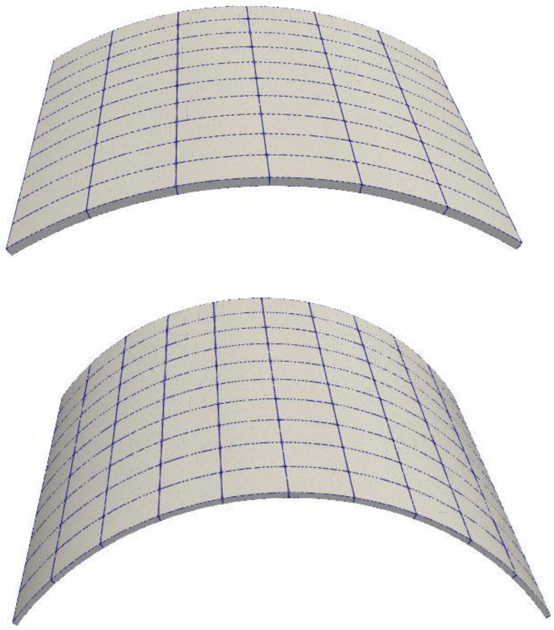

Figura 5.9 : Shallow and Deep Shells

Boundary conditions were applied to both configurations that allowed them to rotate around their own longitudinal y-axis, passing through the origin of the reference system.

As we can observe from the following images (**Fig. 5.10** and **Fig. 5.11**), in this case the combination of boundary conditions and very thin structure determined strong differences in the results obtained from the two types of analyses: namely 108 and 165. Both start from the correct values for the zero rotation speed ($\omega = 0$), also calculated through the structural modal analysis 103, but soon the calculated values tend to diverge, moving further and further away.

It is important to underline that in this case the rotation range was limited between 0 and 400 radians per second: this proved necessary for the correct functioning of the linearized analysis, which in other processing at higher speeds entered into crisis and began to return null values, which compromised the effectiveness of the visualization.

This erroneous behavior could be caused by the lack of stiffness of the structure: when it is subjected to excessively high centrifugal loads, it can reach a deformed configuration so different and far from the undeformed one, that the linearization is no longer valid, as it leads to neglect some non-linear terms which actually have an order of magnitude very similar to the linear ones.

Nevertheless, before presenting these problems, the linearized theory copies well the trends of the non-linear theory, presenting the same intersections and the growth of frequencies within the same family, at least at low speeds.

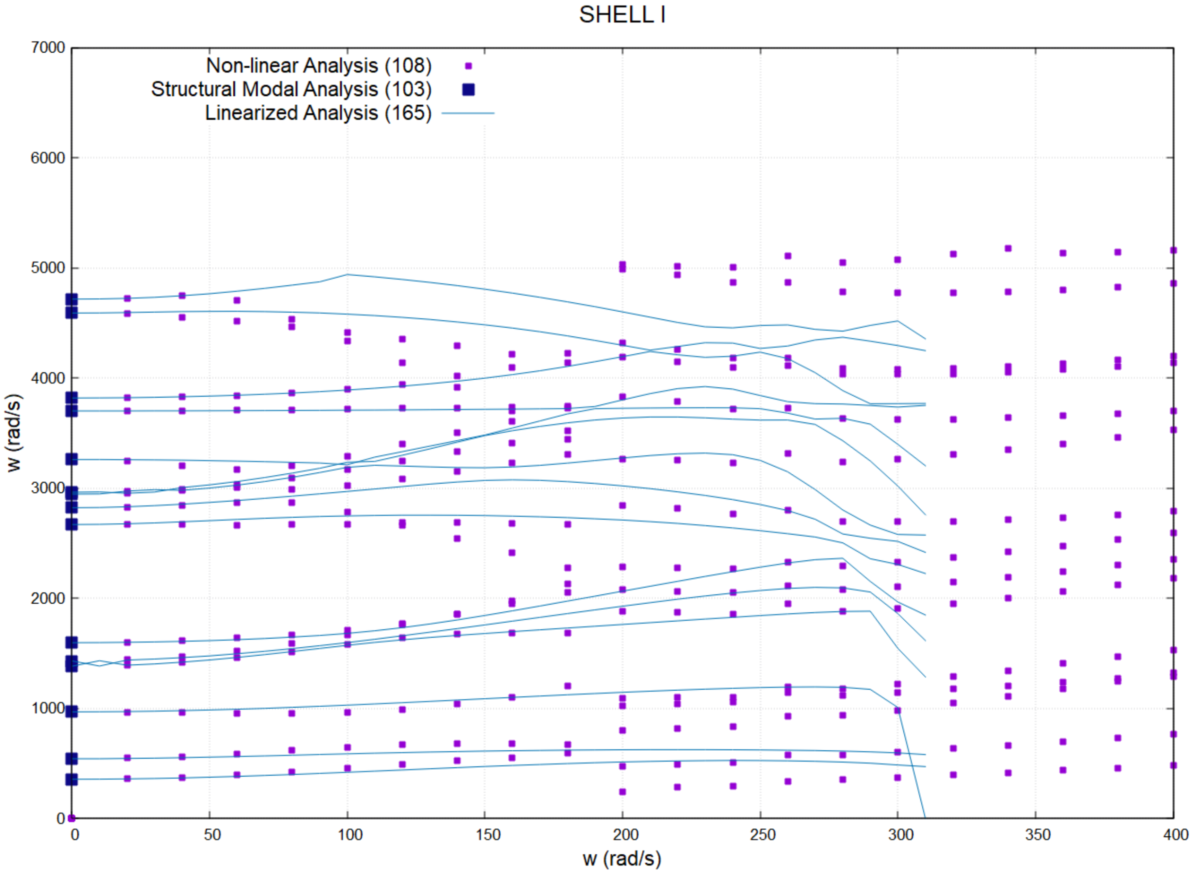

Figure 5.10 : Campbell Diagram for the Shallow Shell

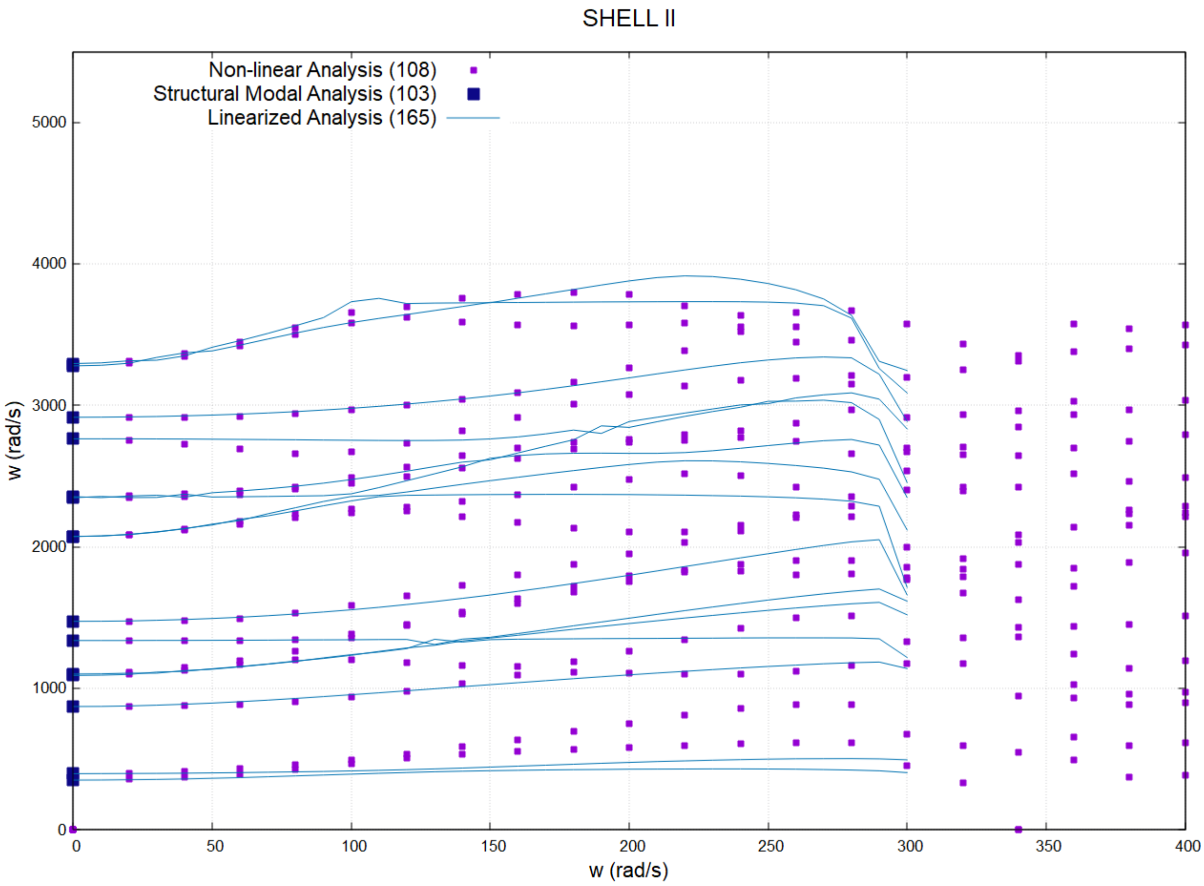

Figure 5.11 : Campbell Diagram for the Deep Shell

Complex Rotor

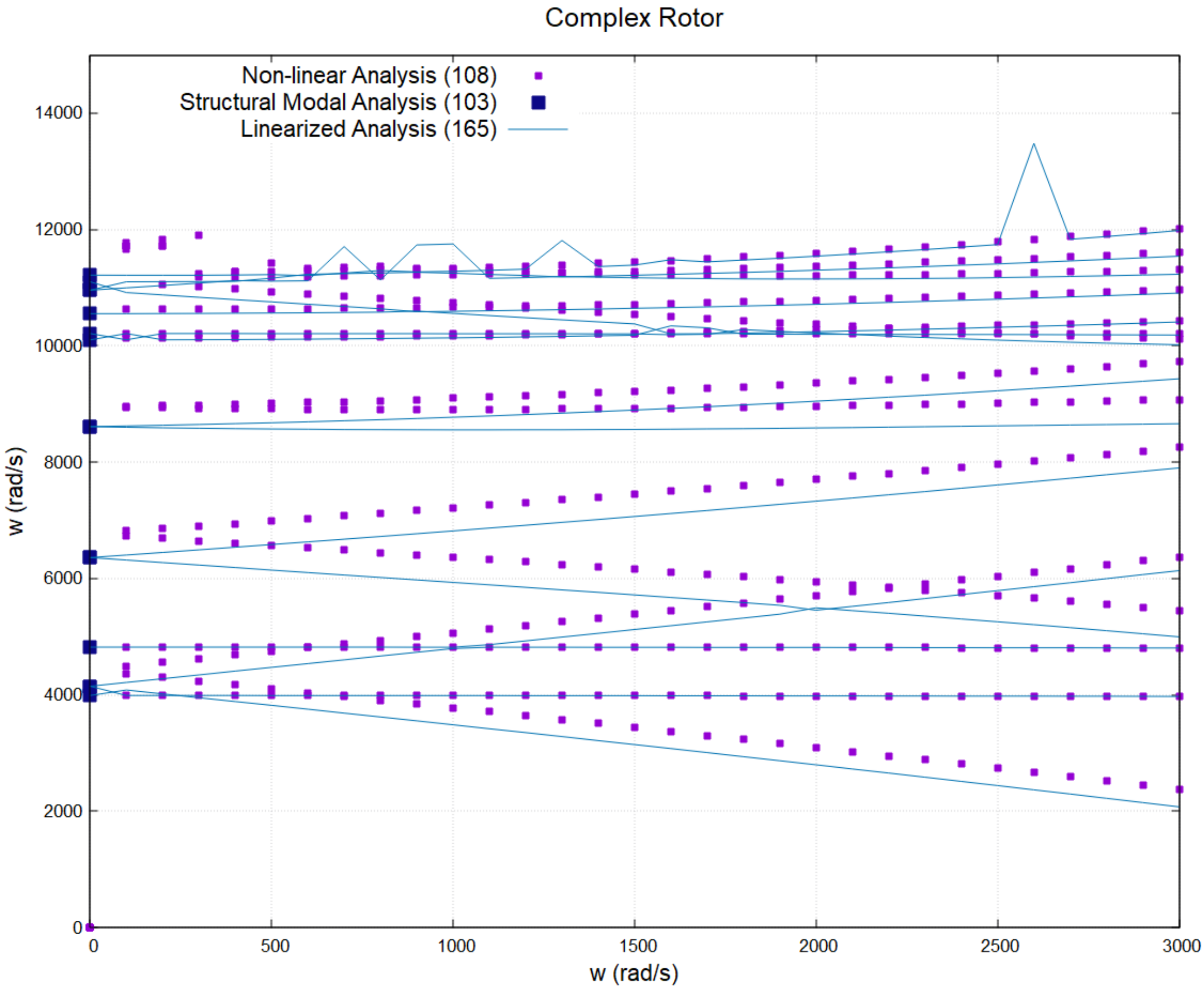

Figure 5.12 : Campbell Diagram for the Complex Rotor

In this section will be presented the results obtained for the complex rotor described previously in chapter 4, and taken from the reference **[13]**.

In general, the structure is sufficiently rigid and in fact the two analyses do not differ too much from each other: on the other hand, we perceive here the greater richness of dynamic phenomena due to the interaction of the vibrating modes of the shaft, of the turbine disk and two disks simulating two stages of an axial compressor.

Overall, the linearized analysis is able to follow the trend of the natural frequencies families as calculated by the non-linear analysis (**Fig. 5.12**), even if with a slight gap between the results: nevertheless, for the purposes of the Mul2 program, this small difference can be acceptable, if we consider the large time difference necessary to carry out the two analyses, which certainly goes to the advantage of the linearized analysis 165. Especially in the preliminary design phases, when the geometry of the entire rotor and all its components is not yet fully defined, it is absolutely convenient to have a rapid and sufficiently reliable tool for the calculation of the first natural frequencies, in order to direct the future changes.

Thin Ring

Continuing the analysis of thin and particularly flexible structures, the Campbell diagram obtained for the case of a thin ring is here presented.

This model was obtained starting from the same cross section already used for the case of the thin-walled cylinder on page 67, but the length along the longitudinal axis has been reduced to just 0.1 m, as shown in the **Fig. 5.13.**

The results shown in the graph below (**Fig. 5.14**) are not particularly good, as the difficulty of linearized theory in describing these very flexible structures well at high speeds and with large deformations reoccurs.

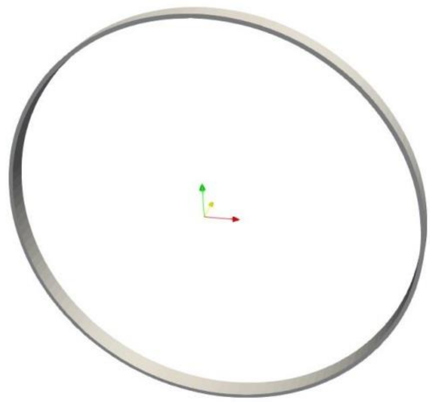

Figure 5.13 : Thin Ring Model

Nevertheless, it can be seen how at least the linearized theory is able to predict the increase of the natural frequencies values at higher speeds, especially for the modes that already start from higher values.

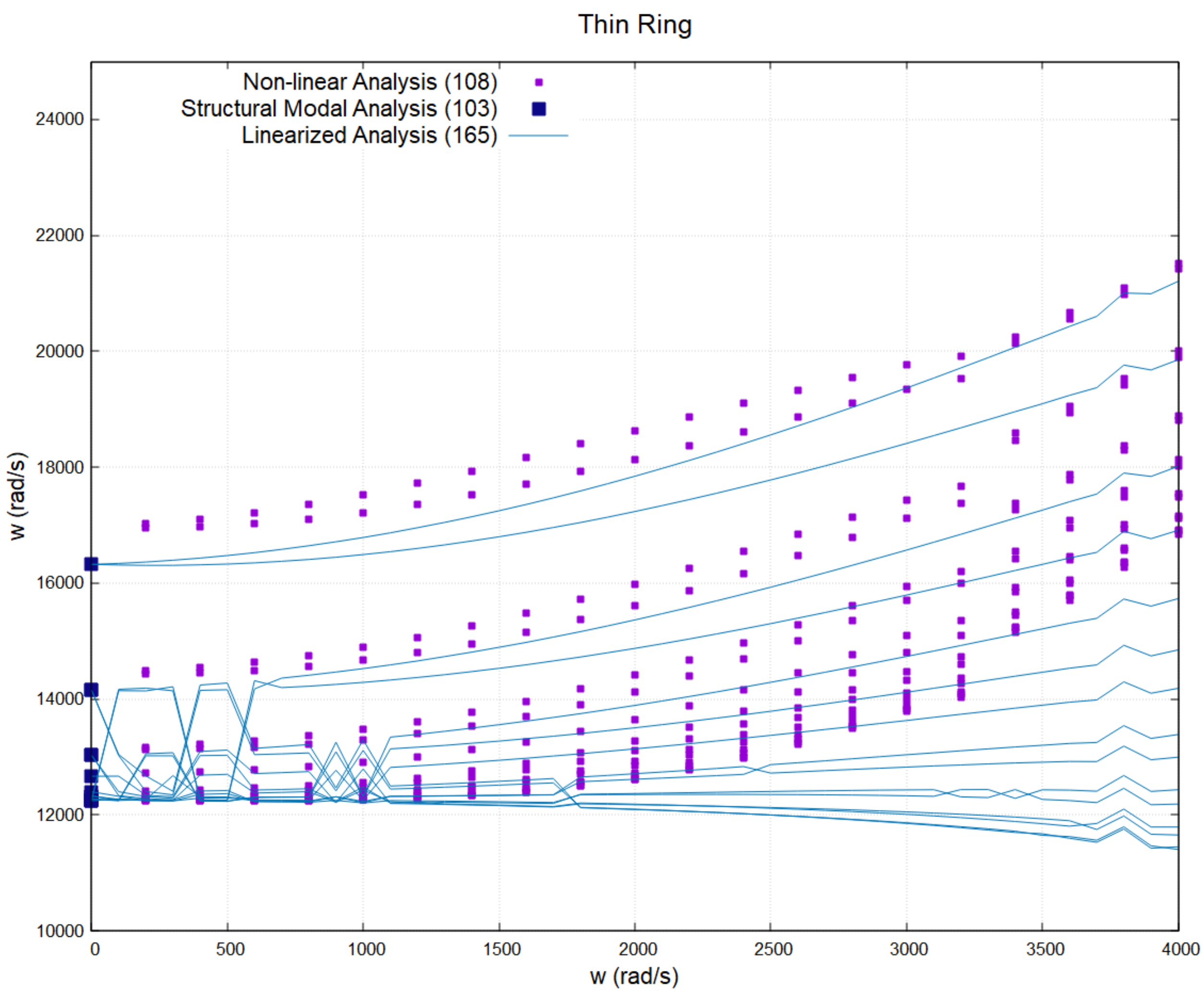

Figure 5.14 : Campbell Diagram for the Thin Ring

Bladed Disk

Our analysis continues with the study of the Bladed Disk already described in chapter 4.

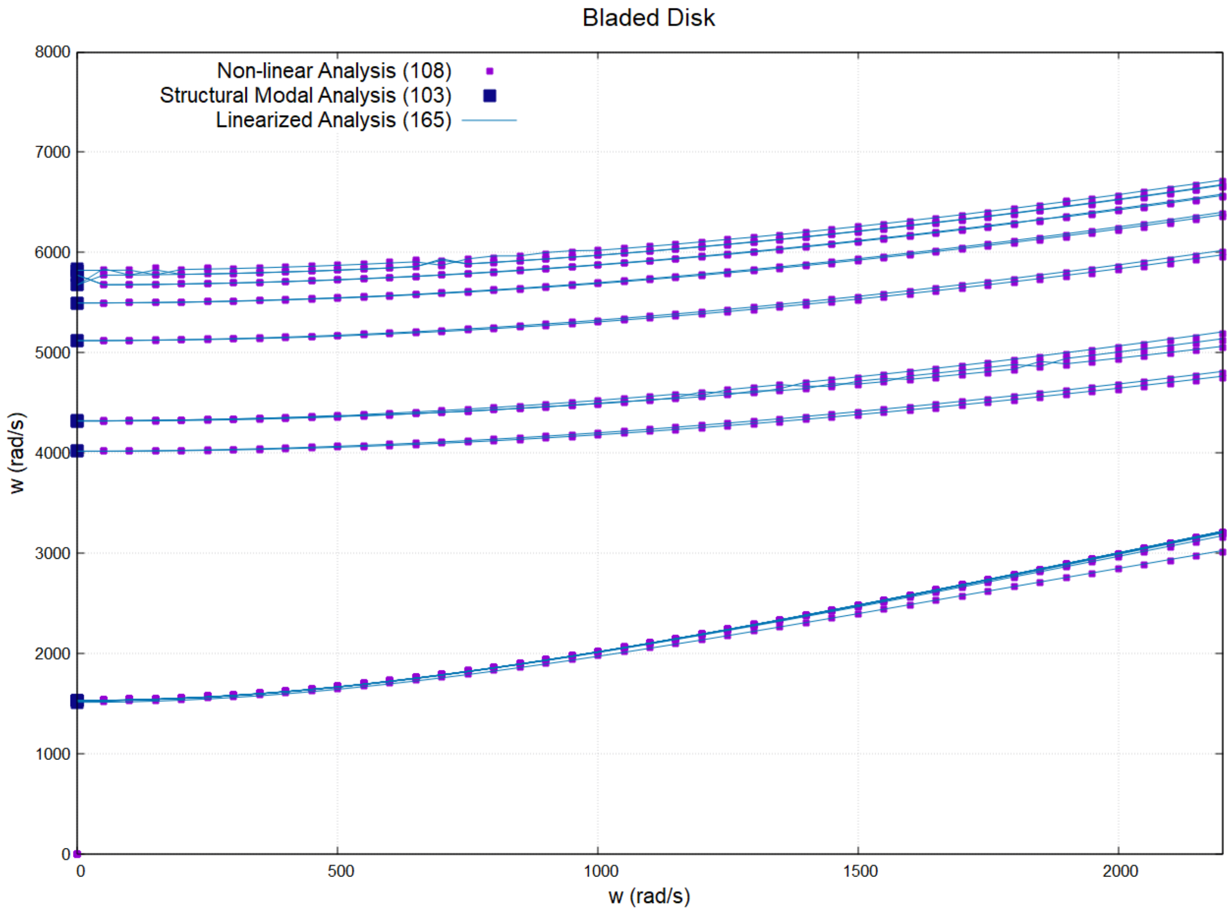

Figure 5.15 : Campbell Diagram for the Bladed Disk

Since the bladed disk, as it was modeled, is a fairly thick and rigid structure, it is noted how the two analyses perform well and present almost the same results: both the non-linear (108) and the linearized (165) analyses were able to "capture" in the proper way the growth of natural frequencies, and therefore the stress stiffening, caused by the increasing centrifugal force with the increasing rotation speed. The 2 kinds of analysis mirror each other (**Fig. 5.15**): here we can see the growth of the natural frequencies with the rotational speed of the dynamic system.

As already noted in the comments of **Tab. 4.6**, even in the rotordynamic analysis the structural dynamics of this disk is dominated by the bending modes of the 16 blades, which in fact have their first 16 natural frequencies all packed around the value of $243\ Hz \approx 1526\ rad/s$.

These natural frequencies families correspond to the lowest continuous blue line within the Campbell diagram, and it will be especially here that the main differences will be noticed, once 3 main Mistuning Patterns are analyzed.

Mistuned Bladed Disk

In mechanical engineering, mistuning is defined as a lack of symmetry present in a real object that ideally is perfectly symmetric. This phenomenon is mainly studied in relation to turbine disks and engine rotors as, for example, it can cause a sudden increase of the forced response that can bring about unexpected failures due to fatigue. Mistuning is caused by manufacturer tolerances, non-homogeneity of the material, wear dictated by usage and many other factors, being for this reason unavoidable.

Many studies have been carried out in this field, and it has been observed that the magnitude of the increase in the forced response of mistuned turbine discs strongly depends on the physical characteristics of the disc itself. Currently, the main efforts to limit the negative effects of this phenomenon on turbine discs focus on understanding how to design a disc that is affected as little as possible by mistuning in the design work rotation speed.

To do this, a large number of different mistuning patterns are statistically tested, gradually simulating different combinations of blades that could have degraded mechanical characteristics due to grain defects of the material, incorrect geometric tolerances during production or even non-homogeneous wear compared to the neighboring blades. These analyzes are crucial for the good design of the components and for their reliability, but they are also very time-consuming, since with Mistuning it is difficult, if not impossible, to use cyclic symmetry to save on the number of degrees of freedom of the finite element model (**Fig. 5.16**).

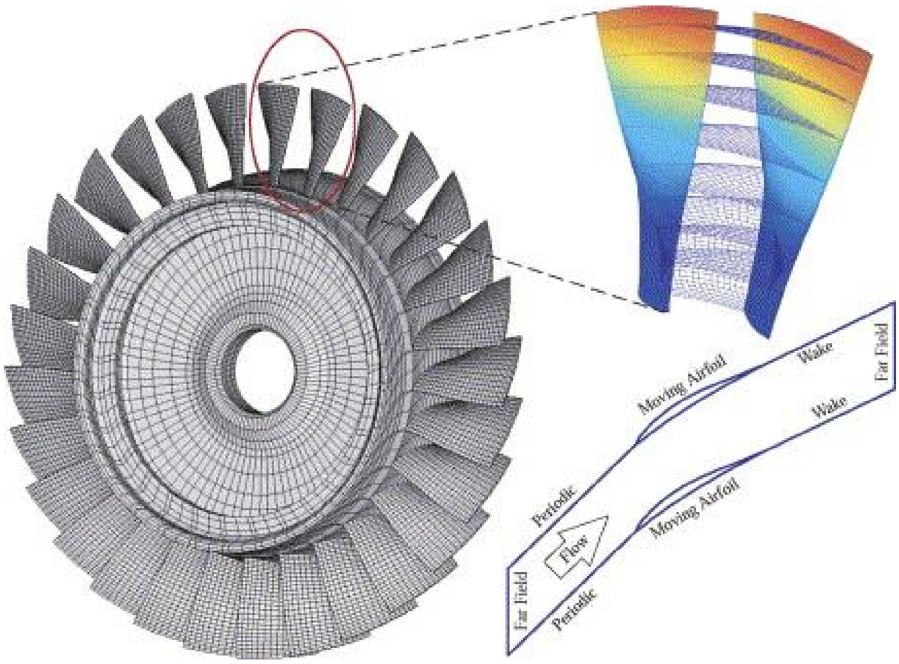

Figure 5.16 : 3D solid FEM model for the analysis of Mistuning [16]

In our case, the input folder of the Mul2 code turns out to be extremely convenient, as it is sufficient to act on the *EXP_CONN.dat* file, modifying the lamination index, and therefore the material, of the specific Lagrange element of the blade to which we want to apply a mistuning pattern.

For the purpose of this thesis, 3 simple Mistuning patterns will now be analyzed, presented in the **Fig. 5.17**: they provide that 1, 2 or 4 blades positioned in strategic locations have suffered a degradation of the mechanical characteristics of the material of 10% compared to the nominal value.

This means that, if the disc considered TUNED is formed by a steel alloy with the following mechanical characteristics,

$$E = 174\ GPa, \qquad \nu = 0.3, \qquad \rho = 8200\,\frac{kg}{m^3}$$

the blades that have been modelled with defects are instead entirely made of a fictitious material that has these data, corresponding to 90% of those listed above:

$$E = 156\ GPa, \qquad \nu = 0.27, \qquad \rho = 7400\,\frac{kg}{m^3}$$

The colored blade in the image below clearly indicates the one made of degraded material:

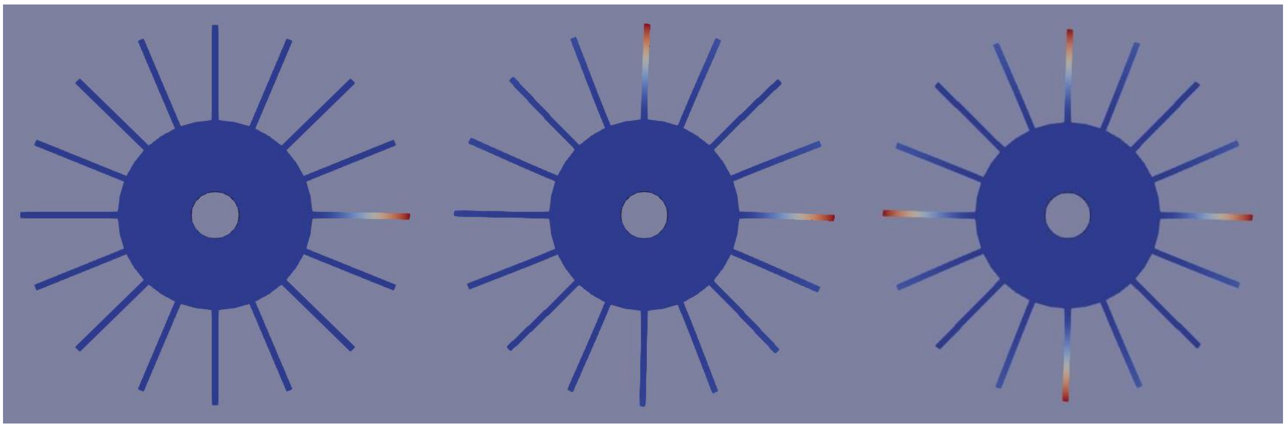

Figure 5.17 : Mistuned Patterns analyzed for the Bladed Disk

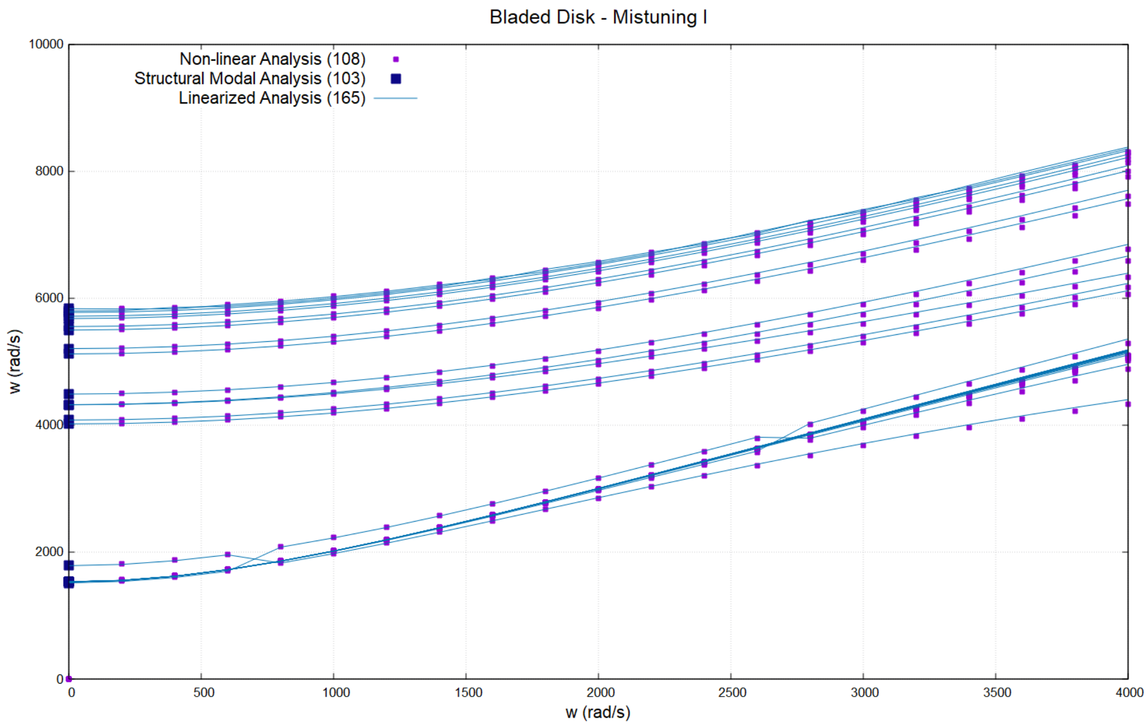

Figure 5.18 : Mistuned Bladed Disk – I blade Pattern - Campbell Diagram

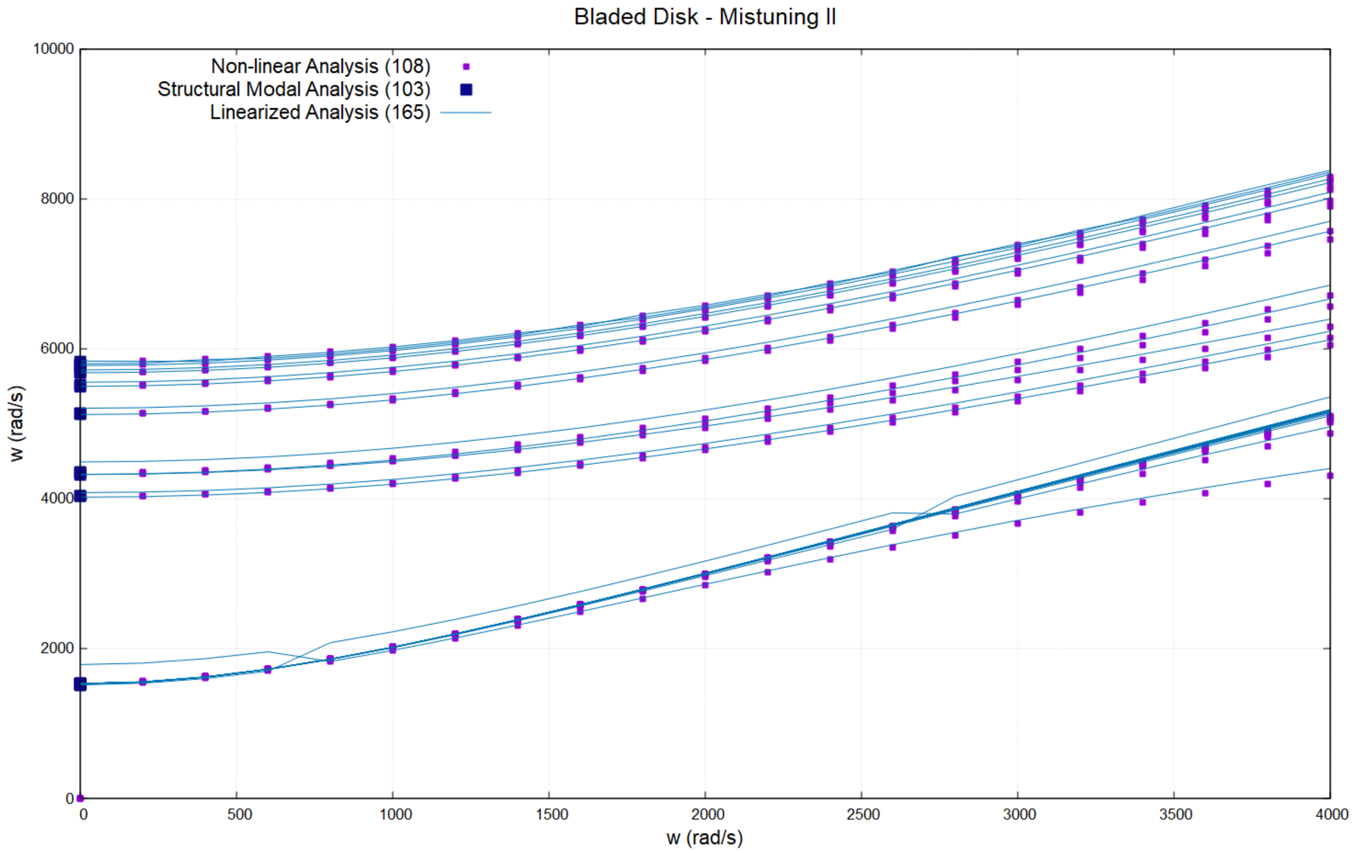

Figure 5.19 : Mistuned Bladed Disk – II blades Pattern - Campbell Diagram

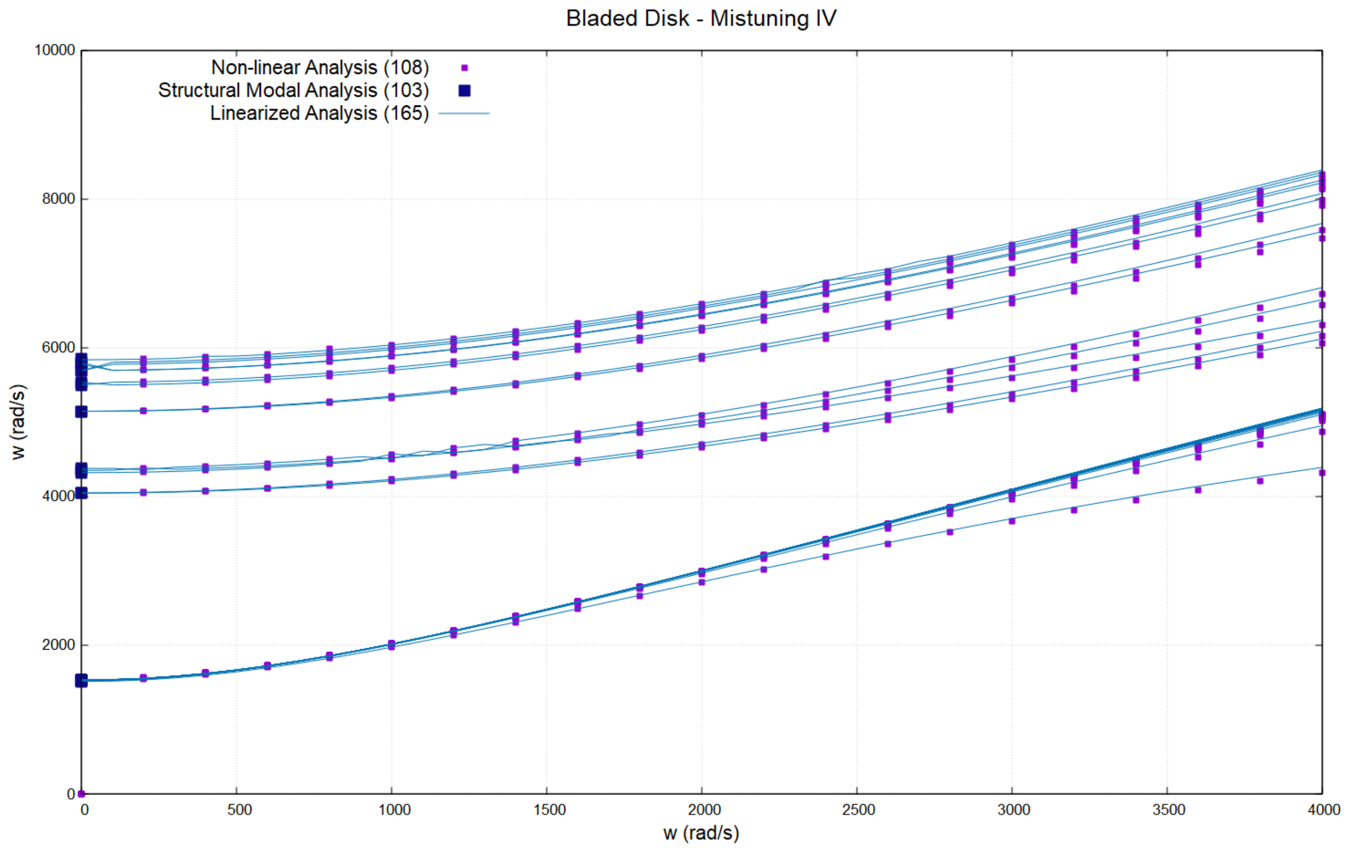

Figure 5.20 : Mistuned Bladed Disk – IV blades Pattern - Campbell Diagram

As expected, all 3 Campbell diagrams for the 3 mistuning cases analyzed (**Fig. 5.18 – 5.19 - 5.20**)show good harmony between the results of the linearized and nonlinear analysis.

As announced, the differences, albeit small, between the 3 cases can be seen above all in the lower part of the graphs, where, for example in the case of Mistuning on 4 blades placed at 90° from each other, there is a further condensation of natural frequencies families.

In the same graph, we can also locate some intersections between families as calculated by the linearized analysis, but overall it can be said that the Mul2 code has worked successfully in this situation as well.

Chapter VI
Conclusions

The innovative approach used in this thesis work was mainly given by the application of the Mul2 code to the rotordynamic study of axial rotors in the geometrically non-linear field.

After having learned the structure of the software and the management of all its inputs, we first committed ourselves to validating the code in a static configuration, at zero speed, comparing the results obtained from the simulation with those taken from articles and papers in the bibliography.

After having obtained sufficient confidence regarding the reliability of the results, the analysis was extended to the dynamic case, implementing rotation by imposing the centrifugal force as an external forcing.

It was therefore possible to study the behavior of various structures, with different geometric characteristics, depending on the models used for the analysis and the material. Additional models were generated to investigate thin and flexible structures, where the difference between 108 and 165 analyzes was more evident, given the greater distance between deformed and undeformed configuration of the structure with low stiffness. A lot of time was spent analyzing the right boundary conditions to apply, in order to understand the crucial inputs for the fit between the results of the nonlinear and linearized analysis.

The most interesting results, based on the considered structure, can be summarized as follows:

- A perfect overlap was observed between the two types of analysis for the cases of discs with constant and variable thickness, even at very high speeds.
- Some weaknesses of the linearized analysis have been identified in describing the high-speed dynamics of particularly thin and deformable structures, such as the case of the thin ring and the shallow and deep shells.
- A good but not perfect harmony was found between the results in the case of the cylinders and the complex rotor, even if the rich phenomenology that distinguishes the dynamics of these particular structures emerged.
- A dynamic study was conducted on a bladed disk model implemented during the thesis, to which 3 simple mistuning patterns were also applied: the effectiveness of the Mul2 code and the CUF in obtaining reliable results in a short time and with significantly reduced computational load compared to commercial FEM codes was thus proven. This aspect could be fundamental for the study of mistuning and further developments in this sense can certainly be carried out in the future.

Bibliography

[1] L. Caracciolo e L.Canali "L'ora più chiara", in "*Il Mondo Virato*", Limes - Rivista Italiana di Geopolitica n° 3/2020. Gedi Gruppo Editoriale SpA, Roma

[2] P. Gloeckner, C. Rodway. "The Evolution of Reliability and Efficiency of Aerospace Bearing Systems", in *Engineering* 09.2017. pp 962-991. DOI: 10.4236/eng.2017.911058

[3] J.S. Rao. "*History of Rotating Machinery Dynamics".* Springer Netherlands, 2011

[4] J. Vance, F. Zeidan, B. Murphy. "*Machinery vibration and rotordynamics".* John Wiley and Sons, INC. 2010

[5] Y. Ishida, T. Yamamoto. "*Linear and Nonlinear Rotordynamics".* A modern Treatment with Applications, 2nd enlarged and Improved Edition. Wiley-VCH Verlag & Co. 2012

[6] A. Stodola. "Dampf und Gas-Turbinen", Verlag von Julius Springer, Berlin. 1924
English translation "Steam and Gas Turbines", McGraw-Hill, New York. 1927

[7] A.D. Dimarogonas. "A Brief History of Rotor Dynamics", Conference paper for *Rotordynamics* '92, pp 1-10, Springer London. 1992

[8] K.P. Van Hooser, D.P. Bradley, "Space Shuttle Main Engine - The Relentless Pursuit of Improvement", Conference Paper for the AIAA SPACE Meeting, Long Beach, California, 2011. Document ID: 20120001539.

[9] E. Carrera, M. Cinefra, M. Petrolo, E. Zappino, "*Finite Element Analysis of Structures through Unified Formulation*". John Wiley & Sons Ltd. 2014

[10] E. Carrera, M. Filippi, "A refined one-dimensional rotordynamics model with three-dimensional capabilities", in *Journal of Sound and Vibrations*, vol. 366. 2016, pp 343-356 ISSN 0022-460X

[11] A. Pagani, E. Carrera, "Unified formulation of geometrically nonlinear refined beam theories", in *Mechanics of Advanced Materials and Structures*, 2018. 25:1, pp 15-31, DOI: 10.1080/15376494.2016.1232458

[12] M. Filippi, A. Pagani, E. Carrera (July 24, 2018), "Accurate Nonlinear Dynamics and Mode Aberration of Rotating Blades." ASME. *J. Appl. Mech*. Novmeber 2018; 85(11): 111004 https://doi.org/10.1115/1.4040693

[13] A. Entezari, M. Filippi, E. Carrera "On dynamic analysis of variable thickness disks and complex rotors subjected to thermal and mechanical prestresses" in *Journal of Sound and Vibration*, Volume 405, 2017. pp 68-85. ISSN 0022-460X https://doi.org/10.1016/j.jsv.2017.05.039.

[14] A. Entezari, M. Kouchakzadeh, E. Carrera, M. Filippi (2017). "A refined finite element method for stress analysis of rotors and rotating disks with variable thickness". *Acta Mechanica*. 228. 10.1007/s00707-016-1727-x.

[15] Alexander Kosenkov , https://commons.wikimedia.org/w/index.php?curid=17153099

[16] Z. He, B.I. Epureanu, C. Pierre, (2007) "Parametric study of the aeroelastic response of mistuned bladed disks", in *Computers & Structures*, Volume 85, Issues 11-14. pp 852-865. ISSN 0045-7949 https://doi.org/10.1016/j.compstruc.2007.01.007.